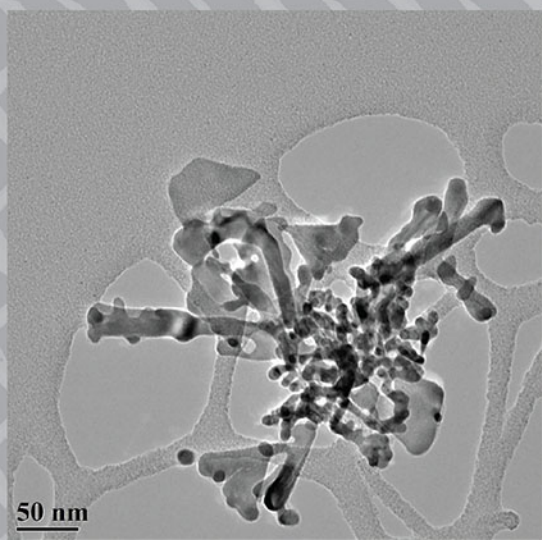# Functional Materials and Applied Physics

FMAP-2021

50 nm

Edited by

**Yogesh Sonvane, Dimple Shah,
K.N. Pathak and Lalit Saini**

M|R|F

Functional Materials and Applied Physics
FMAP-2021

Virtual International Conference on
Functional Materials and Applied Physics (FMAP-2021), held
14-15 May 2021 at S.V. National Institute of Technology, Surat
Ichchhanath, Surat-395 007, Gujarat, India

Editors
Yogesh Sonvane, Dimple Shah, K.N. Pathak and Lalit Saini

Department of Physics, S.V. National Institute of Technology, Surat
Ichchhanath, Surat-395 007, Gujarat, India

Peer review statement

All papers published in this volume of "Materials Research Proceedings" have been peer reviewed. The process of peer review was initiated and overseen by the above proceedings editors. All reviews were conducted by expert referees in accordance to Materials Research Forum LLC high standards.

This book contains information obtained from authentic and highly regarded sources. Reasonable efforts have been made to publish reliable data and information, but the author and publisher cannot assume responsibility for the validity of all materials or the consequences of their use. The authors and publishers have attempted to trace the copyright holders of all material reproduced in this publication and apologize to copyright holders if permission to publish in this form has not been obtained. If any copyright material has not been acknowledged please write and let us know so we may rectify in any future reprint.

Table of Contents

Preface

It is a matter of immense pleasure and proud privilege to bring out this proceeding of the "International Conference on Functional Materials and Applied Physics (FMAP-2021)" held via Online Mode at SVNIT 14-15 May 2021.

The International Conference is a premier forum for the presentation of new advances and research results in Functional Materials and Applied Physics. It brings together leading academic scientists, experts from industry, and researchers in their domains of expertise worldwide. The conference featured highly selective research papers, keynotes, plenary, and invited talks.

We are pleased to state the conference had glaring success with more than 80 research papers presented. The conference also witnessed several papers of interdisciplinary nature, genuinely reflecting the integration of computational physical science. Our review panel members also put in their hearts and helped us in including high-quality research papers, and for this, we are highly indebted to all our reviewers.

We also would like to express our special thanks to Thomas Wohlbier from Materials Research Forum LLC for his support of FMAP-2021.

With best wishes,
Dr. Dimple Shah, Conference Chairman, FMAP-2021
Prof. K. N. Pathak, Conference Chairman, FMAP-2021
Dr. Yogesh Sonvane, Organizing Secretary, FMAP-2021
Dr. L. K. Saini, Organizing Secretary, FMAP-2021

Virtual International Conference on
Functional Materials and Applied Physics (FMAP-2021)
Under Institute Diamond Jubilee Celebration
14-15 May 2021

Organized by
Department of Physics
S. V. National Institute of Technology, Surat
Ichchhanath, Surat-395 007, Gujarat, India

EDITORS

ORGANIZING COMMITEE

CHIEF PATRON
Chairman, BOG, SVNIT, Surat

PATRON
Prof. S. R. Gandhi, Director, SVNIT

Co-Patron:
Prof. P. L. Patel, Deputy Director, SVNIT

Chairman
Prof. Dimple Shah, Head, DOP, SVNIT

Organizing Secretaries
Prof. K. N. Pathak, Professor, DOP, SVNIT
Dr Yogesh Sonvane, Assistant Professor, DOP, SVNIT
Dr L. K. Saini, Assistant Professor, DOP, SVNIT

INTERNATIONAL ADVISORY COMMITTEE
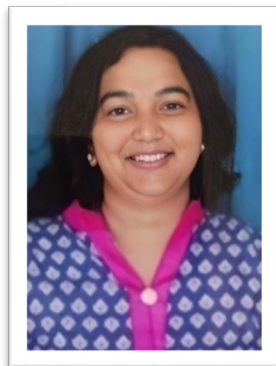
Prof. Ravindra Pandey,USA
Prof. Rajeev Ahuja, Sweden
Prof. Nicola Seriani, Italy
Prof. Rita Magri, Itlay
Prof. Prof. C. Jagdish, Australia
Dr. Yogendra Kumar Mishra, Denmark
Dr. Mohammad Mahdi Tavakoli, USA
Dr. S D. Mohanti, USA
Dr. Sohail Ahmad, Saudi Arabia
Prof. Aditya Mohite, LANL
Prof. Abdul Rahman, KAUST
Prof. Zakheerudin Mohammed, EPFL
Prof. Sushil Auluck, NPL, New Delhi
Prof. Rajeev Ahuja, Upsala, Sweden
Prof. Igor Lukacevic, Croatia
Prof. S.D. Mahanti, MSU, USA
Prof. Kirill Nekrassov,
Ural Federal University, Russia
Prof. Zafar Said, University of Sharjah, UAE
Prof. Madhav Ghimire, Tribhuvan University, Nepal
Prof. Satishchandra Ogale, IISER, Pune
Prof. D. G. KUBERKAR, Saurashtra University, Rajkot
Prof. Sumit Saxena, IIT Bombay
Prof. Kanishka Biswas, JNCASR, Bangalore
Dr. Pankaj R Sagdeo, IIT Indore
Dr. Sivaiah Bathula, IIT BHUBANESWAR
Dr. Abir De Sarkar, INST, Mohanli
Dr Amrita Bhattacharya, IIT, Bombay

Prof. A. R. Jani, SICART, Anand
Prof. ManojHarbola, IIT, Kanpur
Prof. K. G. Suresh, IITB, Mumbai
Prof. P. K. Jha, MSU, Vadodara
Dr. C. Majumdar, BARC, Mumbai
Prof. Pankaj Gajjar, GU, Ahmedabad
Prof. Pankaj Thakor, VNSGU, Surat
Dr. Satyaprakash Sahoo, IOPB, BBSR
Dr. B. P Mandal, BARC, Mumbai
Dr. Dhiraj Singh, IITRAM, Ahmedabad
Prof.VivekPolshettiwar, TIFR, Mumbai
Prof.Asim Roy, NIT Silchar
Prof. Raju K.George, IIST , Kerala
Dr. Jain, Madhu, IIT Roorkee
Prof. Muslim Malik, IIT, Mandi
Prof. ManojHarbola, IIT, Kanpur
Prof.Natesan Srinivasan, IIT Guwahati
Prof.Kasi Viswanadhan KNS, NIT Warangal
Dr. Niraj Kumar Shukla, IIT Indore
Prof. A. K. Tyagi, BARC, Mumbai
Prof. S. K. Ray, SNBNCBS, Kolkotta
Prof. D. K. Aswal, CSIR-NPL, New Delhi
Dr. S. K. Varshney, DST, New Delhi
Dr. Pankaj Poddar, NCL, Pune
Dr. B. P Mandal, BARC, Mumbai
Dr. Prakash Jha, CUG, Gandhinagar
Prof. Amitava Das, CSMCRI,Bhavnagar
Dr Ashok Kumar, CUP, Bathinda
Dr. Sanjeev Gupta. SXC, Ahemdabad.

Coulomb Drag Study of Non-Homogeneous Dielectric Medium: Hole-Hole Static Interactions in 2D-GaAs DQW

Sharad Kumar Upadhyay[a] [*] and L.K. Saini[b]

Department of Physics, Sardar Vallabhbhai National Institute of Technology, Surat, (395007), Gujarat, India

[a]sharadupadhyay1992@gmail.com, [b]drlalitsaini75@gmail.com

Abstract. The induced (drag) resistivity (ρ_D) is calculated numerically in low temperature, large interlayer separation and weak interactive regime for 2D hole-hole (h-h) static interactions using the RPA method, with the geometry of non-homogeneous dielectric medium. Exchange-correlations (XC) and mutual interaction effects are considered in low/high density regime for analysing the drag resistivity. It is found that the drag resistivity is found inhanced on using the XC effects and increases on increasing the effective mass. In Fermi-Liquid regime, drag resistivity is directly proportional to r^2/n^3 at low temperature. Temperature (T), density (n), interlayer separation (d) and dielectric constant (ϵ_2) dependency of drag resistivity is measured and compared to 2D e-e and e-h coupled-layer systems with and without the effect of non-homogeneous dielectric medium.

Introduction

Coulomb drag (CD) is a transport phenomenon that occurs in coupled layer structure, when a current is allow to flow by an active layer and a drag/induced voltage is detected in passive layer, without the tunnelling effect [1–13]. An insulated wall seperates both the layers electrically. Drag resistivity (ρ_D) is a general phenomena of momentum and energy transfer rate by the interaction of electron-electron (e-e), electron-hole (e-h), hole-hole (h-h), pasmons and phonons etc. With the Fermi-liquid state, the phase space give the dependency of drag resistivity, as $\rho_D \propto T^2/n^3$ at low temperature regime.

Consequently, coulomb drag effect was devoted to the numerically and quantitatively results, for measuring the strength of the screening due to induced field [14,15], electron-electron bilayer system of 2D-3D [7,16], two dimensional (2D) electron-electron (e-e) [16–20]. A vast range of curiosity have emerged for studying transport based properties. Mutual coulomb scattering can theoretically be realised cause of the exchange of momentum ($\hbar q$) and energy ($\hbar \omega$) between the coupled layers system. Following the ground breaking experimental work in the AlGaAs/GaAs double quantum wells (DQW) [17,20]. Drag effect became an important part for measuring the many body properties. It had been used to analyze the properties of electrons, holes, phonons, plasmons. Interactions in low density regime [21,22], excitons impact of e-h double layers systems [23–25].

Theoretically, a vast and explored field of CD phenomena which suggested several extensions and generalizations in the field of non-homogeneous dielectric medium. The theory of CD effect has extended to multi-layer between two 2D electron and/or hole system, which is an fascinating electronic system of 2D-GaAs DQW [2,3,6,8,11–13,26–30]. For the simplest such structure, CD in bilayer systems is a very interesting phenomenon. We consider two 2D-GaAs distanced by a insulated wall of Al_2O_3, with the case of a large interlayer separation limit ($k_F d \gg 1$), where d is

a distance of the wall and k_F is the Fermi wave vector of 2D-sheets. It is a general and well known results for ρ_D, which present the dependency to temperature and interlayer separation, as $T^2 d^{-4}$ in low temperature, large separation and weak interaction limit.

Theoretical Formalism
With considering a double layer systems of 2D-GaAs, which contain holes in both the layers. The numerical results of drag resistivity is measured by using the solution of RPA method in weak interaction ($r_s \sim 1$), at low temperature ($T_F \gg T$), and large interlayer distance limit ($k_F d \gg 1$). The interlayer screening ($U_{12}(q)$) caused of hole-hole (h-h) static interaction is considered in this manuscript. In low concentration regime ($r_s \gg 1$), the RPA method don't able to hold consistency cause of exchange correlations (XC) effects are not considered. The total screening between the electron and/or hole extracted enhanced results because of XC effects. The LFC introduced by the HA and STLS approximation, which consider the XC effect into account.

A general expression of drag resistivity [2,3,6,8,11–13,26–30] may be present as,

$$\rho_D = -\frac{\hbar^2}{8\pi^2 e^2 n_1 n_2 k_B T} \int_0^\infty dq\, q^3 |U_{12}(q)|^2 \int_0^\infty d\omega\, \frac{|\Im\chi_1(q,\omega)||\Im\chi_2(q,\omega)|}{\sinh^2\left(\frac{\hbar\omega}{2k_B T}\right)} \tag{1}$$

To evaluate the drag resistivity, nonlinear susceptibility function (NLSF) and effective interlayer interaction are main function. This gives the dependency of temperature T, density n, interlayer distance d, etc.…

Nonlinear Susceptibility Function (NLSF)
The non-interacting NLSF [$\chi(q,\omega)$] in weakly interactive and low frequency regime (Ballistic regime) ($\omega\tau \gg 1$ or $k_F\ell \gg 1$), as seen in Eq. (2), which extracted temperature dependency of ρ_D in Fermi-liquid regime. Analytically, it is entirely determined by the denominator $\sinh^2(\frac{\hbar\omega}{2k_B T})$ in Eq. (1), which restricts the integral with respect to frequency, $\hbar\omega < 2k_B T$. The non-interacting NLSF $\chi_{1(2)}(q,\omega)$ [1,3,8,11,12,31] which is presented by the equation as,

$$\chi(q,\omega) = -\int \frac{d\mathbf{k_i}}{4\pi^2} \frac{(f^0(\xi_i)-f^0(\xi_i \pm \hbar\omega))}{\xi_i - \xi_{i'} \pm \hbar\omega - i\delta} \tag{2a}$$

$$\Im\chi(q,\omega) = -\int \frac{d\mathbf{k_i}}{4\pi^2} \big(f^0(\xi_i) - f^0(\xi_i + \hbar\omega)\big)\delta(\xi_i + \xi_{i'} - \hbar\omega) \tag{2b}$$

Interlayer Interaction [$U_{12}(q)$]
To evaluating the screening effects of holes in the double layer systems, a typical toolbox of Dyson equation is taken into consideration within the random phase approximation (RPA) method [2,3,6,8,11–13,26–30]. This finally presents the standard equation of interlayer interaction as,

$$U_{12}(q) = \frac{U_{12}^0(q)}{\varepsilon(q)} \tag{3a}$$

$$\varepsilon(q) = \big(1 + U_{11}^0(q)\{1 - G_{11}(q)\}\chi_1(q)\big)\big(1 + U_{22}^0(q)\{1 - G_{22}(q)\}\chi_2(q)\big) - (q))^2\chi_1(q)\chi_2(q) \tag{3b}$$

The screening effects is measured by the Eq. (3a) for interactive weak field cause of stationary point charge source is present at active layer and drag the carriers in other layer. Where $\varepsilon(q)$ is the dielectric function. $U_{ii}^0(q)$ and $U_{ij}^0(q)$ are known as bare intra and interlayer potential, respectively and local form factor (LFF) $F_{ij}(qd)$ are key equations. To evaluating the form factor $F_{ij}(qd)$,

electrostatic problem needs to solve by using the solution of Poisson equation, by assuming the different-different screening of substrate layer, insulated layer, and top layer (such as, air) [3,8,11–13,32]. The form factors for non finite width [3,8,11–13,32],

$$F_{11}(d) = \frac{\epsilon_2 \exp(qd)[\epsilon_2 \cosh(qd) + \epsilon_1 \sinh(qd)]}{[(\epsilon_1+\epsilon_2)(\epsilon_3+\epsilon_2)\exp(2qd)-(\epsilon_1-\epsilon_2)(\epsilon_3-\epsilon_2)]} \tag{4a}$$

$$F_{12}(d) = \frac{\epsilon_2 \exp(qd)}{[(\epsilon_1+\epsilon_2)(\epsilon_3+\epsilon_2)\exp(2qd)-(\epsilon_1-\epsilon_2)(\epsilon_3-\epsilon_2)]} \tag{4b}$$

Where $F_{22}(d)$ may be obtained by replacing $\epsilon_1 \leftrightarrow \epsilon_3$ in Eq. (4a).

The method of RPA with including the XC effects is a implications of measuring the required results. The LFC of using the HA and STLS approximation are commonly used approximations for considering the XC effects. ρ_D is enhanced on using the LFC, as seen in Eq. (3). The LFC is evaluated by the solution of the static structure factor S(q) by using the fluctuation dissipation theorem [3–5,13,33,34].

$$G(q) = -\frac{1}{n}\int_0^\infty \frac{d\boldsymbol{k}}{(2\pi)^2}\frac{\boldsymbol{q}.\boldsymbol{k}}{q^2}\frac{U^0(\boldsymbol{k})}{U^0(\boldsymbol{q})}S(|\boldsymbol{k}-\boldsymbol{q}|-\delta) \tag{5}$$

Result and Discussion

In this section, we have discussed about the structure and results of ρ_D in screened double layer systems od 2D-GaAs at low temperature and Boltzmann regime. Present approach for the sulution of ρ_D expression, which is a solution of the Boltzmann kinetic equation (BTE). The system is taken under the low temperature limit $T \ll T_F$, the large interlayer distance $k_F d \gg 1$ [2,3,6,8,11–13,26–30]. With the weak interactions limit and low frequency regime, ρ_D behaves as $\frac{T^2\epsilon_2^2}{n^3 d^4}$ in the limit of $T \ll T_F$, as shown in Fig. (1a, 1b). This is the same variables dependency found for the drag resistivity [2,3,6,8,11–13,26–30].
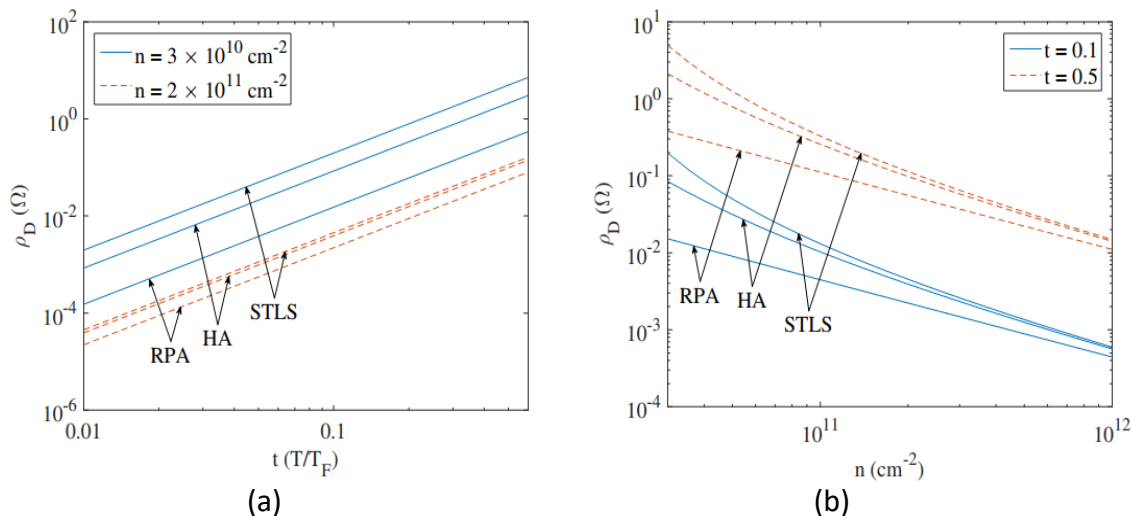

Figure 1: The plots show the behavior of the absolute value of ρ_D with respect to temperature (T) and concentration (n), as shown in Fig. (1a, 1b), respectively. Where the dielectric constant of the barrier is Al_2O_3 $(\epsilon_2 = 9)$ and inter-layer distance is d = 30 nm.

The measured data of ρ_D for h-h interactions is compared by measured results of e-e and e-h interactions [1,13]. ρ_D is found 14.47, 16.18 $m\Omega$ for e-e and e-h interactions [11,13] for the parameters such as, the carrier concentration $n \sim 3 - 20 \times 10^{10}\ cm^{-2}$, temperature is t = 0.5 k, the interlayer separation is d = 30 nm, the dielectric constant of the barrier is $\epsilon_2 = 9$, interlayer distance d = 30 nm, effective mass of hole is $0.45 m_e$. For these parameter, h-h interactions found enhanced results compare to e-e and e-h interactions, as seen in Fig. (1a, 1b) for the RPA method with and without including the LFC effects.

Articles on ρ_D in coupled-layer structure measured inhanced results of stationary and weak screening with including the LFC, as seen in Fig. (1a, 1b). It is found consistently better results for h-h interactions than RPA method, because of LFC based on HA and STLS approximation. The RPA model does not account for XC impacts, which are taken into account by LFC. The expressions of LFC impact the effect of interlayer interaction effective and cause of this, ρ_D is found enhanced [3,11–13]. This is because the coupling between the charge carriers has increased as a result of the increase in coupling, as seen in Fig. (1a, 1b).

Conclusion

In this section, its aim is to demonstrate the improvement of ρ_D as a result of h-h screening, as well as the impact of LFC, compare to e-e and e-h screening of weakly coupling condition. ρ_D is measured for density r_s = 1.154–2.979, at low temperature and large interlayer distance in a double layer structure, separated by a thick wall. The measured results of ρ_D are consistently better compare to the system of a simple double layer systems.

References

[1] A. P. Jauho and H. Smith, *Coulomb Drag between Parallel Two-Dimensional Electron Systems*, Phys. Rev. B **47**, 4420 (1993). https://doi.org/10.1103/PhysRevB.47.4420

[2] A. Kamenev and Y. Oreg, *Coulomb Drag in Normal Metals and Superconductors: Diagrammatic Approach*, Phys. Rev. B **52**, 7516 (1995). https://doi.org/10.1103/PhysRevB.52.7516

[3] S. K. Upadhyay and L. K. Saini, *Study of Drag Resistivity in Dielectric Medium with the Correlations Effect*, Appl. Phys. A **127**, 276 (2021). https://doi.org/10.1007/s00339-021-04422-y

[4] S. K. Upadhyay and L. K. Saini, *Coulomb Drag Study in Graphene/GaAs Bilayer System with the Effect of Local Field Correction and Dielectric Medium*, Phys. E Low-Dimensional Syst. Nanostructures **127**, 114484 (2021). https://doi.org/10.1016/j.physe.2020.114484

[5] S. K. Upadhyay and L. K. Saini, *Drag Resistivity in Bilayer-Graphene/GaAs Coupled Layer System with the Effect of Local Field Corrections*, Eur. Phys. J. Plus **136**, 433 (2021). https://doi.org/10.1140/epjp/s13360-021-01377-0

[6] R. Pillarisetty, H. Noh, D. C. Tsui, E. P. De Poortere, E. Tutuc, and M. Shayegan, *Frictional Drag between Two Dilute Two-Dimensional Hole Layers*, Phys. Rev. Lett. **89**, 16805 (2002). https://doi.org/10.1103/PhysRevLett.89.016805

[7] P. M. Solomon, P. J. Price, D. J. Frank, and D. C. La Tulipe, *New Phenomena in Coupled Transport between 2D and 3D Electron-Gas Layers*, Phys. Rev. Lett. **63**, 2508 (1989). https://doi.org/10.1103/PhysRevLett.63.2508

[8]   B. Scharf and A. Matos-Abiague, *Coulomb Drag between Massless and Massive Fermions*, Phys. Rev. B **86**, 115425 (2012). https://doi.org/10.1103/PhysRevB.86.115425

[9]   S. K. Upadhyay and L. K. Saini, *Drag Resistivity in InAs/GaAs and InAs/GaSb Bilayer Due to Electron-Electron Interactions*, AIP Conf. Proc. **2220**, 140031 (2020). https://doi.org/10.1063/5.0002594

[10] L. K. Saini, S. K. Upadhyay, and B. P. Bahuguna, *Investigations of Optical and Thermoelectric Response of GaBi Monolayer*, AIP Conf. Proc. **2220**, 20158 (2020). https://doi.org/10.1063/5.0002593

[11] S. K. Upadhyay and L. K. Saini, *Coulomb Drag of Electron-Electron Interactions in GaAs Bilayer with a Non Homogeneous Dielectric Background*, Adv. Mater. Lett. **11**, 20071539 (2020). https://doi.org/10.5185/amlett.2020.071539

[12] S. K. Upadhyay and L. K. Saini, *Coulomb Drag Study in Electron-Electron Bilayer System with a Dielectric Medium*, Phys. E Low-Dimensional Syst. Nanostructures **124**, 114350 (2020). https://doi.org/10.1016/j.physe.2020.114350

[13] S. K. Upadhyay and L. K. Saini, *Study of Coulomb Drag with the Effect of Local Field Correction and Dielectric Medium*, Phys. B Condens. Matter **614**, 412982 (2021). https://doi.org/10.1016/j.physb.2021.412982

[14] R. A. Höpfel, J. Shah, P. A. Wolff, and A. C. Gossard, *Negative Absolute Mobility of Minority Electrons in GaAs Quantum Wells*, Phys. Rev. Lett. **56**, 2736 (1986). https://doi.org/10.1103/PhysRevLett.56.2736

[15] R. A. Höpfel and J. Shah, *Electron-Hole Drag in Semiconductors*, Solid. State. Electron. **31**, 643 (1988). https://doi.org/10.1016/B978-0-08-036237-3.50080-2

[16] P. M. Solomon and B. Laikhtman, *Mutual Drag of 2D and 3D Electron Gases in Heterostructures*, Superlattices Microstruct. **10**, 89 (1991). https://doi.org/10.1016/0749-6036(91)90154-J

[17] T. J. Gramila, J. P. Eisenstein, A. H. MacDonald, L. N. Pfeiffer, and K. W. West, *Mutual Friction between Parallel Two-Dimensional Electron Systems*, Phys. Rev. Lett. **66**, 1216 (1991). https://doi.org/10.1103/PhysRevLett.66.1216

[18] T. J. Gramila, J. P. Eisenstein, A. H. MacDonald, L. N. Pfeiffer, and K. W. West, *Electron-Electron Scattering between Parallel Two-Dimensional Electron Gases*, Surf. Sci. **263**, 446 (1992). https://doi.org/10.1016/0039-6028(92)90386-K

[19] T. J. Gramila, J. P. Eisenstein, A. H. MacDonald, L. N. Pfeiffer, and K. W. West, *Measuring Electron—Electron Scattering Rates through Mutual Friction*, Phys. B Condens. Matter **197**, 442 (1994). https://doi.org/10.1016/0921-4526(94)90243-7

[20] J. P. Eisenstein, *New Transport Phenomena in Coupled Quantum Wells*, Superlattices Microstruct. **12**, 107 (1992). https://doi.org/10.1016/0749-6036(92)90231-S

[21] M. Kellogg, I. B. Spielman, J. P. Eisenstein, L. N. Pfeiffer, and K. W. West, *Observation of Quantized Hall Drag in a Strongly Correlated Bilayer Electron System*, Phys. Rev. Lett. **88**, 126804 (2002). https://doi.org/10.1103/PhysRevLett.88.126804

[22] M. Kellogg, J. P. Eisenstein, L. N. Pfeiffer, and K. W. West, *Evidence for 2kF Electron–Electron Scattering Processes in Coulomb Drag*, Solid State Commun. **123**, 515 (2002). https://doi.org/10.1016/S0038-1098(02)00426-X

[23] A. F. Croxall, K. Das Gupta, C. A. Nicoll, M. Thangaraj, H. E. Beere, I. Farrer, D. A. Ritchie, and M. Pepper, *Anomalous Coulomb Drag in Electron-Hole Bilayers*, Phys. Rev. Lett. **101**, 246801 (2008). https://doi.org/10.1103/PhysRevLett.101.246801

[24] C. P. Morath, J. A. Seamons, J. L. Reno, and M. P. Lilly, *Density Imbalance Effect on the Coulomb Drag Upturn in an Undoped Electron-Hole Bilayer*, Phys. Rev. B **79**, 41305 (2009). https://doi.org/10.1103/PhysRevB.79.041305

[25] J. A. Seamons, C. P. Morath, J. L. Reno, and M. P. Lilly, *Coulomb Drag in the Exciton Regime in Electron-Hole Bilayers*, Phys. Rev. Lett. **102**, 26804 (2009). https://doi.org/10.1103/PhysRevLett.102.026804

[26] M. Mo\ifmmode \checks\else š\fiko, V. Cambel, and A. Mo\ifmmode \checks\else š\fiková, *Electron-Electron Drag between Parallel Two-Dimensional Gases*, Phys. Rev. B **46**, 5012 (1992). https://doi.org/10.1103/PhysRevB.46.5012

[27] R. Pillarisetty, H. Noh, E. Tutuc, E. P. De Poortere, K. Lai, D. C. Tsui, and M. Shayegan, *Coulomb Drag near the Metal-Insulator Transition in Two Dimensions*, Phys. Rev. B **71**, 115307 (2005). https://doi.org/10.1103/PhysRevB.71.115307

[28] H. C. Tso, P. Vasilopoulos, and F. M. Peeters, *Coulomb Coupling between Spatially Separated Electron and Hole Layers: Generalized Random-Phase Approximation*, Phys. Rev. Lett. **70**, 2146 (1993). https://doi.org/10.1103/PhysRevLett.70.2146

[29] A.-P. Jauho and H. Smith, *Coulomb Drag between Parallel Two-Dimensional Electron Systems*, Phys. Rev. B **47**, 4420 (1993). https://doi.org/10.1103/PhysRevB.47.4420

[30] H. C. Tso, P. Vasilopoulos, and P. M. Peeters, *Coupled Electron-Hole Transport: Generalized Random-Phase Approximation and Density Functional Theory*, Surf. Sci. **305**, 400 (1994). https://doi.org/10.1016/0039-6028(94)90925-3

[31] R. Pillarisetty, H. Noh, E. Tutuc, E. P. De Poortere, D. C. Tsui, and M. Shayegan, *Spin Polarization Dependence of the Coulomb Drag at Large ${r}_{s}$*, Phys. Rev. Lett. **94**, 16807 (2005). https://doi.org/10.1103/PhysRevLett.94.016807

[32] S. Kim, I. Jo, J. Nah, Z. Yao, S. K. Banerjee, and E. Tutuc, *Coulomb Drag of Massless Fermions in Graphene*, Phys. Rev. B **83**, 161401 (2011). https://doi.org/10.1103/PhysRevB.83.161401

[33] T. Vazifehshenas and T. Salavati-fard, *Inelastic Coulomb Scattering Rate within the Finite-Temperature Hubbard Approximation*, Phys. Scr. **81**, 25701 (2010). https://doi.org/10.1088/0031-8949/81/02/025701

[34] T. Salavati-fard and T. Vazifehshenas, *Local Field Correction Effect on Inelastic Coulomb Scattering Lifetime of Two-Dimensional Quasiparticles at Low Temperatures*, Phys. B Condens. Matter **406**, 1883 (2011). https://doi.org/10.1016/j.physb.2011.02.047

Spectrum Analysis of Mesons using Nikiforov-Uvarov Functional Analysis Method

Vinod Kumar[1,a], Ram Mehar Singh[1,b], S.B. Bhardwaj[2,c], Fakir Chand[3,d,*]

[1]Department of Physics, Chaudhary Devi Lal University, Sirsa – 125055, India

[2]Department of Physics, S. U. S. Govt College, Matak Majri, Karnal – 132001, India

[3]Department of Physics, Kurukshetra University, Kurukshetra - 136119, India

[a]vk337727@gmail.com, [b]dixit_rammehar@yahoo.co.in, [c]sbnit@gmail.com, [d]fchand@kuk.ac.in

Keywords: Schrodinger Equation, CPP Potential, NUFA Method, Mesons, Mass-Spectra

Abstract. The analytical expressions for the energy eigenvalues and eigenfunctions are computed for Coulomb perturbed potential by solving the Schrodinger equation within the framework of the Nikiforov-Uvarov functional analysis method and applying the Greene-Aldrich approximation. Using the energy eigenvalue expression, we have determined the mass spectra of $c\bar{s}$ and $\bar{b}c$ mesons. The results of present study are in good agreement with experimental, relativistic and other relevant works available in the literature.

Introduction

As we know that most of the quantum mechanical systems can be studied by determining the bound state solutions to Schrodinger equation (SE) within a suitable potential model. Thereby, within the framework of an appropriate potential model and a proper mathematical approach, one can understand the behaviors of quantum mechanical systems. Such theoretical models also help to investigate the complicated structures, the mass spectra and radiative transitions width of various mesons. In non-relativistic quantum mechanics, experimentally observed vital physical properties can be reproduced with a suitable interaction potential model which, in general, is a function of relative separation between quark and antiquark pairs. In literature, there exist several important studies related to computation of mass spectra of mesons; a brief of those is as follows.

Inyang et. al. [1] studied a temperature dependent Yukawa potential by replacing the screening parameter with the Debye mass and obtained mass spectra of heavy mesons by solving the SE with series expansion method. Moazami et. al [2] solved the SE with the Cornell potential and calculated the mass spectra of some mesons. Using power series and asymptotic iteration method, Ramesh et. al [3, 4] calculated the mass spectra of charmonium and bottomonium by solving the N-dimensional SE. By considering a generalized interaction potential, Richa et. al [5] solved the SE via asymptotic iteration method and calculated the mass spectra of some heavy and light mesons. Some other important studies related to mass spectra of mesons are available in refs. [6-9].

So, to obtain better results for meson systems, here, we use the Coulomb perturbed potential (CPP) as an interaction potential i.e.

$$V(r) = ar^2 + br - \frac{c}{r}, \qquad (1)$$

where a, b and c are potential parameters and should be chosen appropriately such that the obtained results be comparable with available experimental and other theoretical outcomes.

Formalism

In literature, there are many robust and easy to apply mathematical techniques to solve the SE with exactly or approximately. Such approaches include Nikiforov Uvarov (NU) method [10], Lie algebraic approach [11], asymptotic iteration method (AIM) [12], parametric Nikiforov Uvarov (pNU) method [13], and many others. Here in our present calculations, however we have utilized a relatively new method, the Nikiforov Uvarov functional analysis (NUFA) method [14].

The non-relativistic radial SE for the potential (1) is written as

$$\frac{d^2R(r)}{dr^2} + \frac{2\mu}{\hbar^2}\left(E - ar^2 + br + \frac{c}{r} - \frac{l(l+1)\hbar^2}{2\mu r^2}\right)R(r) = 0 \tag{2}$$

Now by invoking the Greene-Aldrich approximation [15] for the centrifugal term

$$\frac{1}{r^2} \approx \frac{\alpha^2}{(1-e^{-\alpha r})^2} \ , \tag{3}$$

E q. (2) reduces to

$$\frac{d^2R(r)}{dr^2} + \frac{\alpha^2}{(1-e^{-\alpha r})^2}\left[\frac{2\mu E(1-e^{-\alpha r})^2}{\hbar^2\alpha^2} - \frac{2\mu a(1-e^{-\alpha r})^4}{\hbar^2\alpha^4} - \frac{2\mu b(1-e^{-\alpha r})^3}{\hbar^2\alpha^3} + \frac{2\mu c(1-e^{-\alpha r})}{\hbar^2\alpha} - l(l+1)\right]R(r) = 0 \tag{4}$$

By putting $s = e^{-\alpha r}$ in above equation and neglecting higher powers of 's' in the resultant expression, we obtain

$$\frac{d^2R(r)}{dr^2} + \frac{1}{s}\frac{dR(s)}{ds} + \frac{1}{s^2(1-s)^2}\left[\left(\frac{2\mu E}{\hbar^2\alpha^2} - \frac{12\mu E}{\hbar^2\alpha^4} - \frac{6\mu b}{\hbar^2\alpha^3}\right)s^2 + \left(\frac{8\mu a}{\hbar^2\alpha^2} - \frac{4\mu E}{\hbar^2\alpha^2} + \frac{6\mu b}{\hbar^2\alpha^3} - \frac{2\mu c}{\hbar^2\alpha}\right)s + \left(\frac{2\mu E}{\hbar^2\alpha^2} - \frac{2\mu a}{\hbar^2\alpha^4} - \frac{2\mu b}{\hbar^2\alpha^3} + \frac{2\mu c}{\hbar^2\alpha} - l(l+1)\right)\right]R(s) = 0 \ . \tag{5}$$

Eq. (5) can further be written as

$$\frac{d^2R(r)}{dr^2} + \frac{1}{s}\frac{dR(s)}{ds} + \frac{1}{s^2(1-s)^2}[-\xi_1 s^2 + \xi_2 s - \xi_3]R(s) = 0, \tag{6}$$

where,

$$\xi_1 = -\frac{2\mu E}{\hbar^2\alpha^2} - \frac{12\mu E}{\hbar^2\alpha^4} - \frac{6\mu b}{\hbar^2\alpha^3} = -\frac{2\mu E}{\hbar^2\alpha^2} + \tau_1 \ , \tag{7a}$$

$$\xi_2 = -\frac{4\mu E}{\hbar^2\alpha^2} + \frac{6\mu b}{\hbar^2\alpha^3} - \frac{2\mu c}{\hbar^2\alpha} + \frac{8\mu a}{\hbar^2\alpha^2} = -\frac{4\mu E}{\hbar^2\alpha^2} + \tau_2 \ , \tag{7b}$$

$$\xi_3 = -\frac{2\mu E}{\hbar^2\alpha^2} + \frac{2\mu a}{\hbar^2\alpha^4} + \frac{2\mu b}{\hbar^2\alpha^3} - \frac{2\mu c}{\hbar^2\alpha} + l(l+1) = -\frac{2\mu E}{\hbar^2\alpha^2} + \tau_3 \ . \tag{7c}$$

Comparing Eq. (5) with the following standard equation of NUFA method [14]

$$\frac{d^2\psi(s)}{ds^2} + \frac{\alpha_1 - \alpha_2 s}{s(1-\alpha_3 s)}\frac{d\psi(s)}{ds} + \frac{1}{s^2(1-\alpha_3 s)^2}[-\xi_1 s^2 + \xi_2 s - \xi_3]\psi(s) = 0, \tag{8}$$

one can obtain

$\alpha_1 = \alpha_2 = \alpha_3 = 1,$

$\mu_1 = \sqrt{\varepsilon + \tau_3}\,,$

$$\nu_1 = \frac{1}{2} + \frac{1}{2}\sqrt{1 + 4(\tau_1 - \tau_2 + \tau_3)}\ . \tag{9}$$

The equation for finding the energy eigenvalue using the NUFA method [14] is given as

$$\mu_1^2 + 2\mu_1\left(\nu_1 + \frac{\alpha_2}{\alpha_3} - 1 + \frac{1}{\sqrt{\alpha_3}}\right) + \left(\nu_1 + \frac{\alpha_2}{\alpha_3} - 1 + \frac{1}{\sqrt{\alpha_3}}\right)^2 - \left(\frac{\alpha_2}{\alpha_3} - 1\right) - \frac{\xi_1}{\alpha_3^2} = 0. \tag{10}$$

Using Eqs. (7a) and (9) in eq. (10), the energy eigenvalue expression for the CPP is written as

$$E = -\frac{\hbar^2\alpha^2}{2\mu}\left[\frac{(-(\nu_1+n)^2 + \tau_1 - \tau_3)}{2(\nu_1+n)}\right]^2 + \frac{\hbar^2\alpha^2\tau_3}{2\mu}; \tag{11}$$

and the corresponding eigen function is thus written as

$$R_n(r) = N(e^{-\alpha r})^{\sqrt{\varepsilon+\tau_3}}(1 - e^{-\alpha r})^{\frac{1}{2}\pm\frac{1}{2}\sqrt{1+4(\tau)}} \times 2F_1(-n, n + 2(\mu_1 + \nu_1), 1 + 2\mu_1; e^{-\alpha r}). \tag{12}$$

Spectrum Analysis of Mesons

So, in order to calculate the mass spectra of mesons, we exploit the following well known equation [4]

$$M = m_q + m_{\bar{q}} + E_{nl}, \tag{13}$$

here m_q and $m_{\bar{q}}$ are the masses of quark and antiquark respectively. Thus, by using Eq. (11) in the above equation, we determine the equation for finding the mass spectra of mesons as

$$M = m_q + m_{\bar{q}} - \frac{\hbar^2\alpha^2}{2\mu}\left[\frac{(-(\nu_1+n)^2 + \tau_1 - \tau_3)}{2(\nu_1+n)}\right]^2 + \frac{\hbar^2\alpha^2\tau_3}{2\mu}\ . \tag{14}$$

Further, to check the correctness of analytical results, we have calculated mass spectra of $c\bar{s}$ and $\bar{b}c$ mesons by considering m_b =4.823 GeV, m_s =0.419 GeV and m_c =1.209 GeV. The numerical values of the potential parameters are taken from ref. [5].
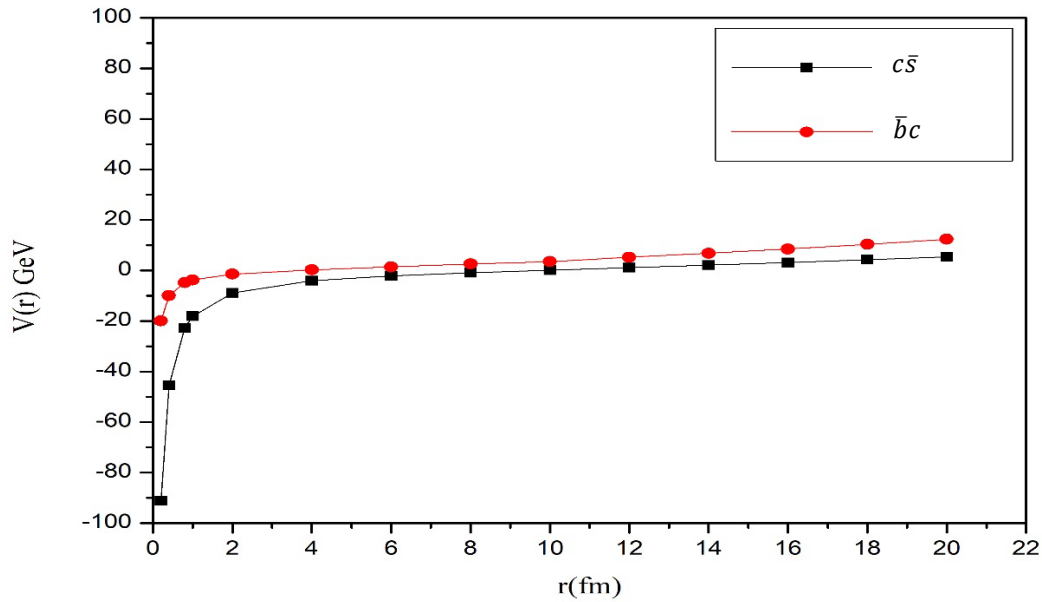
Fig. 1: Behavior of Coulomb perturbed potential with 'r'.

Table 1: *Mass spectra of cs̄ in GeV (a = 0.0123 GeV³, b= 0.0688 GeV², c = 18.2252, α=0.0725, μ= 0.3111 GeV)*

State	Present Work	Experimental [9]	Relativistic [6]	Ref. [5]	Ref. [16]
1S	2.517	-	2.129	2.512	1.968
1P	2.548	-	2.549	2.649	2.565
1D	2.610	2.859	2.899	2.859	2.857
2S	2.755	2.709	2.732	2.709	2.709
2P	2.784	-	3.018	2.860	-
3S	2.956	-	3.193	2.906	2.932
4S	3.124	-	3.575	3.102	-

Table 2: *Mass spectra of $\bar{b}c$ in GeV (a = 0.0204 GeV³, b = 0.2209 GeV², c = 4.0087, α=0.2187, μ = 0.9666 GeV)*

State	Present Work	Experimental [8]	Relativistic [7]	Ref. [5]	Ref. [16]
1S	6.277	6.277	6.332	6.277	6.277
1P	6.365	-	6.734	6.340	7.042
1D	6.531	-	7.072	6.452	-
2S	6.460	-	6.881	6.814	7.383
2P	6.532	-	7.126	6.851	6.663
3S	6.558	-	7.235	7.235	7.206
4S	6.591	-	-	7.889	-

Concluding Remarks

Here, we have explored the NUFA method for solving the Schrodinger equation and obtained analytical expressions for the bound state energy eigenvalues and eigenfunctions within the framework of the Coulomb perturbed potential. To check the suitability of the choice of potential and applicability of the NUFA-method, we utilized the energy eigenvalue expression (11) to compute the mass spectra of $c\bar{s}$ and $\bar{b}c$ mesons with suitable values of potential parameters chosen from literature. The obtained results are comparable with the earlier published results of similar studies. The behaviour of the Coulomb perturbed potential with separation 'r' is also plotted in Fig.1

Conflicts of interests

The authors declare no conflict of interest.

Acknowledgement

References

[1] Inyang, E.P., Akpan, I.O., Ntibi, J.E. and William, E.S., *Eur. J. Appl. Phy. 2(6) (2020)*. https://doi.org/10.24018/ejphysics.2020.2.6.26

[2] Moazami, M., Hassanabadi, H. and Z. Kumar, S., *Few-Body Sytm.*, *59* (5), 2018. https://doi.org/10.1007/s00601-018-1422-7

[3] Kumar, R. and Chand, F., *Phy. Scr.*, *85*(5), 055008 (2012). https://doi.org/10.1088/0031-8949/85/05/055008

[4] Kumar, R. and Chand, F., *Comm. Theor. Phy.*, *59*(5), 2013. https://doi.org/10.1088/0253-6102/59/5/02

[5] Rani, R., Bhardwaj, S.B. and Chand, F., *Comm. Theor. Phy.*, *70*(2), 179 2018. https://doi.org/10.1088/0253-6102/70/2/179

[6] Godfrey, S. and Moats, K., *Phy. Rev. D*, *93*(3), 034035 (2016). https://doi.org/10.1103/PhysRevD.93.034035

[7] Ebert, D., Faustov, R.N. and Galkin, V.O., *Phy. Rev. D*, *67*(1), 014027 (2003). https://doi.org/10.1103/PhysRevD.67.014027

[8] Beringer, J. et. al, *Phy. Rev. D-Particles, 86*(1), 010001 (2012).

[9] Godfrey, S. and Moats, K., *Phy. Rev. D*, *90*(11), 117501 (2014). https://doi.org/10.1103/PhysRevD.90.117501

[10] Nikiforov, A.F. and Uvarov, V.B., *Special functions of mathematical physics* (Vol. 205) Springer, 1988. https://doi.org/10.1007/978-1-4757-1595-8

[11] Panahi, H., Z. Kumar, S. and Baradaran, M., *Eur. Phy. J. Plus*, *131*(2), 1 (2016). https://doi.org/10.1140/epjp/i2016-16035-5

[12] Boztosun, I., Bonatsos, D. and Inci, I., *Phy. Rev. C*, *77*(4), 044302 (2008). https://doi.org/10.1103/PhysRevC.77.044302

[13] Tezcan, C. and Sever, R., *Int. J. Theo. Phy.*, *48*(2), 337 (2009). https://doi.org/10.1007/s10773-008-9806-y

[14] Ikot, A.N., Okorie, U.S., Amadi, P.O., Edet, C.O., Rampho, G.J. and Sever, R., *Few-Body Sys.*, *62*(1), 1 (2021). https://doi.org/10.1007/s00601-021-01593-5

[15] Jia, C.S., Chen, T. and He, S., *Phy. Lett. A*, *377*(9), 682 (2013). https://doi.org/10.1016/j.physleta.2013.01.016

[16] Abu-Shady, M., Abdel-Karim, T.A. and Ezz-Alarab, S.Y., *J. Egypt. Math. Soc.*, *27*(1), 1 (2019). https://doi.org/10.1016/j.physleta.2013.01.016

Evaluation of Bloch–Gruneisen Function to Determine the Electrical Resistivity for Pure Nano-MgB₂ Superconductor

Intikhab A. Ansari[a] [*], C.V. Rao[b]

Department of General Studies, Jubail Industrial College, P. O. Box - 10099, Jubail Industrial City-31961, Saudi Arabia

[a]ansari_i@jic.edu.sa, [b]cvrao@jic.edu.sa

Keywords: Incomplete Gamma Function, Debye Temperature, Bose–Einstein Statistics

Abstract. Here, the generalized Bloch–Gruneisen (BG) function is described with wide range of temperatures in addition with some other parameters. This function shows the easy and precise method to determine the resistivity as a function of temperature for pristine nano-MgB₂ sample. The fitted outcomes are in resemblance with the experimental results up to 20–150 K temperature range. This generalized BG function is appropriate for diverse non-integers and integers values of *n*. Experimental result is full agreement with the fitted data for *n* = 4 integer value. Furthermore, the present method exposes the accuracy, easiness and preciseness of the results up to a high order of decimals for the determination of the resistivity as a function of temperature.

Introduction

In solid-state physics, the Bloch–Gruneisen (BG) function is the essential term which describes the contribution of phonon resistivity. BG-like behavior exhibits the influence of *e–ph* interaction on the electrical transport of nanowires [1,2] and nano-films [3,4]. The electrical resistivity has been measured with the help of the incomplete gamma function for pure nano-MgB₂ superconductor in the previous report [5]. The novelty of the present work is that we have adopt the different approach to calculate the BG function with more accuracy and preciseness rather than previous work [5]. In nonmagnetic crystalline materials, the electrical resistivity as a function of temperature, $\rho\,(T)$ is defined by the Bloch–Gruneisen formula [6,7] as given below:

$$\rho\,(T) = A\left(\frac{1}{p}\right)^n \int_0^p \frac{x^n}{(e^x-1)(1-e^{-x})}\,dx, \tag{1}$$

where $p = (\theta_D/T)$ and T is the applied temperature and θ_D is the Debye temperature which obtained from heat capacity calculations. The above Eq. (1) is applicable not only for integers, n but also for non-integers that has strong relation with dominant scattering mechanism [8]. The right side function in the above Eq. (1) can be re-written as:

$$J\left(\frac{1}{p}\right) = \int_0^p \frac{x^n e^{-x}}{(1-e^{-x})^2}\,dx \tag{2}$$

Most terms of equation (2) extracted from the Bose–Einstein statistics [9-11] depends upon the kind of particles either phonons or magnons. In some literature BG function has broadly used for MgB₂ sample to demonstrate the accuracy of the method [12,13].

In this study, we have evaluate the temperature dependence of resistivity for nano-MgB₂ superconductor by using BG function which is the important factor to understand the mechanism of the lattice behavior. The BG function can be solve for different non-integer and integer values

of n. The above Eq. (2) is further elaborated and numerical results attained from this equation are studied and compared experimentally for resistivity as a function of temperature which are in agreement with the previous study.

Numerical Solution of Bloch-Gruneisen Model
Currently, MgB_2 superconductor is widely well-known by the scientists due to its inexpensive material cost, easy synthesis method and distinctive transport and electrical properties. Its transition temperature, T_c is the maximum among phonon-mediated superconductors. The crystalline structure of MgB_2 is simple as graphite structure and layered like high-T_c cuprate superconductor; whereas pristine cuprates are insulators at ambient temperatures, however, MgB_2 shows the metallic behavior. It contains the hexagonal planes of B atoms sandwiched by the planes of Mg atoms.

The electrical resistivity as a function of temperature for nano-MgB_2 is an important factor which describes the electron-phonon interaction within a matrix of the superconductor. The BG function precisely explicates the role of e–ph interaction by the aforementioned Eq. (1).

$$\text{Let} \quad y(x) = \frac{x^n e^{-x}}{(1-e^{-x})^2} \tag{3}$$

Applying Simpson's rule, for $y = f(x)$ in the internal $[a, b]$

$$I = \int_a^b f(x)\ dx \tag{4}$$

Divide $[a, b]$ into an even number of equal intervals.

$$I = \frac{h}{3}[(y_0 + y_N) + 4(y_1 + y_3 + \cdots) + 2(y_2 + y_4 + \cdots)] \tag{5}$$

$$y_0 = \lim_{x \to 0} y(x) = \lim_{x \to 0} \frac{x^n e^{-x}}{(1-e^{-x})^2} \tag{6}$$

The above expression is in indeterminate form, therefore applying the L' Hospital's rule we get $y_0 = 0$.

$$J\left(\frac{1}{p}\right) = \int_0^p y\ dx \tag{7}$$

where $\quad h = \frac{p}{N}$ and $N = 800$

$$J\left(\frac{1}{p}\right) = \frac{h}{3}\left[y_N + 4\sum_{i=0}^{\frac{N}{2}} y((2i-1)h) + 2\sum_{k=0}^{\frac{N}{2}-1} y(2kh)\right] \tag{8}$$

We have expressed below the resistivity as a function of temperature of nano-MgB_2 for generalized BG function as evaluated above in series form. The general form of BG function can be analyzed as [13]:

$$\rho\ (T) = A\left(\frac{1}{p}\right)^n J\left(\frac{1}{p}\right) \tag{9}$$

Here coefficient A is related with the temperature based resistivity in Eq. (9). The parameters θ_D = 1150 K and A = 230 μΩ-cm are the polynomial fit parameters. The parameter n used in the present work has nearly fitting for the range 3–6 in the normal-state of the nano-MgB$_2$ sample that is in good agreement with the previous report [3]. The resistivity as a function of temperature of nano-MgB$_2$ is then accomplished with the help of Eq. (9) for non-integer and integer values of n = 3–6.

Results and Discussion

We demonstrates the accuracy and preciseness of aforementioned method in the present work. Table 1 shows the result of the Eq. (8) for integer n = 6 while Table 2 depicts the result of Eq. (8) for diverse non-integer and integer values of n. The proposed method described above in this present study is suitable for calculating the resistivity as a function of temperature up to high accuracy of preciseness. The evaluated outcomes achieved in these tables are in agreement with the previous report [3]. These tables illustrate the extensively high precise results for integer and non-integer auxiliary values of variables. We have constructed the algorithm in MATLAB to evaluate the BG function of Eq. (8) for integer and non-integer values of n that is displayed in Table 1 and 2. In addition, the proposed algorithm of BG function used here is favorable for calculating the temperature dependence of resistivity up to high order of decimals for pure nano-MgB$_2$. Fig. 1, evaluates the variation of temperature dependence of resistivity, ρ (T) for pristine nano-MgB$_2$ superconductor with temperature range 20–250K for integer values n = 3–6. It is noticed that the experimental resistivity data is in agreement with the fitted parameter n = 4 up to temperature 150 K at normal-state of pristine nano-MgB$_2$. In addition, it is observed that at lower temperature the experimental results are very much closer to the other fitted parameter integers of n = 3, 5 and 6 for this particular sample. The ρ (T) of fitted parameters are diverging after 150 K temperature. It is remarkable that the proposed BG function evaluated here is suitable to determine the resistivity as a function of temperature is articulated by Eq. (9) for different non-integer and integer values of n. It is remarkable that parameter A in Eq. (9) for pure nano-MgB$_2$ might be associated with the lattice distortion near the grain boundaries.

Table 1: *The determined BG function J (T/θ_D) with Eq. (8) for n = 6 and N = 800*

T	θ_D	Eq. (8)
35	180	1.97681054433016E+02
170	1420	5.36481589414526E+02
20	154	4.79434564949680E+02
18	107	2.88975219380716E+02
95	56	1.39443352569230E-02
70.8	520.5	4.45300544545428E+02
52	21	2.12764884053156E-03
55.3	354.6	3.43090699182929E+02
112	112	1.88543602757016E-01
117	1180	6.42597123150886E+02

Table 2: *Evaluated BG function J (T/θ_D) for N = 800 with different n values*

T	θ_D	n	Eq. (8)
24.2	114	4	3.53047917392598E-02
45.4	316	5.5	1.85842043705552E+02
112.3	262.6	7.43	2.62774301572033E+01
32.4	211.7	8.7	2.78998060604394E+04
61.3	312.2	11	2.56537347825103E+05
79.1	108.3	12	2.52940908796277E+00
234	832	13	1.49033930140852E+05
278	1121	7	2.91946361395975E+02
118	437	9	1.93515335158151E+03
527	3274	21	3.53588752223842E+013
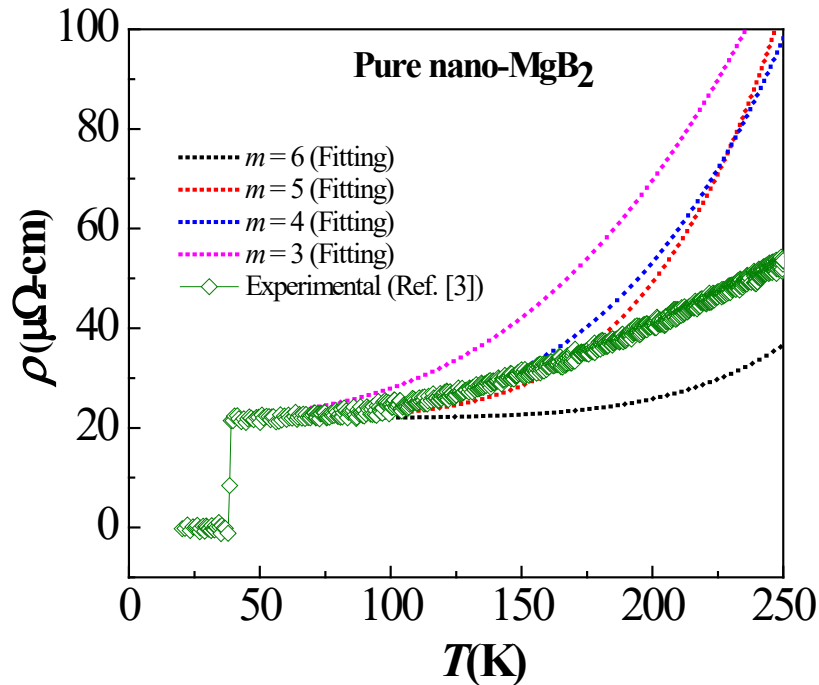
Figure 1: *Comparison of experimental and fitted measured resistivity as a function of temperature with varying n = 3, 4, 5 and 6 for pure nano-MgB$_2$ superconductor.*

Conclusions

Conclusively, we have evaluated the BG function with integer and non-integer values of n = 3, 4, 5 and 6. To obtained the resistivity as a function of temperature, $\rho(T)$ for pure nano-MgB$_2$ superconductor at normal-state this BG function reveals more accuracy and preciseness. The experimental outcomes are consistent with the fitted value of n = 4 up to 20–150 K. The proposed method shows the significant results and easy technique for the calculation of BG function rather than complex method. The novelty of this technique is that we can use this generalized BG function for other superconductors as well.

References

[1] S. S. Kubakaddi, Electron-phonon interaction in a quantum wire in the Bloch-Gruneisen regime. Phys. Rev. B 75 (2007) 075309. https://doi.org/10.1103/PhysRevB.75.075309

[2] A. Bid, A. Bora, and A. Raychaudhuri, Temperature dependence of the resistance of metallic nanowires of diameter $\geq$ 15 nm: Applicability of Bloch-Gruneisen theorem, Phys. Rev. B 74 (2006) 035426. https://doi.org/10.1103/PhysRevB.74.035426

[3] I. A. Ansari et al., Enhancement of critical current density for nano (n)–ZnO doped MgB_2 superconductor, Physica C 495 (2013) 208-212. https://doi.org/10.1016/j.physc.2013.10.001

[4] L. Mazov, High-field evidence for the Bloch-Gruneisen curve in the cuprates, Phys. Rev. B 70 (2004) 054501. https://doi.org/10.1103/PhysRevB.70.054501

[5] I. A. Ansari, The Analytical Solution of Incomplete Gamma Function to Determine the Electrical Resistivity at Normal State for MgB_2 Superconductor, Journal of Physics: Conference Series 1172 (2019) 012028. https://doi.org/10.1088/1742-6596/1172/1/012028

[6] J. M. Ziman (Eds.), Electrons and Phonons, Clarendon, Oxford University Press (2001). https://doi.org/10.1093/acprof:oso/9780198507796.001.0001

[7] J. Bass, Jr. W. P. Pratt and P. A. Schroeder, The temperature-dependent electrical resistivities of the alkali metals, Rev. Modern Phys. 62 (1990) 645–744. https://doi.org/10.1103/RevModPhys.62.645

[8] D. Varshney and N. Kaurav, Interpretation of Temperature-Dependent Resistivity of La-Pb-MnO_3: Role of Electron-Phonon Interaction, J. Low Temp. Phys. 141 (2005) 165–178. https://doi.org/10.1007/s10909-005-8226-0

[9] P. A. M. Dirac, On the Theory of Quantum Mechanics, Proceedings of the Royal Society, *Series A* 112 (762) (1926) 661-677. https://doi.org/10.1098/rspa.1926.0133

[10] S. N. Bose, "Plancks Gesetz und Licht quanten hypothese", Zeitschrift für Physik 26 (1924) 178-181. https://doi.org/10.1007/BF01327326

[11] David J. Griffiths, Introduction to Quantum Mechanics (2nd Ed.), Upper Saddle River, New Jersey, Pearson, Prentice Hall (2005)

[12] J-Q Shen, M-H Fang, Y. Zheng, H-T Wang, Y. Lu and Z-A Xu, **2003**. Study of high temperature resistivity and thermal stability of superconductor MgB_2, Physica C 386 (2003) 663-666. https://doi.org/10.1016/S0921-4534(02)02189-5

[13] A. Poddar et al., Studies of transport properties of MgB_2 superconductor, Physica C 390 (2003) 191-196. https://doi.org/10.1016/S0921-4534(03)00961-4

Effect of Various Process Parameter of GTA Cladding on Surface Properties of Mild Steel: A Critical Review

Sujeet Kumar[a,*], Anil Kumar Das[b]

Department of Mechanical Engineering, National Institute of Technology Patna, Bihar, 800005, India

[a] sujeetk65@gmail.com, [b] akdas.mechnitp@gmail.com

Keywords: GTA Cladding, Composite, Coating, Mild Steel, In-Situ Method, Microhardness, Wear Resistance, Microstructure, Nitrogen, Shielding Gas

Abstract. Mild steel has considerable importance in the field of engineering due to its high strength, good mechanical properties and low cost. However, its application is restricted in some industries where wear failure is considered as major problem. Wear attacks on the moving components from the upper surface, which proves wear is often a surface phenomenon. Many researchers have used the gas tungsten arc (GTA) cladding process to deposit a thick alloy layer, metal matrix composite layer and ceramic composite layer on low carbon steel substrate due to its high deposition efficiency, inexpensive, easy to operate and good performance. The metal matrix composite (MMC) coating makes the components reusable because of the synergetic effect of the combination of hard reinforcement and ductile matrix. Researchers also investigated that the deposition of hard coating synthesized by the in-situ method gives better properties rather than the ex-situ method due to the mismatch of the wetting properties between the various phases of ceramics materials during the ex-situ method. This review paper summarizes the literature related to the GTA cladding on mild steel and its applications. Further, it was also described here about the effect of coating materials, process parameters of GTA cladding on surface properties of mild steel such as resistance to wear, corrosion resistance and hardness. This review paper will provide reference for the researchers working in the GTA cladding area.

Introduction

In many industries, mild steel components have been used in various conditions such as high speed, load, chemical condition and elevated temperature or combination of these. Due to high strength, toughness and relatively low coast of the mild steel, it is frequently used for structural engineering components. However, it is restricted to use mild steel in some industries because of its miserable surface properties such as wear, corrosion, oxidation resistance and microhardness [1-3]. Thus, a surface treatments technique required to enhance surface properties of the mild steel. There are three different surface treatments available for steel such as thermal treatments, thermo-chemical treatments and surface coating. Thermal hardening such as flame and induction hardening, enhance the surface properties by modifying microstructure without altering its surface chemistry. This method is not suitable for mild steel. Thermal hardening is restricted to use on the steel that have carbon content less than 0.5 % [4]. Thermo-chemical treatments such as carburizing, boriding and nitriding, improve the surface properties by modifying microstructure as well as surface chemistry of the steel. It modify the surface properties and tribological properties of steel. This process also restricted to use due to processing on very high temperature and high case depth. Due to processing at high temperature can occurs oxidation on the surface and distortion of the steel components [5-6]. Surface coating involves melting of the coating powder with preferable composition and thin substrate surface deposition of dense coating layer on the substrate [7]. There

are various surface coating process such as physical vapour deposition (PVD), chemical vapour deposition (CVD), cladding by electron beam, laser beam coating, gas tungsten arc (GTA) coating/cladding, plasma arc coating and thermal spraying. Among these surface coating techniques, GTA coating gained much attention due to following advantages such as easy to operate, abundance availability and low cost [8]. It not only provide better microstructure and tribological as well as surface properties but also remarkably improved the powder utilization as well as cladding efficiency [9].

Numerous researchers improve the surface properties of the substrate by depositing the various types of ceramic composite and metal matrix composite by GTA cladding. Metal matrix composite provides the combination of the properties of metals (soft phase) as well as ceramic reinforcements (hard phase) that are not provide by a single ceramic reinforcement materials. Many authors reported about the various metal matrix composite such as $Ni–TiC-TiB_2$, $Fe–Al_2O_3–TiB–TiN$, $Fe–TiB_2–TiN–BN$, $Al_2O_3–TiB_2–TiC$ etc [10-12].

Wear and corrosion is the failure mode of the mechanical components that working under moving condition and chemical environment. Coating of the base metal is one of the most effective idea to restrict the corrosion as well as wear of the base metal. Coated layer provide the obstacle between the base metal and environment in the existence of corrosion or chemicals. For providing adequate protection against wear and corrosion, coating layer should be free of voids or pore, uniform layer and well adhered. Coating successfully increases the service life of the components by providing high wear resistance and corrosion resistance to the components [13, 14].

The purpose of the present study is to collect the information about GTA cladding on mild steel. This paper also demonstrate the effect of the various process parameters of GTA cladding and coating materials on the microstructure of the coating and properties of the coated materials such as microhardness, wear resistance and corrosion resistance. Authors explored the feasibility of deposition of crack and pores free GTA coating on the mild steel substrate.

GTA cladding process

Gas tungsten arc cladding process has been used for depositing the coating layer on the mild steel. In this process, non-consumable tungsten electrode used to accomplish the heating to melt the preplaced layer and substrate surface simultaneously. The schematic diagram of GTA cladding on the mild steel substrate shows in Fig. 1. It also shows the coated tracks, preplaced layer as well as passage for shielding gas in the GTA nozzle.

During cladding the clad zone is protected by the use of shielding gas such as argon gas, nitrogen gas etc. [15]. The tool travel speed controlled by the automatic GTA cladding or use of moving machine attached with torch holding device. A flow chart shown in Fig. 2 that show the deposition of coating on the mild steel substrate using GTA coating technique.
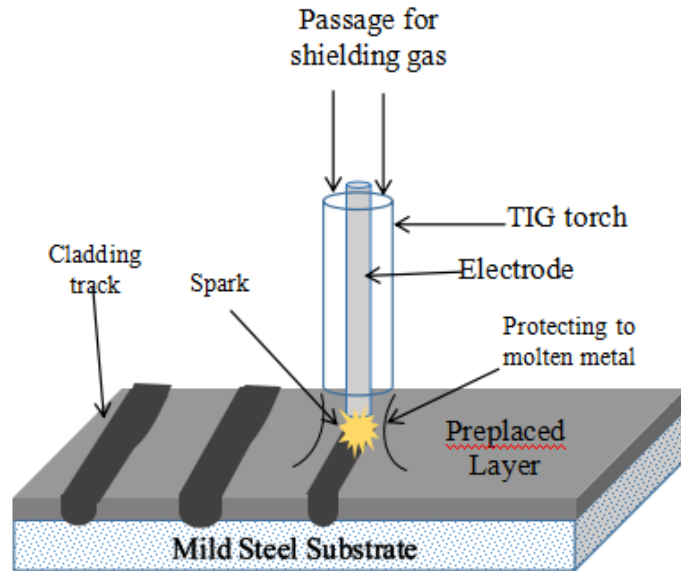
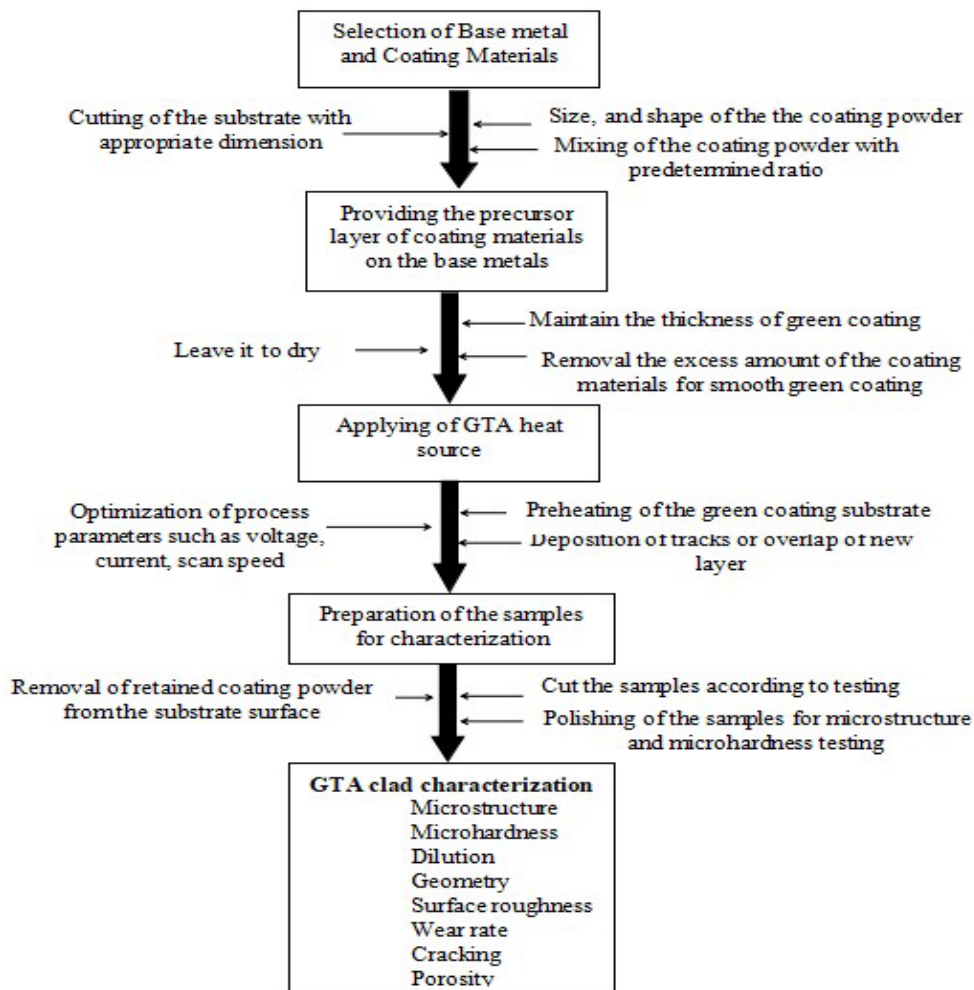*Fig 1. The setup diagram of the gas tungsten gas (GTA) cladding*

Fig. 2 Flow chart of deposition of coating layer using GTA cladding

Influence of process parameters of GTA cladding on surface properties of mild steel
Numerous researchers have deposited the coating layer on the mild steel using GTA cladding and have reported the influence of process parameters of GTA cladding such as input current, voltage, scan speed, shielding gas, different coating materials etc. on the surface properties of mild steel.

Shielding gas
During gas tungsten arc (GTA) cladding, different type of shielding gas used such as argon, nitrogen, carbon dioxide (CO_2) to shield the molten metal from the environment. The shielding gas is a factor that directly affect the microhardness and quality of coating layer. Hojjatzadeh et al. (2012) deposited the ferrotitanium coating layer on AISI 1045 steel with shielding gas of $100\%N_2$, $70\%N_2$–$30\%Ar$, $40\%N_2$–$60\%Ar$, $20\%N_2$–$80\%Ar$ and $100\%Ar$ using GTA cladding. Authors noticed that the increasing of nitrogen content with argon shielding gas promoted the arc voltage therefore the heat input also increases. This high specific heat input directly enlarged the cross section area and penetration depth as show in Fig. 3. High amount of nitrogen gas in the shielding gas promoted the larger dilution of the substrate that leads to decreases in hardness value of coated samples.They also noticed that the porosity observe on the outer layer of the coating with high contents of nitrogen and eliminated with less than 40 % nitrogen content [16].
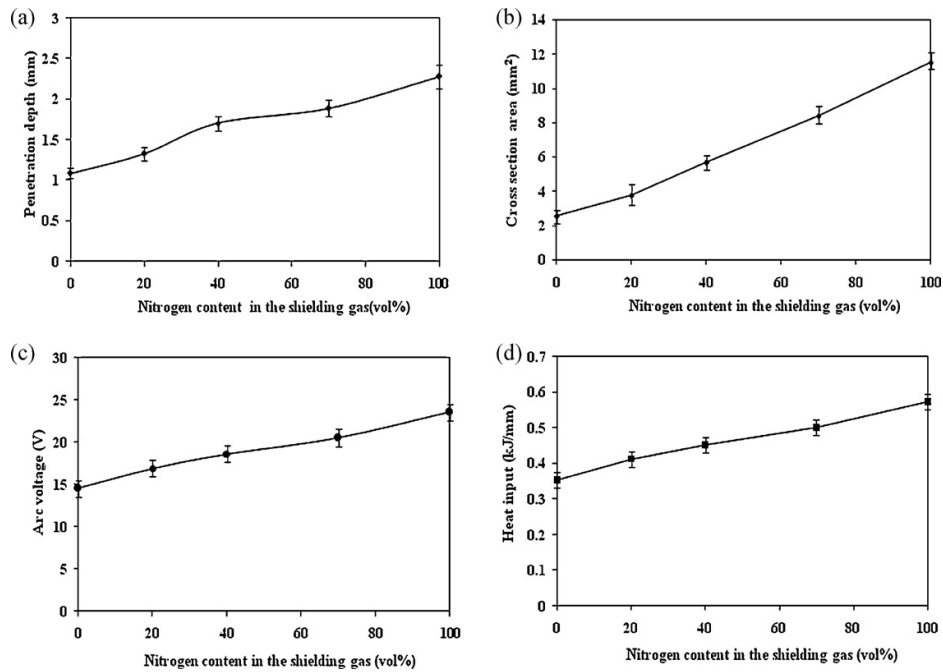
Fig. 3 Influence of nitrogen gas content on the (a) depth of penetration of the tracks, (b) cross section area, (c) arc voltage of GTA cladding and (d) GTA heat input during coating [16]

Huang (2009) also investigated the effect of nitrogen increment in the shielding gas with and without activating flux on properties of GTA weldments. They reported that the heat input promoted with increasing the nitrogen content in the protecting gas therefore penetration depth increases [17]. Dyuti et al. (2010) also synthesized the TiAlN cladding by TIG cladding on mild steel substrate using pure nitrogen shielding gas. It was noticed that some pores also present in the nitrided layers [18].

Input current and voltage of GTA cladding

The GTA cladding utilized to melt the preplaced layer and substrate surface and deposit a new layer on the substrate. The heat input of GTA cladding depends upon the input current, voltage and torch scanning speed. The heat input calculated by the following formula [19];

Heat Input = (0.48 × current × voltage) / (scan speed)   ……..   (1)

Dyuti et al. (2010) deposited the Ti and Al composited coating on the mild steel substrate using different heat input of TIG cladding. It was found that the melt of the coating depends upon the heat input as well as voltage and current of TIG. Glazing directly depends upon the current and voltage whereas inversely proportional to torch speed of the TIG . At high scan speed reduced the glaze time therefore small melt depth occurs. The fine dendrites formed close to substrate surface in random direction because of fast solidifying of the melt pool. The glazing at high energy density the excess melting of base metal occurs and decreases the titanium-aluminum nitride particles in the coating zone. The microhardness achieved was maximum near the surface of the coating glazed with lower heat input [18]. Komvopoulo et al. (1990) reported that at the top surface of the coating fine microstructure was achieved because of high solidification rate in case GTA cladding as a result hardness and wear resistance of the substrate improved [20]. Sekhar et al. (2020) deposited the pure TiC composite coating on mild steel at different processing current. Authors noticed the major effect of the current on the hardness as well as wear loss value. It was reported that the maximum hardness value achieved about 3000 HV at 100 A and decreases with increases above 100 A processing current due to dilution of the mild steel with TiC coating layer occurs at high heat input. Due to high heat input (at 110 A and 120 A) melting depth increases due to dilution occurs. It was reported that the wear loss decreases with increasing processing current due to improvement of the bonding between TiC particles and steel substrate as shown in Fig. 4 [21].
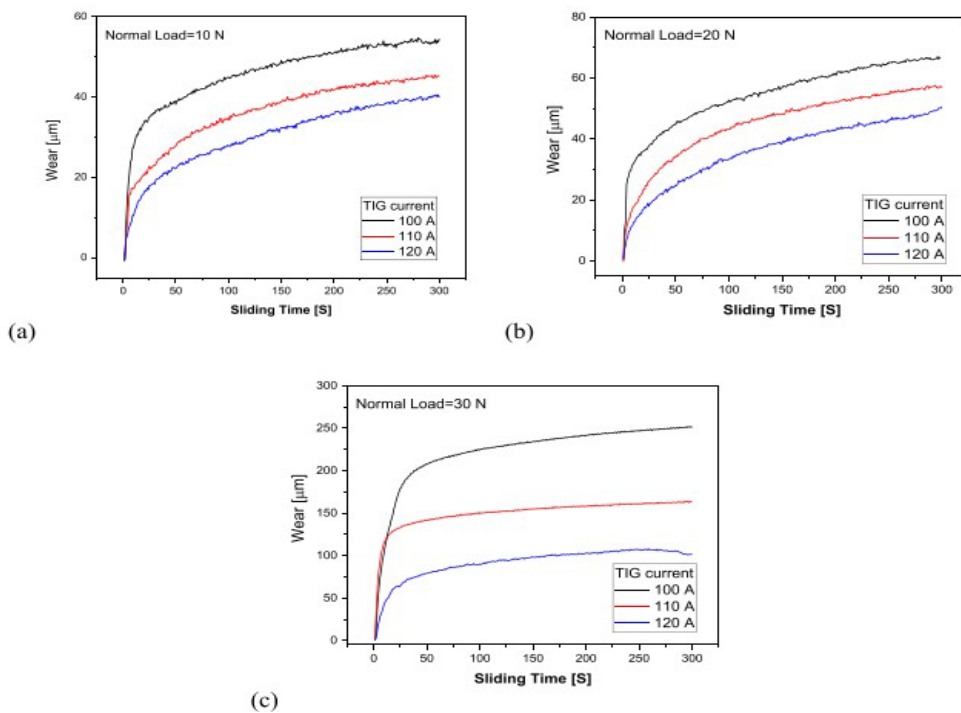

Fig. 4 Wear rate of the pure TiC coating layer with increasing input current at various applied load (a) 10 N, (b) 20 N and (c) 30 N [21]

Das et al. (2020) had improved the microhardness of AISI 1020 mild steel with Fe-based composite coating using TiC ceramic particles deposited by TIG cladding. It was reported that the microhardness value was maximum at 140 A, and decreases further with increase in input current [22].

Coating materials

The surface properties of the mild steel are enhanced by depositing the cladding layer using desirable coating materials by the GTA cladding techniques. The composite coating can be deposited by either directly mixing of ceramic materials such as TiN, TiB_2, SiC, TiC, WC etc. or hard phase produced in-situ techniques such as Ti + B_4C formed TiB, TiB_2 and TiC composite coating.

In recent years, the Ni-based coating possesses excellent advantages such as providing good bonding between coating materials and substrate, reducing friction coefficient, increasing wear and corrosion resistance. Among various ceramic reinforcements TiB_2 and TiN are considered as excellent ceramic materials because of its high melting points, excellent hardness and high thermal stability. Meng and Ji (2013) synthesized the TiN-TiB_2 ceramic phases in Ni-based coating layer on 16 Mn steel by in-situ process using arc cladding process. Researchers carefully analyzed the microstructure of the sample and noticed the TiB_2 (hexagonal and rectangular in shape) distributed in top surface of the coating, TiN (near spherical shape) distributed in middle zone and very less amount of TiN and carbide particles distributed in bottom zone. It was reported in the study that the microhardness gradually decreases with distance from the top surface of the coating and maximum microhardness found in the spam of 1100-1380 $HV_{0.2}$ [23].
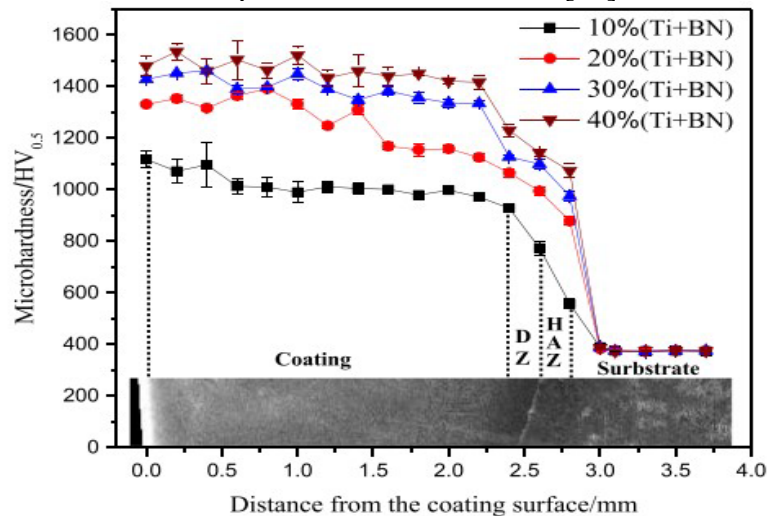
Fig. 5 Microhardness distribution of the composite coating with different composition of Ti+BN [24].

Meng et al. (2019) evaluated the wear and friction properties of Ni based composite coating using Ti and BN coating powder on a low carbon steel substrate. From XRD analysis of coated samples, it was noticed that the diffraction peak of TiB_2 and TiN increases with increasing the BN + Ti contents. Therefore microhardness of the composite coating enhanced with increasing of BN and Ti contents due to the increasing number of TiN and TiB_2 phases in coating zone. Researchers reported four regions: coated zone, dilution region, heat affected zone (HAZ) and substrate as show in Fig. 5. The microhardness achieved was in the range of 1100–1500 $HV_{0.5}$ in coating zone. The

wear loss of the composite initially decreases up to 30 % of Ti+BN and then increases with more than 30 % of Ti+BN contents [24].

Ceramic materials such as TiB_2, TiC, and Al_2O_3 and combination of these enhance the resistance to mechanical wear, hardness and chemical stability. Wang and Du (2010) improved the wear resistance and hardness of AISI 1020 steel by depositing the Fe based TiC-TiB_2-Al_2O_3 ceramic composite using GTAW process. The Al_2O_3 and Ti formed at 1025 °C because at this temperature exothermic reaction take place between Al and TiO_2 while TiC-TiB_2 formed at 1100 °C due to reaction take place between Ti and B_4C. The microhardness of the composite coating approaches about 1700 HV. From the wear test analysis, they reported that because of the formation of TiB_2-TiC-Al_2O_3 ceramic phases the quality of coating improved and enhance the plastic deformation resistance [25]. Sharifitabar et al. (2016) deposited the Fe–TiC–Al_2O_3 composite by GTA cladding on the AISI 1045 steel substrate using TiO_2–Al–C–Fe coating powder. It was reported in his that the coating with 0Fe approach minimum 430 HV while coating with 20Fe50C achieved maximum hardness value about 830 HV because of the TiC and Al_2O_3 particles detected after solidification in the coating layer. The researchers also tested the wear behaviour of samples with 20Fe50C and base metal using 5 N and 10 N normal load and reported that the wear resistance of the coated sample (20Fe50C) better than the base metal and did not affected by the change in normal load [10]. Weng et al. (2006) produced the Fe based TiC composite coating on the mild steel using graphite and ferrotitanium (FeTi) by GTA cladding. The microhardness test was also performed of the coated samples and maximum hardness value achieved was between 700–800 HV [26]. Tekera et al. (2014) have enhanced the wear resistance and hardness of AISI 1020 mild steel using different mixture of Hardox 450 steel and FeB powder. The microhardness value increases with boron content increases in mixture of composite powder. It was found that more B_8C and Fe_3B phases were present in the coating layer with 40 % FeB ($S_{2.4}$) therefore maximum hardness values measured as 655 HV for sample this samples. Wear resistance found excellent for the $S_{2.4}$ as compare to other samples [27]. Zhen-ting et al. (2008) synthesized in-situ TiC-TiB2/Fe based coating on steel substrate using argon arc cladding process. It was investigated and reported that the wear resistance and microhardness enhanced with increase the Ti+B_4C coating powders contents becuse the synthesis of the TiB_2 and TiC phases in the coated layer [28]. Xinhong et al.used the graphite, ferrotitanium and ferrovanadium powders to deposit the (Ti,V)C carbide Fe-based composite layer on low carbon steel. It was noticed that the wear resistance improved and maximum hardness found 950 $HV_{0.2}$ due to formation of multiple carbide particles in the coating such as TiC, VC and Fe_3C. It was reported that there were no evidence of brittle fracture and debris formation of carbide particles therefore the coated layer capable to resist the plastic deformation, micro plowing and micro cutting [29]. Wang et al. (2006) improved the microhardness and wear resistance by depositing the multi-layer on the AISI 1045 steel substrate using GTAW process. It was reported that TiC phases was synthesized by in-situ process using graphite and ferrotitanium powder. It was reported that the microhardness and wear resistance achieved higher value for multi pass coating layer than single pass coating layer [30].

Conclusion
From the above discussion, it may be concluded that hard composite coating may be deposited using GTA cladding, either in-situ process or ex-situ process. This new layer of composite coating can exhibit excellent microhardness, which can protect from the various surface degradations such as wear and oxidation.

- The shielding gas affects the quality of coating and surface properties of treated layer. Coating developed under argon shielding gas achieved good quality and high hardness as compared with coating developed under nitrogen shielding gas.
- In situ synthesis provides better quality and surface properties of the coating because it eliminates the interfacial incompatibility between the matrices and reinforcements.
- The microhardness decreases with distance from top surface to the substrate due to the different-density-driven force.
- The microhardness also depends upon the formation of ceramic phases in the coating zone. It increases with increasing the ceramic phases in the coating layer.
- During in-situ synthesis, at 1025 °C exothermic reaction take place between Ti and TiO_2 therefore the Al_2O_3 and Ti phases formed, whereas TiC-TiB_2 also formed due to reaction take place between Ti and B_4C at 1100 °C.
- The melt depth and coating width depends upon the heat input of GTA cladding. At high heat input, more melting of the base metal and decreases the amount of coating particles in the coating layer, therefore increases the coating dimension and decreases the microhardness values.

References

[1] M. Prince, A. J. Thanu, and P. Gopalakrishnan, Improvement in wear and corrosion resistance of AISI 1020 steel by high velocity oxy-fuel spray coating containing Ni-Cr-B-Si-Fe-C, High temperature materials and processes. 31 (2012) 149-155. https://doi.org/10.1515/htmp-2012-0009

[2] K.Y. Chiu, F.T. Cheng, H.C. Man, Laser cladding of austenitic stainless steel using NiTi strips for resisting cavitation erosion, Mater. Sci. Eng. A 402 (2005) 126–134. https://doi.org/10.1016/j.msea.2005.04.013

[3] M. Masanta, S. M. Shariff, and A. Roy Choudhury, A comparative study of the tribological performances of laser clad TiB2–TiC–Al2O3 composite coatings on AISI 1020 and AISI 304 substrates, Wear. 271 (2011) 1124-1133. https://doi.org/10.1016/j.wear.2011.05.009

[4] P. Gopalakrishnan, Some refinements to boriding processes, Ph. D thesis, Bharathiyar University, Coimbatore, India (1999).

[5] S. C. Mishra, , B. C. Mohanty, and B. B. Nayak, Arc plasma nitriding of low carbon steel, Surface and coatings technology. 145 (2001) 24-30. https://doi.org/10.1016/S0257-8972(01)01291-9

[6] R. Iakovou, L. Bourithis, and G. Papadimitriou, Synthesis of boride coatings on steel using plasma transferred arc (PTA) process and its wear performance, Wear, 252 (2002) 1007-1015. https://doi.org/10.1016/S0043-1648(02)00056-X

[7] Teker, Tanju, Selçuk Karataş, and S. Osman Yilmaz, Microstructure and wear properties of AISI 1020 steel surface modified by HARDOX 450 and FeB powder mixture, Protection of Metals and Physical Chemistry of Surfaces. 50(2014) 94-103. https://doi.org/10.1134/S2070205114010213

[8] Ivanov, F. Yu , S. V. Konovalov, V. E. Kormyshev, V. E. Gromov, A. D. Teresov, and O. A. Semina, Structure and properties of Hardox 450 steel with arc welded coatings, In AIP

Conference Proceedings. 1909, no. 1, p. 020073. AIP Publishing LLC, 2017. https://doi.org/10.1063/1.5013754

[9] Q. An, L.J. Huang, S. Jiang, X.T. Li, Y.N. Gao, Y. Liu, L. Geng, Microstructure evolution and mechanical properties of TIG cladded TiB reinforced composite coating on Ti- 6Al-4V alloy, Vacuum 145 (2017) 312–319. https://doi.org/10.1016/j.vacuum.2017.09.019

[10] M. Sharifitabar, J. Vahdati Khaki, and M. Haddad Sabzevar, Microstructure and wear resistance of in-situ TiC–Al2O3 particles reinforced Fe-based coatings produced by gas tungsten arc cladding, Surface and Coatings Technology. 285 (2016) 47-56. https://doi.org/10.1016/j.surfcoat.2015.11.019

[11] X.H. Wang, M. Zhang, B.S. Du, Fabrication in-situ TiB2–TiC–Al2O3 multiple ceramic particles reinforced Fe-based composite coatings by gas tungsten arc welding, Tribol. Lett. 41 (2011) 171–176. https://doi.org/10.1007/s11249-010-9701-6

[12] W.Q. Yan, L. Dai, C.B. Gui, In situ synthesis and hardness of TiC/Ti5Si3 composites on Ti–5Al–2.5Sn substrates by gas tungsten arc welding, Int. J. Miner. Metall. Mater. 20 (2013) 284–289. https://doi.org/10.1007/s12613-013-0725-4

[13] Agarwal, Arvind, and Narendra B. Dahotre, Comparative wear in titanium diboride coatings on steel using high energy density processes, Wear. 240 (2000) 144-151. https://doi.org/10.1016/S0043-1648(00)00357-4

[14] A. Zikin, E. Badisch, I. Hussainova, C. Tomastik, and H. Danninger, Characterisation of TiC–NiMo reinforced Ni-based hardfacing, Surface and Coatings Technology. 236 (2013) 36-44. https://doi.org/10.1016/j.surfcoat.2013.02.027

[15] Meng, Junsheng, and Zesheng Ji, Microstructure and technology research of in-situ synthesis TiN-TiB2/Ni composite coating by argon arc cladding, Physics Procedia. 50 (2013) 253-260. https://doi.org/10.1016/j.phpro.2013.11.040

[16] Hojjatzadeh, S. M. H., A. Halvaee, and M. Heydarzadeh Sohi, Surface alloying of AISI 1045 steel in a nitrogen environment using a gas tungsten arc process, Journal of Materials Processing Technology. 212 (2012) 2496-2504. https://doi.org/10.1016/j.jmatprotec.2012.06.006

[17] Huang, Her-Yueh, Effects of shielding gas composition and activating flux on GTAW weldments, Materials & Design. 30, (2009) 2404-2409. https://doi.org/10.1016/j.matdes.2008.10.024

[18] S. Dyuti, S. Mridha, and S. K. Shaha, Surface modification of mild steel using tungsten inert gas torch surface cladding, American Journal of Applied Sciences. 7 (2010) 815. https://doi.org/10.3844/ajassp.2010.815.822

[19] K. Easterling, Introduction to the Physical Metallurgy of Welding, Butterworth. (1992).

[20] K. Komvopoulo and K. Nagarathnam, J. Eng. Mater. Technol. 112 (1990) 131. https://doi.org/10.1115/1.2903299

[21] Sekhar, B. Raja, R. K. Nayak, S. R. Rout, and M. Masanta, Wear characteristic of TiC coated AISI 1020 mild steel fabricated by TIG cladding method, Materials Today: Proceedings. 26 (2020) 3288-3291. https://doi.org/10.1016/j.matpr.2020.02.466

[22] A. K. Das, S. Kumar, M. K. Chaubey, and W. Alam, Tungsten Inert Gas (TIG) Cladding of TiC-Fe Metal Matrix Composite Coating on AISI 1020 Steel Substrate, In Advanced Materials Research. 1159, (2020) 19-26. https://doi.org/10.4028/www.scientific.net/AMR.1159.19

[23] Meng, Junsheng, and J. Zesheng, Microstructure and technology research of in-situ synthesis TiN-TiB2/Ni composite coating by argon arc cladding, Physics Procedia. 50 (2013) 253-260. https://doi.org/10.1016/j.phpro.2013.11.040

[24] Meng, Junsheng, X. Shi, S. Zhang, M. Wang, F. Xue, B. Liu, W. Cui, and L. Bian, Friction and wear properties of TiN-TiB2-Ni based composite coatings by argon arc cladding technology, Surface and Coatings Technology. 374 (2019) 437-447. https://doi.org/10.1016/j.surfcoat.2019.06.015

[25] X. H. Wang, M. Zhang and B. Du, Fabrication In Situ TiB2–TiC–Al2O3 Multiple Ceramic Particles Reinforced Fe-Based Composite Coatings by Gas Tungsten Arc Welding, Tribology Letters. 41 (2011)171-176. https://doi.org/10.1007/s11249-010-9701-6

[26] X. H. Wang, S. L. Song, Z. D. Zou, S. Y. Qu, Fabricating TiC particles reinforced Fe-basedcomposite coatings produced by GTAW multi-layers melting process, Mater. Sci. Eng. A 441 (2006) 60–67. https://doi.org/10.1016/j.msea.2006.06.015

[27] Teker, Tanju, S. Karataş, and S. O. Yilmaz, Microstructure and wear properties of AISI 1020 steel surface modified by HARDOX 450 and FeB powder mixture, Protection of Metals and Physical Chemistry of Surfaces. 50 (2014) 94-103. https://doi.org/10.1134/S2070205114010213

[28] Z. T. Wang, , X. H. Zhou, and G. G. Zhao, Microstructure and formation mechanism of in-situ TiC-TiB2/Fe composite coating, Transactions of Nonferrous Metals Society of China. 18 (2008) 831-835. https://doi.org/10.1016/S1003-6326(08)60144-2

[29] W. Xinhong, L. Cheng, M. Zhang and Z Zou, Fabrication of multiple carbide particles reinforced Fe-based surface hardfacing layer produced by gas tungsten arc welding process, Surface and Coatings Technology. 203 (2009) 976-980. https://doi.org/10.1016/j.surfcoat.2008.09.020

[30] X. H. Wang, S. L. Song, Z. D. Zou, and S. Y. Qu, Fabricating TiC particles reinforced Fe-based composite coatings produced by GTAW multi-layers melting process, Materials Science and Engineering: A. 441, (2006) 60-67. https://doi.org/10.1016/j.msea.2006.06.015

Theoretical Investigation of Ballistic Electron Transport in Au and Ag Nanoribbons

Sushil Kumar[a] and R.K. Moudgi[b*]

Department of Physics, Kurukshetra University, Kurukshetra – 136 119, Haryana, India

[a]smutreja619@gmail.com, [b]rkmoudgil@kuk.ac.in

Abstract. We have systematically investigated the ballistic electron transport in gold and silver nanoribbons using first principle methods. The electronic structure calculation is carried out using the "density functional theory" (DFT) within the "SIESTA" code. While the electronic transport is studied using the "non-equilibrium Green's function" (NEGF) method combined with the "Landauer-Buttiker" (LB) approach. We have explored the transport along both the armchair (AC) and zigzag (ZZ) directions. Interestingly, both elements turn semiconducting in the AC-configuration, and their band gap oscillates with increasing width of the nanoribbon. On the other hand, nanoribbons retain metallic character in the ZZ-configuration, with a quantized electrical conductance $4G_0$ for sufficiently small width and temperatures as high as nearly 200 K; $G_0=2e^2/h$, is the elementary quanta of electrical conductance. At zero bias, electronic thermal conductance in each system increases non-linearly with temperature. More is the width of nanoribbons, more is the electronic contribution to heat transport. Further, to assess the utility of nanoribbons in thermoelectric devices, we have calculated the room-temperature Seebeck coefficient S. It is found to evince an oscillatory structure as a function of electrochemical potential μ of electrodes, with pronounced peaks (nearly -118 μV/K in the narrowest gold nanoribbon considered) in the AC-configuration. The maximum S achieved is seen to be comparable to the atomic chains of these elements in linear, ladder and zigzag topologies, suggesting practical importance of nanoribbons as thermoelectric sensors in nanoelectronic devices.

Introduction

One dimensional (1D) materials (viz. atomic chains, nanoribbons, nanorods, etc.) have emerged as an exciting field of research during last few decades. These materials have width and/or thickness in nanometer range and consequently, they show dramatically modified electronic structure due to pronounced quantum confinement effect along the nanoscale dimensions. Owing to this, 1D materials show interesting and unusual electronic properties like ballistic electron transport, quantized electrical conductance, quantum Hall effect etc. Graphene, a noble 2D material with zero band gap, has been cut into nanoribbons (NRs) which develop a gap in electronic structure [1,2], thus turning into a semi-conductor. Scattering from the edges and confinement effects are the main cause of transition into semi-conducting behaviour. Quite recently, Unsal et al. [3] have presented a systematic study of ballistic transport in NRs of $HfSe_2$, together with an analysis of their thermoelectric performance. As compared to their 2D counterpart, the phononic thermal conductance of NRs was found to be suppressed by a factor of 3. Also, the p-type values of thermoelectric figure of merit were improved a lot.

Very recently, Kapoor et al. [4] have simulated the zigzag (ZZ) NRs of noble metals elements (viz. Au, Ag, Cu), and their alloys and hetero-structures modeled in the honeycomb topology. They found pristine systems metallic in nature, while alloyed ones semi-conducting, with band gap decreasing on increasing width of the NRs. Among these systems, pristine Au is predicted to have

the highest tensile strength, which decreases with width of the NR. Singh et al. [5] have calculated the phononic thermal conductance of gold and silver NRs for different widths in both ZZ and armchair (AC) configurations. For nearly the same widths, the ZZNRs show relatively higher thermal conductance. With the exception of ACNRs of Au, all other systems show a linear fit of the room temperature thermal conductance with width of the NRs.

Along the lines of phononic transport, it would be relevant to look into the electron transport properties of gold and silver NRs. Hence, in this study, we have investigated these NRs in honeycomb structure (shown in Fig. 1) for electronic transport and thermoelectric properties using the "density functional theory" (DFT) together with the "Landauer-Buttiker" (LB) approach [6,7] in linear response regime. The effect of edges and width of the NRs on transport properties is also probed.
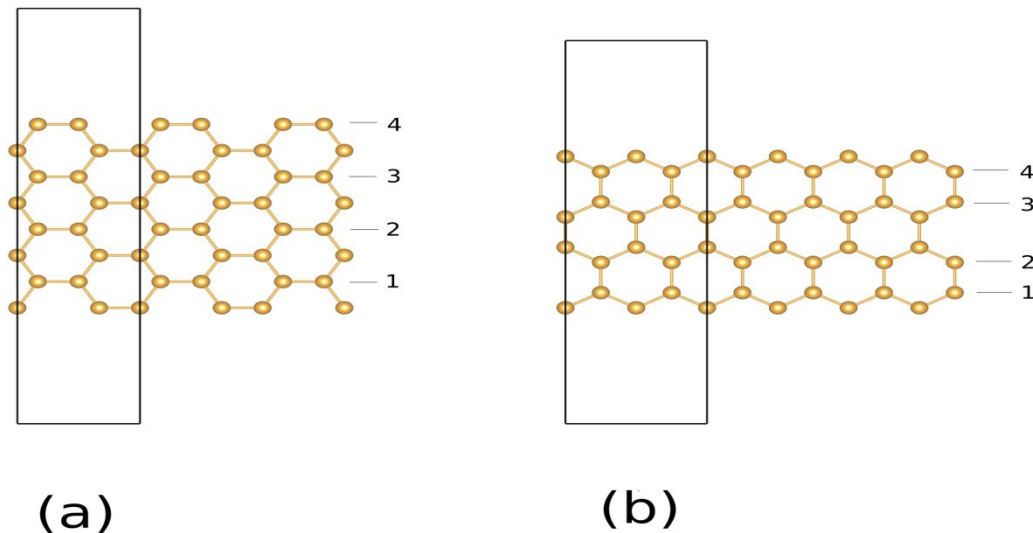

Figure 1: Ball stick depection of (a) Armchair, and (b) Zigzag gold nanoribbons with width index n=4. Rectangular box represents the unit cell chosen for the simulations.

Simulation and Modeling Details

Just like the graphene NRs, we have considered the honeycomb arrangement of atoms in the studied NRs. This leads to two different edges of the NR viz. the AC and ZZ. The width of the NR is indexed by the number of chains used to make it; for example, Fig. 1 shows the Au NRs of width index n=4 in both AC- and ZZ-configurations. The calculations for structure and electronic properties are done using the the SIESTA [8] code, a method based on DFT. Here, the norm-conserving pseudopotentials [9] based on the parameterization scheme of Troullier and Martins [10] are used, and the exchange and correlation (XC) potential is parameterized by the PBEsol-GGA functional [11]. We vary the width of NRs in the range 4-8. The periodic direction for NRs is taken to be the z-axis, while in x- and y-directions a vacuum of 20 Å is introduced. Real space integration is performed on a regular grid with a mesh cutoff of 500 Ry, while the first Brillouin zone is sampled by a uniform k-grid [12] of 1×1×30. All systems are optimized using the standard conjugate gradient (CG) technique until force on each atom becomes less than 0.04 eV/ Å. For calculating the electronic transmission function τ_{el} through the device, we have used the TBTrans utility of TranSIESTA [13,14] (a module of SIESTA) based on "non-equilibrium Green's function" (NEGF) approach [15]. We take a supercell consisting of three parts: (1) "left electrode"

(2) "right electrode", and (3) "scattering region" (i.e., device). Each of the three regions contain one unit cell, which is the same as the one used for SIESTA calculation (see Fig. 1). First, we calculate the electrode Hamiltonian, and then repeat it three times using the SISL [16] python package. This complete Hamiltonian is fed to the TBTrans utility to calculate τ_{el}.

Results and Discussion

First, we find the relaxed positions of atoms for the chosen unit cell. Cohesive energy for these systems is found to be negative, suggesting NRs to be stable structures. The relaxed structure is used to find the electronic transmission function $\tau_{el}(E)$, plotted in Fig. 2 for increasing width of the NRs. Since the calculation of electronic transport coefficients primarily involves $\tau_{el}(E)$ near the Fermi energy E_F, we have reported it for an energy window of -0.5 to 0.5 eV about E_F. It can be seen from Fig. 2 that the ACNRs contain finite gaps in $\tau_{el}(E)$ at E_F, while the gaps disappear in the ZZ-configuration, suggesting their semi-conducting and metallic nature, respectively.
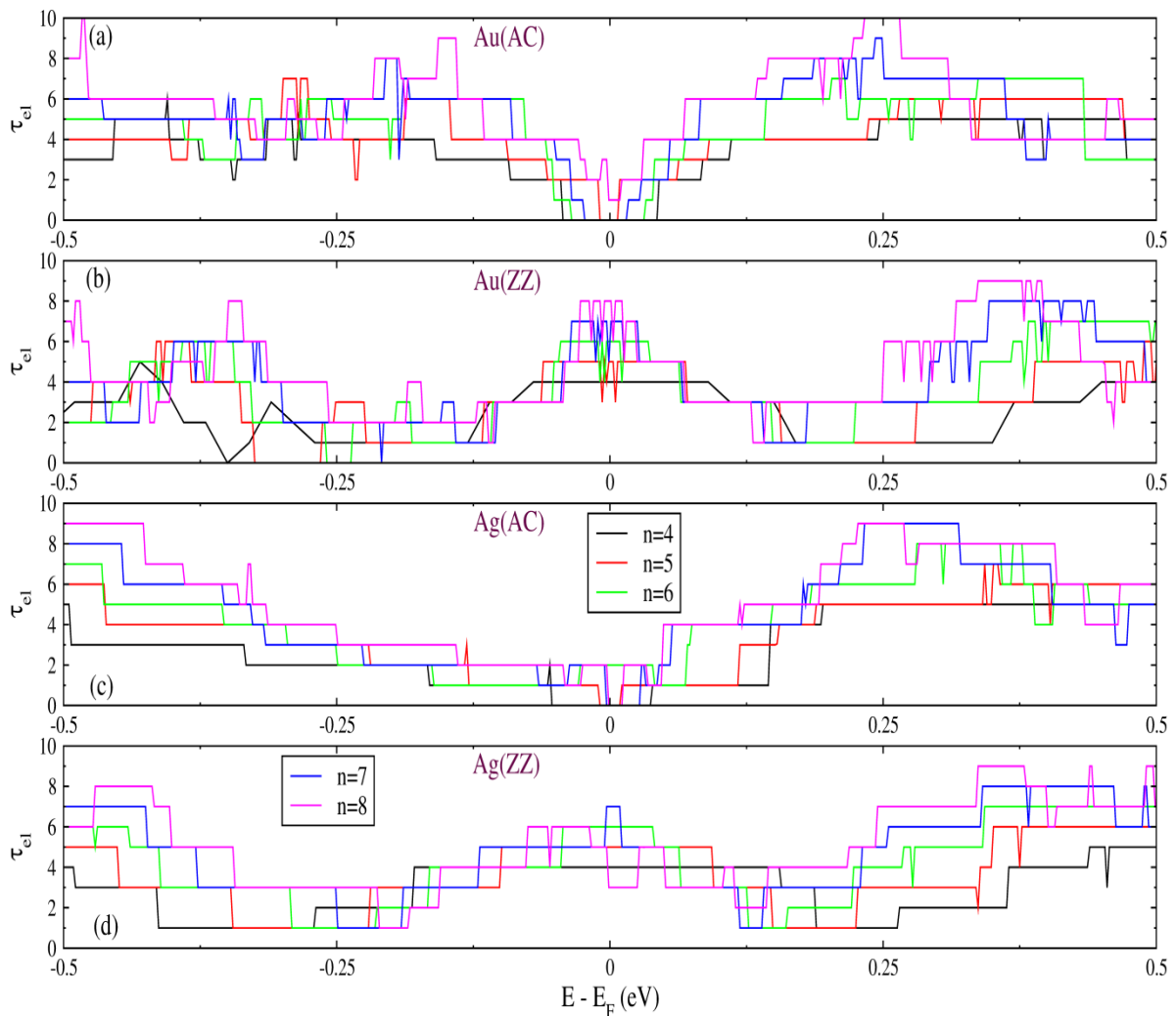

Figure 2: Calculated electronic transmission function $\tau_{el}(E)$ for (a) Au ACNRs, (b) Au ZZNRs, (c) Ag ACNRs, and (d) Ag ZZNRs systems for width index n in the range 4-8.

The calculated band gap values E_g of the ACNRs are summarized in Table. 1 below.

Table 1: Calculated electronic energy band gaps (in eV) in AC-configurations of NRs.

System	n=4	n=5	n=6	n=7	n=8
AuAC	0.089	0.017	0.067	0.041	-
AgAC	0.091	0.020	-	0.033	0.013

Interestingly, the systems with even width index show higher values of band gap. Also, like the atomic chains [17], the electron transport is ballistic in nature. One can obtain different transport coefficients using the LB approach by computing its main coefficient in the linear response domain as,

$$I_m(\mu, T) = \int_{-\infty}^{\infty} \tau_{el}(E)(E - \mu)^m \left(\frac{-\partial f(E, \mu, T)}{\partial E} \right) dE, \qquad (1)$$

where $f(E, \mu, T)$ is the "Fermi-Dirac" distribution function, and μ and T are the average electrochemical potential and temperature of the two electrodes, respectively. From Eq. 1, we can calculate the "electrical conductance" G, the "electronic thermal conductance" κ_{el}, and the "Seebeck coefficient" S using the following relations [17],

$$G(\mu, T) = \frac{2e^2}{h} I_0(\mu, T), \qquad (2)$$

$$\kappa_{el}(\mu, T) = \frac{2}{hT} \left[I_2(\mu, T) - \frac{I_1^2(\mu, T)}{I_0(\mu, T)} \right], \qquad (3)$$

and,

$$S(\mu, T) = \frac{-I_1(\mu, T)}{eT I_0(\mu, T)}. \qquad (4)$$

Here, h is the Planck's constant and e the electronic charge. Fig. 3 shows the calculated temperature dependence of G and κ_{el} under zero-bias condition, and the tuning of room-temperature S with electrochemical potential μ of electrodes for the considered NRs. In the systems having band gap, G starts to rise over its negligibly small value for T above a characteristic temperature E_g/k_B (typical of semi-conductors), while in metallic systems, G decreases with temperature, except for the presence of some dips (minima) or humps (maxima) (i.e., a non-monotonic dependence on T) in low temperature region. Such a non-monotonic variation in G with temperature has earlier been predicted by Singh et al. [18] for bimetallic atomic wires of noble metals. Interestingly, in Au ZZNR (n=4) and Ag ZZNRs (n=4, 5) systems, G displays a quantized behaviour up to temperatures as high as 200 K; it has values $4G_0$ and $5G_0$, respectively, for n=4 and n=5. $G_0=2e^2/h$, is the elementary quantum of electrical conductance. As can be seen from Fig. 2, this arises due to a flat and symmetric variation of $\tau_{el}(E)$ over a window of energy of order $k_B T$ about the Fermi level E_F. On the other hand, the electronic thermal conductance κ_{el} varies non-linearly with temperature, and its magnitude increases with increasing width of the NRs. Turning to the Seebeck coefficient S, its magnitude remains negligibly small under the zero-biasing condition even for the metallic NRs. Again, this result has its origin in the flat and symmetric behaviour of $\tau_{el}(E)$ over an energy interval of order $k_B T$ about E_F. However, S can be tuned to a great extent via biasing of electrodes. It is apparent from Fig. 3 that S oscillates with μ and even changes sign at characteristic μ. Particularly, the ACNRs show pronounced peaks for μ near either edge of gap in $\tau_{el}(E)$; for instance, S as high as -118.65 μV/K and -118.72 μV/K can be achieved at μ=0.035 eV and 0.03

eV, respectively, in the Au ACNR and Ag ACNR with n=4. As the ZZNR of Au with width n=5 develops a gap in $\tau_{el}(E)$ for μ around -0.3 eV, it also shows a significant S of 101.26 µV/K at μ= -0.32 eV. It is relevant to note here that the peak values of S in the smaller width (n=4, 5) NRs are comparable to those predicted for the atomic chains of these elements in linear, ladder and zigzag topologies [17]. Optimization of electronic thermal conductance together with its lattice counterpart, without a major change in S, can make the studied NRs useful in thermoelectric based coolers and generators. Moreover, the predicted decent values of S can be exploited for thermoelectric sensors applications.
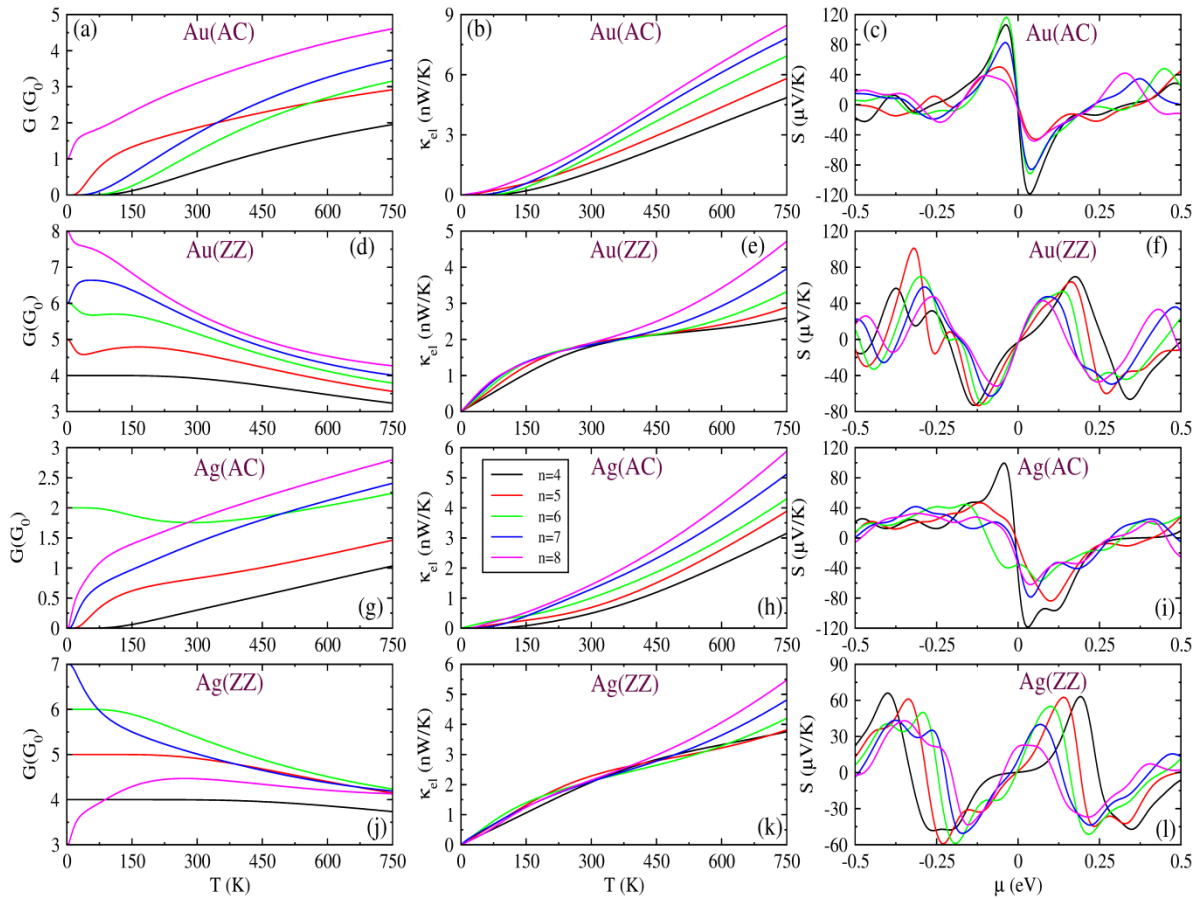

Figure 3: Variation of "electrical conductance" G, and "electronic thermal conductance" κ_{el} with temperature under zero-bias, along with the tuning of room temperature thermopower S with chemical potential μ for (a-c) Au ACNRs, (d-f) Au ZZNRs, (g-i) Ag ACNRs, and (j-l) Ag ZZNRs configurations.

Summary

To summarize, we have conducted the first-principles based simulations of ballistic electron transport in the NRs of gold and silver modeled in a topology similar to graphene NRs. For this, we have employed the NEGF approach and the "Landauer-Buttiker" formalism, with the requisite electronic structure obtained using the DFT based calculations performed with the SIESTA code. As a result of nanostructuring of monolayers along one of the lateral directions, the ACNRs become semiconducting, while the ZZNRs retain metallicity. For sufficiently small widths, the ZZNRs show a quantized electrical conductance up to temperatures as high as 200 K. Electronic heat transport exhibits a marked increase with increasing width of the NRs in AC-systems. But, in

ZZNRs, such a trend is missing for temperatures at least up to 300 K. The Seebeck coefficient S attains reasonably high values (above 100 μV/K in magnitude), when tuned via electrochemical potential μ of electrodes. Our study shows that the AC-configurations are a better candidate for thermoelectric applications.

Acknowledgements

References

[1] L. Yang, C.-H. Park, Y.-W. Son, M. L. Cohen, S. G. Louie, Quasiparticle energies and band gaps in graphene nanoribbons, Phys. Rev. Lett., 99 (2007) 186801.

[2] M. Y. Han, B. Özyilmaz, Y. Zhang, P. Kim, Energy band-gap engineering of graphene nanoribbons, Phys. Rev. Lett., 98, (2007) 206805. https://doi.org/10.1103/PhysRevLett.98.206805

[3] E. Unsal, R. Senger, H. Sevinçli, Enhancement of thermoelectric efficiency of T - $HfSe_2$ via nanostructuring, Physical Review B, 103 (2021) 014104. https://doi.org/10.1103/PhysRevB.103.014104

[4] P. Kapoor, A. Kumar, P. K. Ahluwalia, Size-dependent electronic, mechanical and optical properties of noble metal nanoribbons, Materials Science and Engineering B: Solid-State Materials for Advanced Technology, 262 (2020) 114786. https://doi.org/10.1016/j.mseb.2020.114786

[5] G. Singh, K. Kumar, R. K. Moudgil, Coherent phonon thermal transport in nanoribbons of gold and silver, in AIP conference proceedings, 2115 (2019) 030373. https://doi.org/10.1063/1.5113212

[6] M. Büttiker, Y. Imry, R. Landauer, S. Pinhas, Generalized many-channel conductance formula with application to small rings, Phys. Rev. B, 31 (1985) 6207–6215. https://doi.org/10.1103/PhysRevB.31.6207

[7] P. N. Butcher, Thermal and electrical transport formalism for electronic microstructures with many terminals, J. Phys. Condens. Matter, 2 (1990) 4869. https://doi.org/10.1088/0953-8984/2/22/008

[8] J. M. Soler, E. Artacho, J. D. Gale, A. García, J. Junquera, P. Ordejón, D. Sánchez-Portal, The SIESTA method for ab initio order-N materials simulation, Journal of Physics: Condensed Matter, 14 (2002) 2745. https://doi.org/10.1088/0953-8984/14/11/302

[9] D. R. Hamann, M. Schlüter, C. Chiang, Norm-conserving pseudopotentials, Phys. Rev. Lett., 43 (1979) 1494. https://doi.org/10.1103/PhysRevLett.43.1494

[10] N. Troullier, J. L. Martins, Efficient pseudopotentials for plane-wave calculations, Phys. Rev. B, 43 (1991) 1993. https://doi.org/10.1103/PhysRevB.43.1993

[11] J. P. Perdew, K. Burke, M. Ernzerhof, Generalized gradient approximation made simple, Phys. Rev. Lett., 77 (1996) 3865. https://doi.org/10.1103/PhysRevLett.77.3865

[12] J. Moreno, J. M. Soler, Optimal meshes for integrals in real- and reciprocal-space unit cells, Phys. Rev. B, 45 (1992) 13891. https://doi.org/10.1103/PhysRevB.45.13891

[13] M. Brandbyge, J.-L. Mozos, P. Ordejón, J. Taylor, K. Stokbro, Density-functional method for nonequilibrium electron transport, Phys. Rev. B, 65 (2002) 165401. https://doi.org/10.1103/PhysRevB.65.165401

[14] N. Papior, N. Lorente, T. Frederiksen, A. García, M. Brandbyge, Improvements on non-equilibrium and transport Green function techniques: The next-generation transiesta, Computer Physics Communications, 212 (2017) 8. https://doi.org/10.1016/j.cpc.2016.09.022

[15] S. Datta, Electronic Transport in Mesoscopic Systems, Cambridge university press, 1997.

[16] N. Papior, Sisl: v.0.10.0, 2020.

[17] G. Singh, K. Kumar, R. K. Moudgil, On topology-tuned thermoelectric properties of noble metal atomic wires, Physica E: Low-dimensional Systems and Nanostructures, 109 (2019) 114. https://doi.org/10.1016/j.physe.2019.01.007

[18] G. Singh, K. Kumar, R. K. Moudgil, Alloying-induced spin Seebeck effect and spin figure of merit in Pt-based bimetallic atomic wires of noble metals, Phys. Chem. Chem. Phys., 21 (2019) 20965. https://doi.org/10.1039/C9CP01671F

Structural, Electronic and Optical Properties of 2D Monolayer and Bilayer CoO₂

V.R. Patel[1,a*], A.R. Patel[1,b], Yogesh Sonvane[2,c] and P.B. Thakor[1,d]

[1]Department of Physics, Veer Narmad South Gujarat University, Surat, 395007, India
[2]Department of Applied Physics, S.V. National Institute of Technology, Surat 395007, India

[a]varsha0127@gmail.com, [b]arpatel14@hotmail.com, [c]yas@phy.svnit.ac.in, [d]pbthakor@rediffmail.com

Keywords: Monolayer, Bilayer, Electronic Properties, First-Principles Calculations, Optical Properties

Abstract. In present study, structural, electronic, and optical absorption properties of two dimensional (2D) monolayer and bilayer CoO_2 have been calculated by using the density functional theory. From the electronic band-structures of monolayer CoO_2 and bilayer CoO_2, these materials show metallic (conducting) behavior. The Optical absorption of monolayer and bilayer CoO_2 begins from the infrared region to visible region and maximum absorption in ultraviolet region of the electromagnetic spectrum. Results suggest that the monolayer and bilayer CoO_2 may be utilized for the optoelectronic applications and nano electronics.

Introduction

The discovery of graphene, gives completely new era of two dimensional materials[1]. Since the invention of the exotic properties of graphene, the two-dimensional layer materials like transition metal oxides (TMO), transition metal-dichalcogenides (TMDs), and other 2D materials have gained enormous research interest [2]. Cobalt oxide (CoO_2) is an end member of A_xCoO_2 (A = Li, Na), which is the auspicious material as cathode for fabrication of lithium ion batteries that was studied in previous investigation [3–9]. CoO_2 is an adaptable metal oxide material having many applications in various fields such as catalyst, electrochemical biosensor, photocatalyst and other applications [10]. First principles computations are used to study structural, electrical, and optical absorption properties of two-dimensional (2D) monolayer and bilayer CoO_2.

Computational Details

In the present work, all the calculations have been performed by the density functional theory (DFT). We have been used the generalized gradient approximation (GGA) as employed in QUANTUM ESPRESSO (QE) package with Perdew, Burke and Ernzerhof (PBE) pseudopotential [11,12]. For both the energy cut-off and the k-points, we have followed the convergence criteria. The structure was relaxed toward its equilibrium position, with the force on each atom being less than 10^{-5} Ry/Bohr. The energy cutoff for the wave functions was chosen as 80 Ry. The self-consistent calculations are performed with a Monkhorst-Pack of 15x15x1 k-mesh is used [13].To avoid physical interaction between the periodic layers, a vacuum of order 18 Å in z-direction was utilized. VESTA software was utilized for the visualization of the optimized structure [14].

Results and Discussion

Structural Properties

The optimized structures of monolayers and bilayer of CoO_2 are shown in Fig. 1. The two-dimensional hexagonal lattice, monolayer CoO_2 with the lattice parameters of a = 2.870 Å and, b = 2.870 Å and the bond-length for the bonds Co-O is 1.91 Å, which is consistent with previous reported work [4]. In bilayer CoO_2 with lattice parameters of a = 2.874 Å, and b = 2.874 Å (see Table 1) and, the bond-length for the bonds Co-O is 1.91 Å. The monolayer and bilayer CoO_2 have positive phonon frequencies which indicates that both are dynamically stable [15].
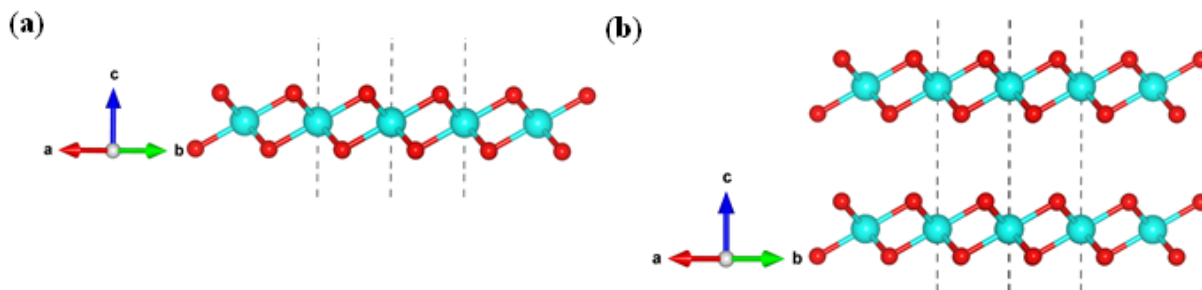

Fig. 1. The optimized structure of (a) Side view of monolayer CoO$_2$ (b) Side view of bilayer CoO$_2$.

Table 1. Calculated the lattice-parameters and bond-length of the monolayer and bilayer CoO$_2$

Structure	Lattice Constants		Bond length (Å)
	a (Å)	b (Å)	
Monolayer CoO$_2$	2.870	2.870	Co-O 1.91
Bilayer CoO$_2$	2.874	2.874	Co-O 1.91

Electronic properties

Fig. 2a and Fig. 2b shows the electronic band structures of the monolayer and bilayer CoO_2 along the k-path Γ– M – K – Γ. In monolayer and bilayer CoO_2 both exhibits metallic characteristics when both the bands cross the Fermi-level. In monolayer CoO_2 the position of the valance-band maximum, and the conduction-band minimum are found at Γ point. Projected density of states (PDOS) for monolayer, and bilayer CoO_2 are illustrated in Fig. 2c and Fig. 2d. The Co(d) orbital and O(p) orbital shows more contributions and less contributions of the O(d) orbital for the creation of the valance-band (VB) and the O(d) orbital gives less contributions for the creation of the conduction-band (CB) in monolayer CoO_2. The Co(d) orbital and the O(p) orbital shows more contributions and the O(d) orbital shows less contributions for the creation of the valance-band (VB) and the Co(d) orbital and the O(p) shows more contributions and the O(d) orbital shows less contributions for the creation of the conduction-band (CB) in bilayer CoO_2.The metallic behaviour of monolayer and bilayer CoO_2 is because of hybridization of the Co(d) orbital, and the O(p) orbital.
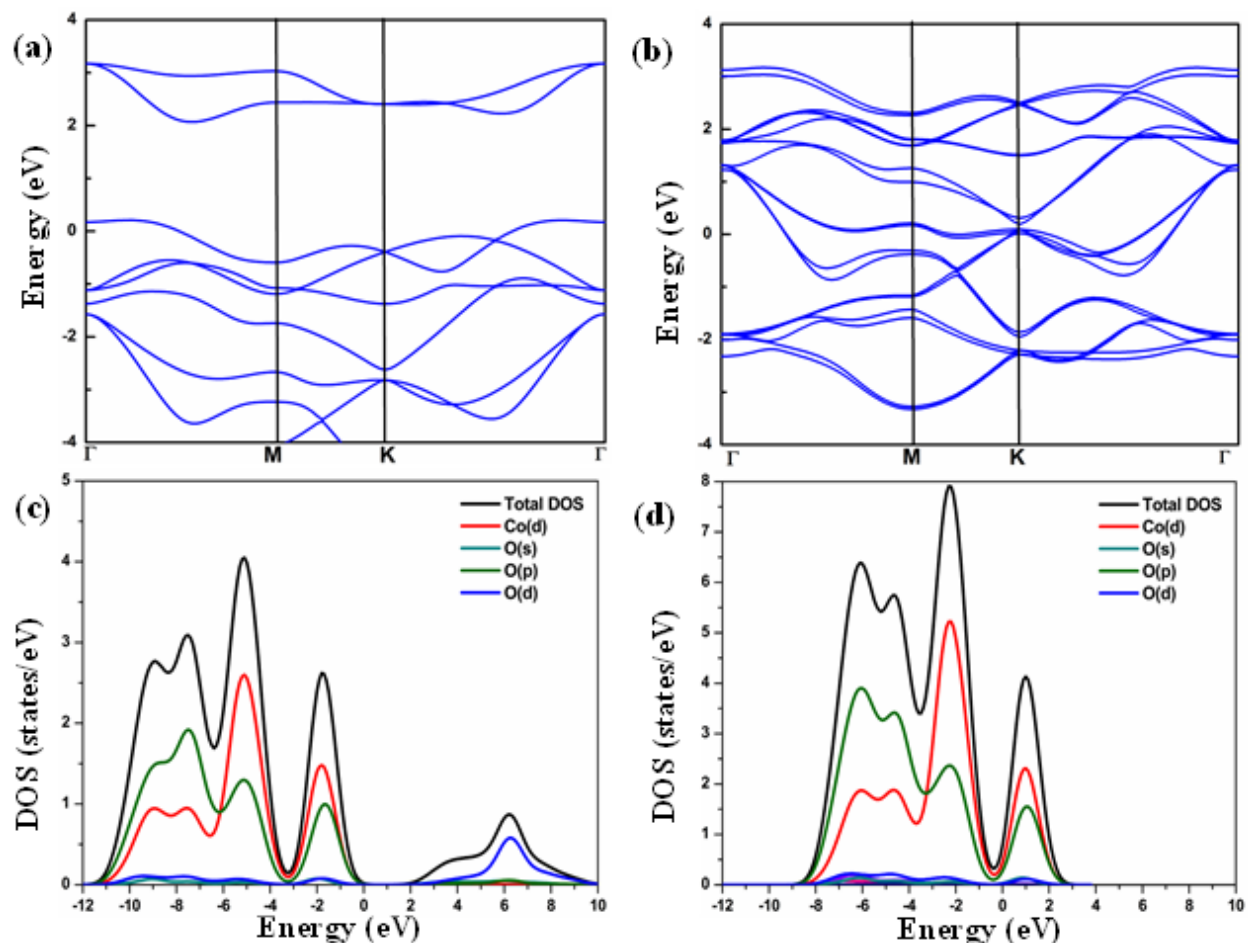
Fig. 2.(a) Band-structure of monolayer CoO₂ (b) Band-structure of bilayer CoO₂ (c) PDOS of monolayer CoO₂ (d) PDOS of bilayer CoO₂

Optical Properties

For study the optical properties of monolayer and bilayer CoO_2 we have calculated the absorption coefficients. Fig. 3 illustrates the optical absorption spectra of monolayer and bilayer CoO_2. The first absorptions peaks are observed in visible region for monolayer and bilayer CoO_2. Furthermore, the photon energies that correspond to the first absorption peaks located at 1.98 eV, and 1.92 eV for monolayer CoO_2, and bilayer CoO_2. The maximum absorption peak values are observed at 7.59 eV and, 7.53 eV, respectively, as shown in Fig. 3, which both are lies in the ultraviolet (UV) region for monolayer and bilayer CoO_2, respectively. The optical absorption of monolayer CoO_2 is slightly less than that of bilayer CoO_2. It is observed that optical absorption of monolayer and bilayer CoO_2 begins from the infrared (IR) region to visible region and shows maximum absorption in the ultraviolet regions of the electromagnetic spectrum. The results indicate that, optical absorption in visible region to ultraviolet region in monolayer CoO_2 and bilayer CoO_2 so that it can be used for optoelectronic applications.
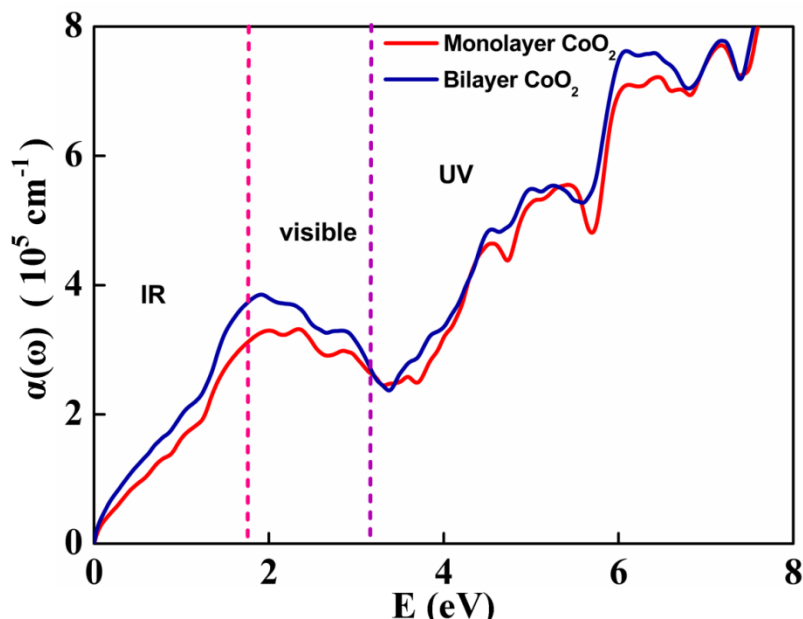
Fig. 3. Optical absorption spectra of monolayer and bilayer CoO_2

Conclusions

We have investigated structural, electronic, and optical absorption properties of two dimensional monolayer and bilayer CoO_2 in the present study. From the calculation of the electronic-band structures of monolayer, and bilayer CoO_2, these materials show metallic (conducting) behavior. The optical absorption spectra of the monolayer and bilayer CoO_2 have large absorption in visible region to ultraviolet region of electromagnetic spectrum. Results suggest that the monolayer and bilayer CoO_2 may be useful in the optoelectronic applications and nano electronics.

References

[1] M. Xu, T. Liang, M. Shi, H. Chen, Graphene-like two-dimensional materials, Chem. Rev. 113 (2013) 3766–3798. https://doi.org/10.1021/cr300263a

[2] C. Chowdhury, S. Karmakar, A. Datta, Monolayer Group IV-VI Monochalcogenides: Low-Dimensional Materials for Photocatalytic Water Splitting, J. Phys. Chem. C. 121 (2017) 7615–7624. https://doi.org/10.1021/acs.jpcc.6b12080

[3] G.G. Amatucci, J.M. Tarascon, L.C. Klein, CoO2, The End Member of the Li x CoO2 Solid Solution, J. Electrochem. Soc. 143 (1996) 1114–1123. https://doi.org/10.1149/1.1836594

[4] T. Motohashi, Y. Katsumata, T. Ono, R. Kanno, M. Karppinen, H. Yamauchi, Synthesis and Properties of CoO 2 , the x = 0 End Member of the Li x CoO 2 and Na x CoO 2 Systems. , Chem. Mater. 19 (2007) 5202–5202. https://doi.org/10.1021/cm702533v

[5] T. Motohashi, T. Ono, Y. Katsumata, R. Kanno, M. Karppinen, H. Yamauchi, Electrochemical synthesis and properties of CoO2, the x=0 phase of the AxCoO2 systems (A=Li,Na), J. Appl. Phys. 103 (2008). https://doi.org/10.1063/1.2828525

[6] M. Onoda, A. Sugawara, Stacking faults and metallic properties of triangular lattice CoO 2 with a three-layer structure, J. Phys. Condens. Matter. 20 (2008). https://doi.org/10.1088/0953-8984/20/17/175207

[7] K.W. Lee, W.E. Pickett, NaxCoO2 in the x→0 regime: Coupling of structure and correlation effects, Phys. Rev. B - Condens. Matter Mater. Phys. 72 (2005) 1–7. https://doi.org/10.1103/PhysRevB.72.115110

[8] E.B. Isaacs, C.A. Marianetti, Compositional phase stability of correlated electron materials within DFT+DMFT, Phys. Rev. B. 102 (2020) 1–11. https://doi.org/10.1103/PhysRevB.102.045146

[9] H. Kang, J. Lee, T. Rodgers, J.H. Shim, S. Lee, Electrical Conductivity of Delithiated Lithium Cobalt Oxides: Conductive Atomic Force Microscopy and Density Functional Theory Study, J. Phys. Chem. C. 123 (2019) 17703–17710. https://doi.org/10.1021/acs.jpcc.9b03232

[10] M. Ranjbar, Thermal decompose method for synthesis and characterization of CoO2/GrO nanostructures and optical investigation, J. Mater. Sci. Mater. Electron. 27 (2016) 11707–11712. https://doi.org/10.1007/s10854-016-5307-6

[11] P. Giannozzi, S. Baroni, N. Bonini, M. Calandra, R. Car, C. Cavazzoni, D. Ceresoli, G.L. Chiarotti, M. Cococcioni, I. Dabo, A. Dal Corso, S. De Gironcoli, S. Fabris, G. Fratesi, R. Gebauer, U. Gerstmann, C. Gougoussis, A. Kokalj, M. Lazzeri, L. Martin-Samos, N. Marzari, F. Mauri, R. Mazzarello, S. Paolini, A. Pasquarello, L. Paulatto, C. Sbraccia, S. Scandolo, G. Sclauzero, A.P. Seitsonen, A. Smogunov, P. Umari, R.M. Wentzcovitch, QUANTUM ESPRESSO: A modular and open-source software project for quantum simulations of materials, J. Phys. Condens. Matter. 21 (2009). https://doi.org/10.1088/0953-8984/21/39/395502

[12] J.P. Perdew, K. Burke, M. Ernzerhof, Generalized Gradient Approximation Made Simple, Phys. Rev. Lett. 77 (1996) 3865–3868. https://doi.org/10.1103/PhysRevLett.77.3865

[13] H.J. Monkhorst, J.D. Pack, Special points for Brillouin-zone integrations, Phys. Rev. B. 13 (1976) 5188–5192. https://doi.org/10.1103/PhysRevB.13.5188

[14] K. Momma, F. Izumi, VESTA 3 for three-dimensional visualization of crystal, volumetric and morphology data, J. Appl. Crystallogr. 44 (2011) 1272–1276. https://doi.org/10.1107/S0021889811038970

[15] D.L. Nguyen, C.R. Hsing, C.M. Wei, Theoretical prediction of superconductivity in monolayer CoO2, Nanoscale. 11 (2019) 17052–17057. https://doi.org/10.1039/C9NR03954F

Role of Plasma-Induced Liquid Chemistry for the Reduction Mechanism of Silver Ions to form Silver Nanostructures

Jenish Patel[1, a *] and Jiten P. Tailor[2,b]

[1]Department of Physics, Uka Tarsadia University, Bardoli-394350. India

[2]Department of Physics, S. V. National Institute of Technology, Surat, 395007, India

[a]jenishpatel87@gmail.com, [b]tailorjiten4u@gmail.com

Abstract. There exists a variety of reports on the synthesis of silver nanostructures by plasma-liquid interactions; however seldom are those that discusses the underlying reaction kinetics. The present study focuses in such direction where the role of plasma-induced chemistry has been analysed in detail with the reports on the influence of radicals on the formation of silver nanostructures. The silver nanostructures are synthesized from various precursor concentrations of silver and characterized byultraviolet-visible spectroscopy and transmission electron microscopy analysis. Further, experiments have been carried out to clarify the role of reductants in silver nanostructures synthesis. It is found that hydrogen peroxide is unable to reduce the silver ions to silver atoms which is a necessary step to produce silver nanostructures. The addition of organic solvents such as methanol and ethanol has been found to enhance the production rate of silver nanostructures which indicates that methanol and ethanol are strong electron donors affecting the reduction process of silver ions. In order to probe the exact reaction mechanism for silver nanostructures synthesis, iodine has been used as hydrogen radical scavenger along with silver precursor solutions; however, it has been observed that addition of iodine ions generates a favourable condition for the reduction of silver ions. The ultraviolet-visible spectroscopy results indicate the existence of small clusters of silver ions and silver iodide and further transmission electron microscopy characterization suggests that a well-dispersed silver nanoparticles of less than 30 nm in size have been formed. The lattice spacing calculation from transmission electron microscopy images suggests the presence of crystallinity of the particles. Overall, it is found that there are two possible ways for the reduction mechanism of silver nanostructures: either via hydrated electrons or hydrogen radicals or both.

Introduction

There exists a range of reports describing the synthesis of silver nanostructures (AgNSs) by means of plasma-based liquid process[1-5] due to their potential applications in various fields[6-9].AgNSs are generally synthesized in solutions containing Ag^+ ions where a reactive agents are used to form Ag atoms that nucleate and grow together in order to produce AgNSs. Depending on the nucleating seeds and the direction of the growth various sizes and shapes are AgNSs are synthesized. Often these chemical and physical methods require some reactive agents that are harmful and hazardous. The plasma-induced liquid chemistry (PiLC) is one of the ways that utilizes no such reactive agents for the synthesis process [10] and it can generate nanostructures (NSs) for ready-to-use purposes and applications.

One of the challenges faced in such PiLC studies is that the reactive species produced by plasma has a very complicated chemistry [11] and a multi-role to play in the synthesis process. Therefore,

the very basic need to such research area is to investigate the reaction mechanisms that clearly demonstrate the reduction process of ions to atoms with good experimental evidences. Peter Bruggeman and his colleagues presented a detailed review on such reaction analysis of plasma-liquid interactions. Although their focus was mostly on the reaction chemistry induced by plasma in liquids, but the analysis has helped various scientists in this field to correlate their experimental findings with the review and the observations made. The present study is such an attempt where AgNSs synthesized by PiLC are studied with a chemical analysis. We first discuss the synthesis process with the help of ultraviolet-visible (UV-Vis) spectroscopy and transmission electron microscopy (TEM) and then the impact of organic and iodine solutions on the reaction mechanisms are discussed in detail.
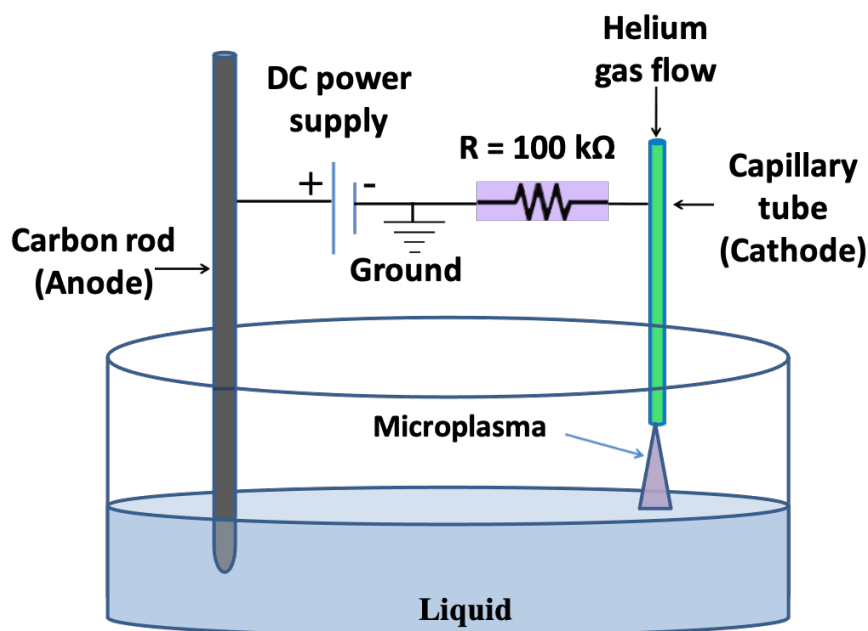
Experimental Details

Fig. 1. Plasma-induced liquid chemistry (PiLC) set-up.

The PiLC set-up used for the synthesis is as shown in Fig. 1 where carbon rod is in contact with the liquid serving as the anode and the cylindrical stainless steel capillary tube (with inner diameter of 0.25 mm) acts as the cathode through which a helium gas is allowed to flow at fixed rate of 70 cubic centimetre per minute. A high DC power supply is used to generate microplasma between the capillary outlet and the surface layer of the liquid. The distance between the capillary outlet and the surface layer of the liquid is 0.7 mm.

A solid powder of silver nitrate (AgNO$_3$) was obtained from Sigma Aldrich (UK) to prepare the aqueous solutions of different concentrations. Three different concentrations, 0.2 mM, 1 mM and 5 mM, were prepared by dissolving a proper amount of silver salt powder in distilled water. Each solution was treated by plasma at current of 2 mA for the period of 10 minutes. The synthesized samples were then characterized by UV-Vis spectroscopy and TEM analysis. In order to assess the reaction chemistry by plasma, experiments were performed with ethanol, methanol and iodine solutions obtained from Sigma Aldrich (UK).

Results and Discussion
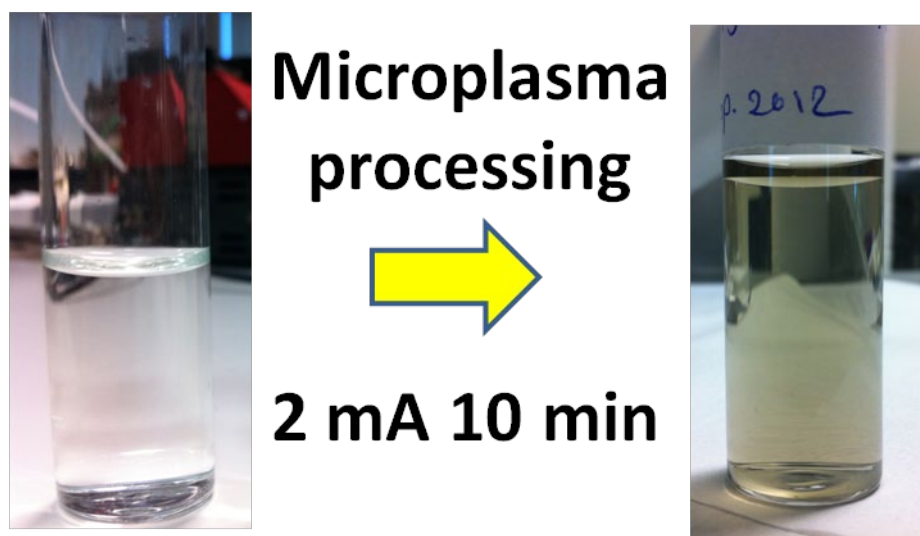
Synthesis of AgNSs

Fig. 2. Difference between the colour of 1 mM AgNO₃ solution before and after plasma treatment at current of 2 mA for the period of 10 minutes.

The AgNO$_3$ solution with a molar concentration of 1 mM is treated by plasma with discharge current of 2 mA. As the plasma treatment continues, there is change in the colour of the solution (see Fig. 2). The solution turns into dark green-yellow after 10 minutes of treatment, which is in good agreement with the characteristic surface plasmon resonance (SPR) peak of AgNSs[12,13].

Fig. 3 shows the obtained UV-Vis and TEM results of the synthesized AgNSs.The absorption peak at 387 nm (as shown in figure 3a) can be compared from the literature [14-17]. The TEM analysis reveals that plasma processing treatment leads to small size of the particles varying in the range of 10 nm to 30 nm along with few different size structures. However, literature shows that the absorption peak of silver nanowires can be found around 380-390 nm [18-20].Furthermore, a detailed study with another two different concentrations of silver precursors, 0.2 mM and 5 mM AgNO$_3$ are performed by plasma treatment procedure same as above.
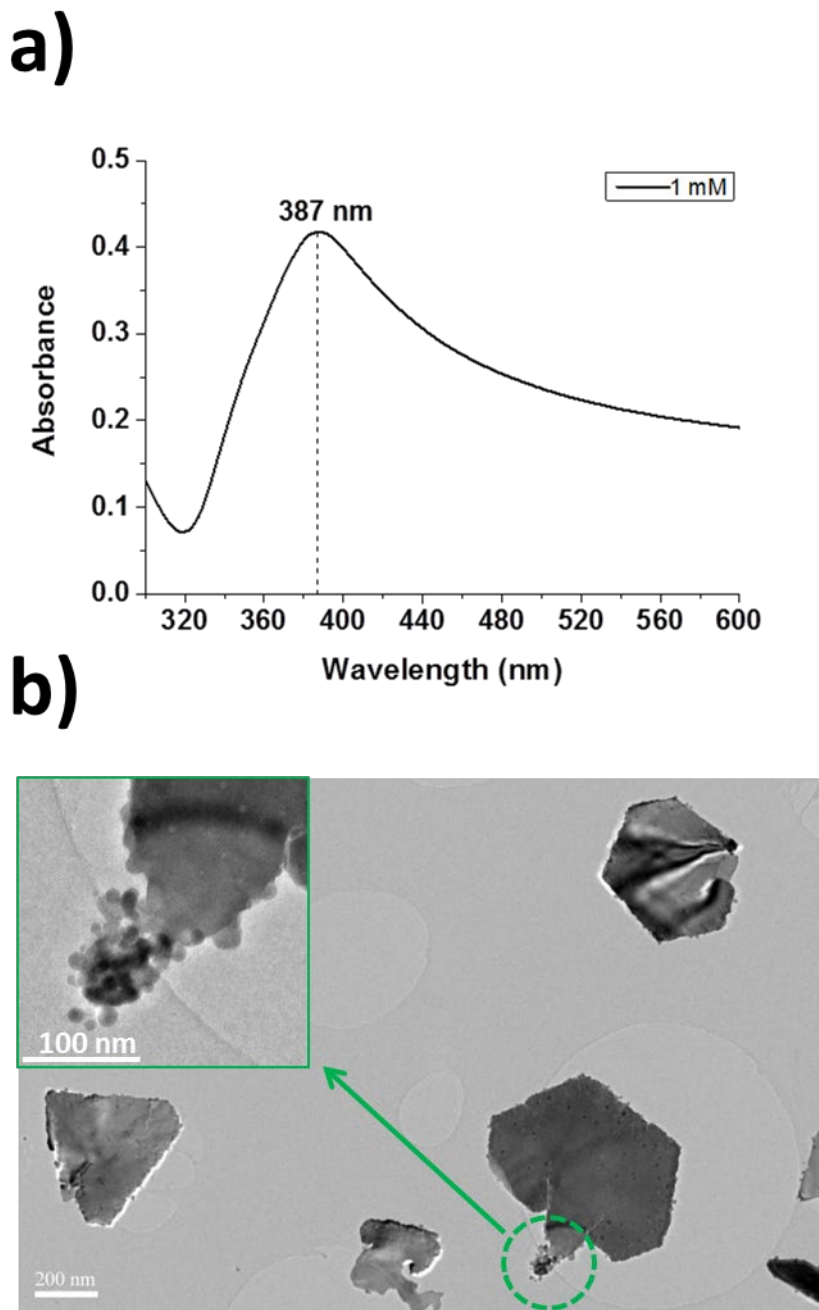
Fig. 3.*Plasma treatment of 1 mM AgNO₃ solutions produces silver nanostructures(a) UV-Vis spectra and (b) transmission electron microscopy (TEM) image.*

Fig. 4a shows a comparative image of the silver nanostructure colloids with different concentrations. Fig. 4b shows a comparative graph of UV-Vis. spectroscopy, which indicates that 5 mM $AgNO_3$has a peak shifted from 387 nm to 402 nm while 0.2 mM $AgNO_3$ did not exhibit sharp peak but has a broad absorption band observed around 360 nm. The broadening of the peak for 5mM $AgNO_3$ is much stronger than 1mM $AgNO_3$ precursors, which indicates that the full width at half maximum (FWHM) for 1mM $AgNO_3$(103 nm) is less compared to 5 mM

precursors(149 nm). It can also be observed that the intensity of absorption for 0.2 mM is quite lower as compared to 0.1 mM and 5 mM samples. On the other hand, intensity of absorption for 5mM precursors is less compared to 1 mM because of variation in size and change in the morphology in case of 5mM sample.

(a)

(b)

Fig. 4. *(a) Photographs of AgNSs samples prepared from different concentrations 0.2 mM, 1 mM and 5 mM. (b) Comparison of UV-Vis absorption spectra of the samples obtained from 0.2 mM, 1 mM and 5 mM AgNO₃ concentrations (Note that 0.2 mM sample has the intensity of the absorption that is multiplied here by a factor of 3 for clarity)*

In order to assess the effect of silver precursor concentration on the optical and morphological properties of the synthesized silver nanostructures, another two different concentrations of silver precursors namely 0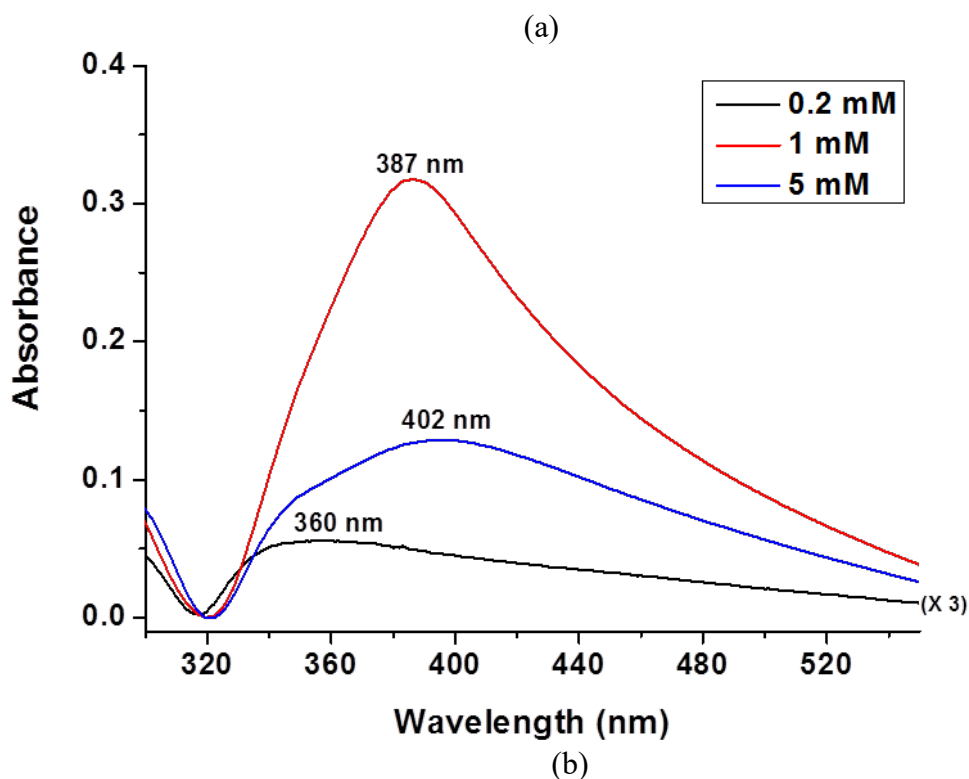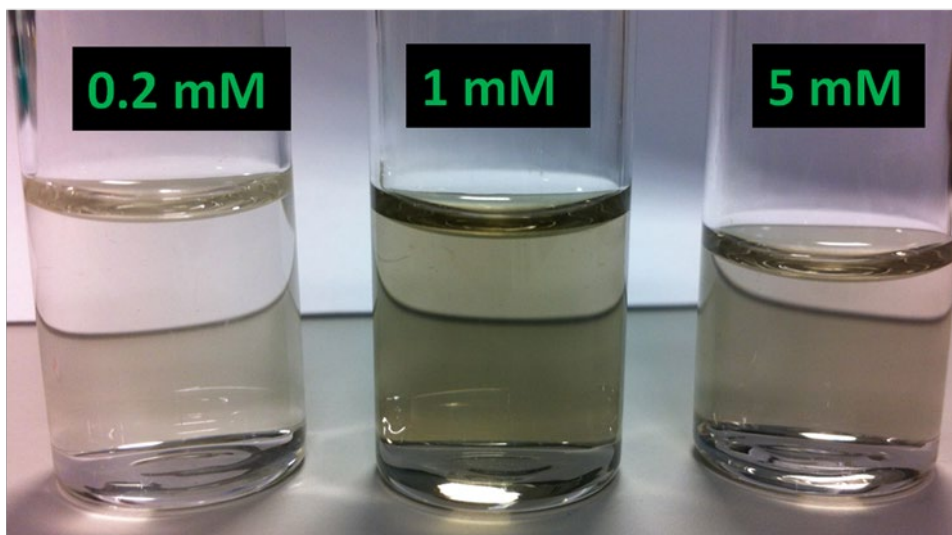.2 mM and 5 mM AgNO₃are processed by plasma with same plasma processing conditions as above and characterized by UV-Vis and TEM (see Fig. 4). Fig. 4a compares the photographs of the AgNSs of different concentration 0.2 mM, 1 mM and 5 mM.UV-Vis results demonstrates that increasing the AgNO₃ concentration to 5 mM shifts the absorption peakfrom 387 nm to 402 nm (see Fig. 4b). However, the 0.2 mM AgNO₃ concentration does not exhibit any sharp absorption peak, but instead a broad absorption band around 360 nm can be observed.It can also be noted that broadening of the absorption peakfor the sample with 5 mM is much stronger than the sample with 1 mM;i.e. the full width at half maximum (FWHM) for 1 mM (103 nm) is less than that for 5 mM (149 nm). The reduction in the intensity of absorption for the 0.2 mM sample is quite apparent because of the lower AgNO₃ concentration used. On the other hand,the intensity of absorption for 5 mM is less than that of 1 mM and the reason could be the existence of different morphological structures orsmaller particles in 5 mM.
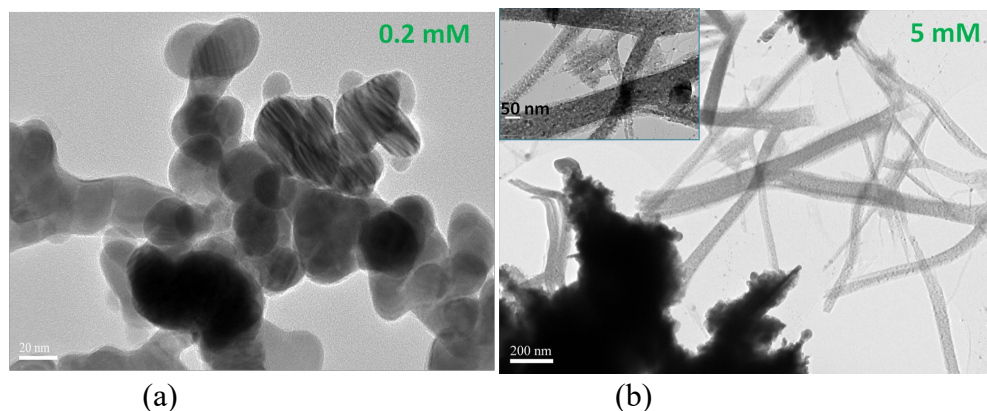
Fig. 5.*TEM images of the synthesized AgNSs with (a) 0.2 mM and (b) 5 mM AgNO₃concentrations.*

Fig. 5 shows TEM analysis of 0.2 mM and 5 mM concentration of silver precursors. It can be observed that 0.2 mM silver precursors produces nanoparticles having size varied from 20 nm to 30 nm with nearly spherical shape. Fig. 5a also shows agglomerated nanoparticles which means nanoparticles stick together duringthe growth of the silver nanostructures. These results indicate the absence of the stabilizer indicating they are not electrostatically stabilized. The nanostructures are also non-uniform in size and shape which is also well reported in Huang *et al.* article [21]. As shown in figure 5b, 5mM silver precursors exhibits some nanowires having diameter varied from 50-70 nm. The inset image of Fig. 5b reveals interesting features in case of 5 mM silver nanostructures. It shows small nanoparticles are attached to the surface of the nanowires which may be due to the coulomb attractive force.

Analysis of reaction mechanisms for the synthesis of AgNSs

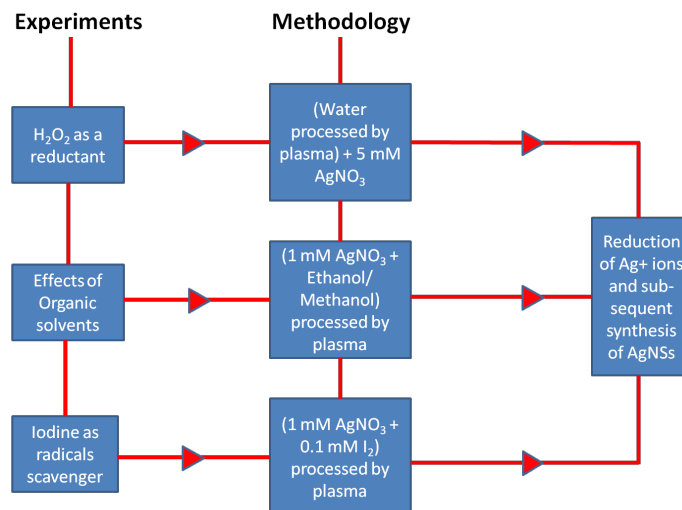***Fig. 6.****Diagrammatic view of the experiments and corresponding strategiesutilised to understand silver nanostructures (AgNSs) synthesis mechanism. Experiments are performed to clarify the better look in the possible role of H_2O_2 as a reducing agent, on the impact of organic solvents and on the probability of using iodine (I_2) as a radical scavenger.*

The synthesis of silver nanostructures by plasma-liquid interactions has been reported previously by a number of researchers; however a small fraction of them discusses the preparation without any surfactant and their respective liquid-chemistry. [4, 21-33]. In this part of discussion, we propose different mechanisms leading to the reduced form of silver ions. In the present work, silver nanostructures are formed with no help from any additional surfactants. The plasma-liquid interface shows up the change in the colour of the solution and hence the much needed liquid-chemistry for the synthesis should occur at the plasma-liquid interface that is responsible for the conversion of Ag^+ cations to Ag^0 atoms. The reduced Ag^0 atoms then nucleate and grow together to produce AgNSs. A set of experimental strategies is designed to clarify the role of reduction mechanism for AgNSs formation. Fig. 6 indicates the diagrammatic view of the experiments conducted to probe the reaction chemistry involved.The experiments are conducted to clarify the proper insights in the probable reductive role of hydrogen peroxide, in the impact of ethanol and methanol solutions, and on the probability of employing iodine (I_2) as a radical scavenger.

H_2O_2 as a possible reducing agent
There are different possible pathways for the reduction mechanism of silver nanostructures, for instance through hydrogen radicals ($H^•$)inside the liquid[25, 27, 34-36],aqueous (hydrated) electrons (e^-_{aq}) [33,34,37,38] and hydrogen peroxide (H_2O_2) [25]. It has been observed previously that the silver nanoparticles actually decompose the hydrogen peroxide[39] and that is why the two reactions, i.e. silver nanoparticles decomposing the hydrogen peroxide and the reduction of Ag^+ cations by hydrogen peroxide, are competing with each other. Therefore, this contradiction state that hydrogen peroxide reducing the Ag^+cations cannot be expected. So, to clarify the role of hydrogen peroxide, the experiment is carried with plasma processed water. It has been found that distilled water treatment by plasma generates the hydrogen peroxide which does not decomposes in water for at least four hours[11]. When the plasma processed water at 2 mA is added to silver

nitrate solution, it is found that the colour of the solution does not change. The results are shown in Fig. 7 where the absorption spectrum of the plasma processed water added with silver nitrate is compared with that of the plasma processed silver nitrate solution (i.e. 5 mM AgNSs). There is no clear evident surface plasmon resonance peak as compared to the 5 mM AgNSs sample which sufficiently demonstrates inability of hydrogen peroxide to reduce Ag^+ cations.
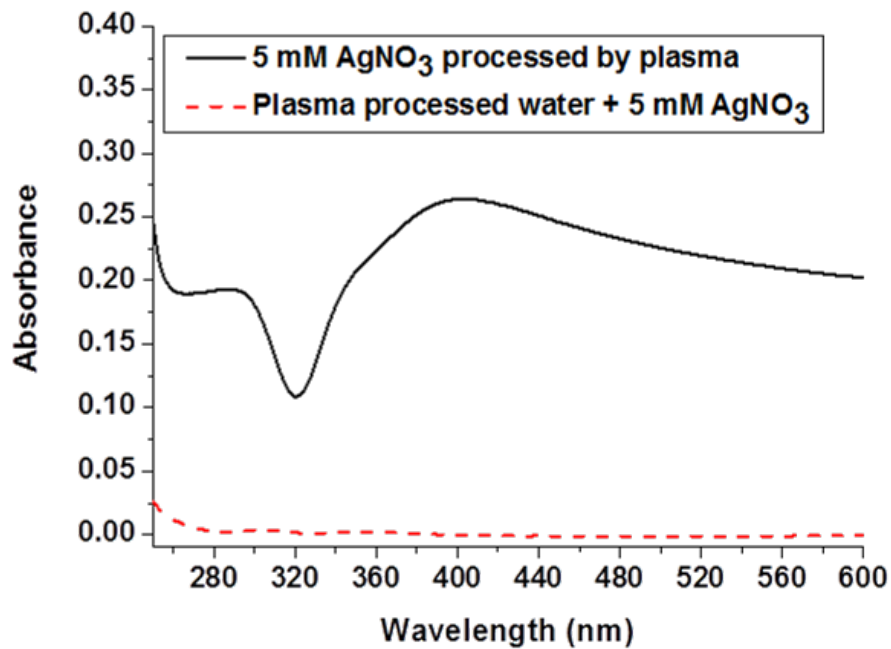

Fig. 7. *Absorption spectra of plasma treated water sample mixed with 5 mM AgNO₃ (red line) and absorption results 5 mM AgNO₃ solution treated by plasma are also shown for comparison (black line).*

Influence of ethanol and methanol solvents

The literature review suggests that the presence of the organic solutions influences the reductive scheme of Ag^+ cations to synthesize silver nanoparticles. For instance, the reports on the synthesis of AgNSs by photochemical techniques and pulse radiolysis methods indicate that the proper ratio of ethanol and silver precursor solutions helps to affect the reduction rate of Ag^+ to form Ag^0 atoms[24,40,41]. In other words, the ethanol added in the silver precursor act as a reducing agent. In order to scavenge the hydroxyl radicals and hydrated electrons one can also utilize tert-butyl alcohol or methanol or 2-propanol in order to achieve the reductive situations [40-42].For instance, Kamat et al. have clearly reported that the presence of tert-butyl alcohol to the silver precursor solutions would help to achieve the scavenging of hydroxyl radicals and therefore the remaining reactive radicals (i.e. hydrated electrons) would act as reductants for Ag^+ cations [42]. In this section, we present the results of the addition of ethanol and methanol in silver nitrate solutions for plasma processing. 1 mL of ethanol and 1 mL of methanol is mixed with 10 mL of silver nitrate solution of treated by plasma at current of 2 mA individually one by one and the absorption results are shown in Fig. 8. The Fig. 8 also includes in the absorption results gained by direct electrochemistry; the two electrodes carbon rod and the capillary tube both are immersed in the liquid and the current of 2 mA is applied.
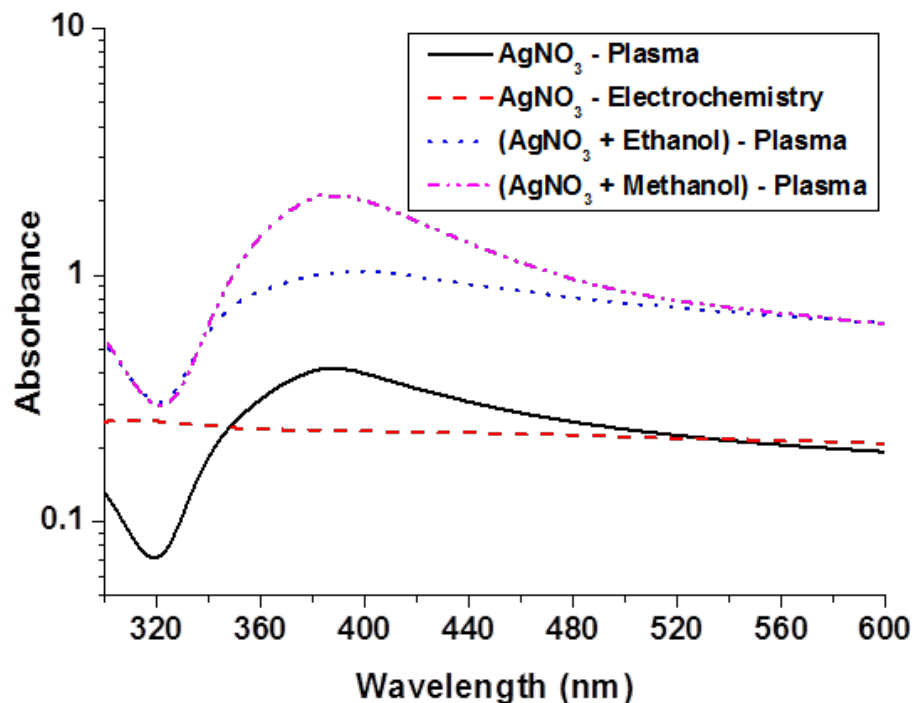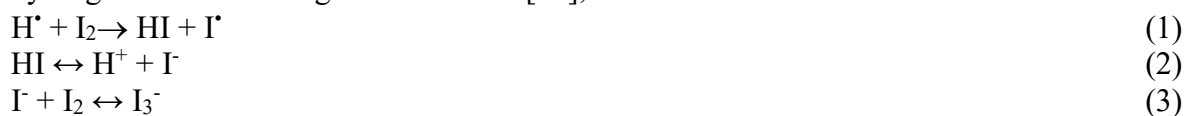
Fig. 8. *Absorption spectrum of 1 mM AgNO₃ solutions treated by plasma and direct electrochemistry. The impact of ethanol and methanol on the synthesis of AgNSs is shown in graph. The ethanol and methanol are mixed with 1 mM AgNO₃ solutions and treated by plasma. In all the cases, the plasma is operated at current of 2 mA for the period of 10 minutes.*

The results as shown in Fig. 8 suggest that silver nanostructures are not formed by direct electrochemistry indicating that a different reaction mechanism is at play that must be induced by plasma-activated chemistry. The experiments with the ethanol and methanol clearly enhances the intensity peak of the synthesized silver nanostructures which is in well agreement with previously reported articles [24]. Therefore, the experiments conducted with organic solvents reflect that methanol and ethanol have a strong capacity to act as a donor of electrons. In other words the negative redox potentials of both the organic solvents appear to be high and therefore it affects the reduction of silver cations[43].

Iodine as a radical scavenger

As per the literature survey[1,4,21,32,34,41] and also the experimental findings received in this work so far, we have two probabilities for the reduction of Ag^+ cations: either it may get reduced via hydrogen radicals or via hydrated electrons (or both). In a similar plasma-based system but with slightly different configuration, it has been found that AgNSs could not be formed where plasma was generated at the anode part [44]. Hence, the reduction of Ag^+ cations may take place through electrons [45]. In this section we describe the results of experiments conducted with iodine solutions along with the silver precursor concentrations. The iodine molecules interact with the hydrogen radicals through the reactions [46],
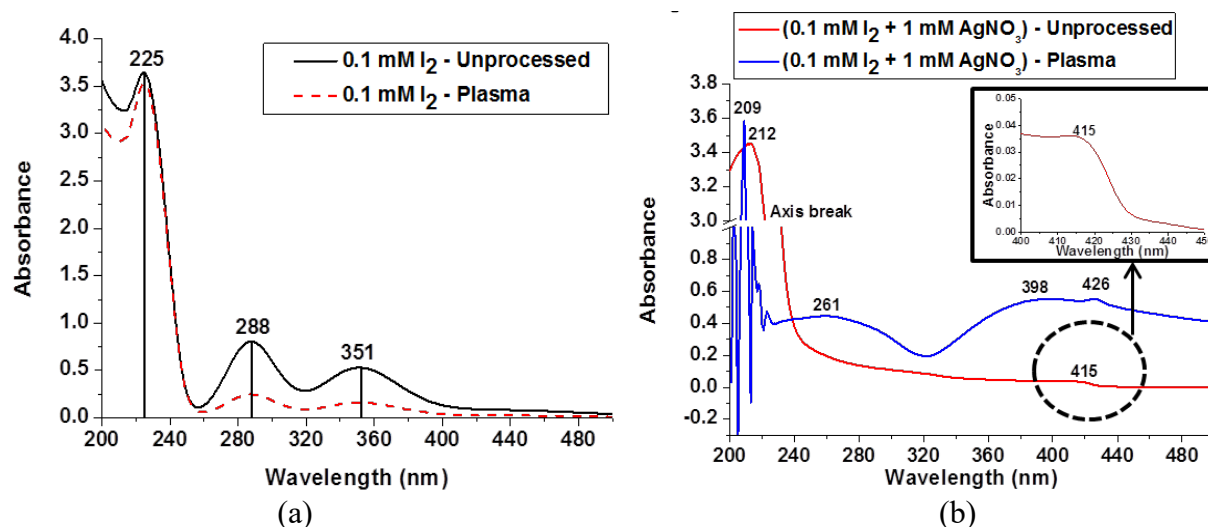
$$H^{\bullet} + I_2 \rightarrow HI + I^{\bullet} \tag{1}$$

$$HI \leftrightarrow H^+ + I^- \tag{2}$$

$$I^- + I_2 \leftrightarrow I_3^- \tag{3}$$

Fig. 9. *(a) The UV-Visspectrum measurements of unprocessed and plasma treated 0.1 mM I_2 solution. (b) The UV-Visspectrum measurements of plasma treatment of 0.1 mM I_2 solution mixed with 1 mM $AgNO_3$ solutions. The graph compares the absorption peaks before and after plasma treatment. In all the cases, the plasma is operated at current of 2 mA for the period of 10 minutes.*

The purpose of using the iodine is to scavenge the $H^•$ radicals generated by plasma-water reactions and therefore they would not be able to reducethe Ag^+cations which leaves only the hydrated electrons as a pathway to the silver reduction. In order to observe the effects of plasma treatment on the iodine solution, 0.1 mM I_2 solution is processed by plasma at current of 2 mA and the absorption measurement is compared with the same obtained from the unprocessed I_2 solution. As shown in Fig. 9, there three different absorption peaks exhibited by the unprocessed I_2 solution: 225 nm is relevant to the solvated I^- ions[46-48] and other two peaks at 288 nm and 351 nm are associated with the I_3^- ion [46,48].It is also important to note the reaction of iodine with water molecules via reaction [49,50]

$$I_2 + H_2O \leftrightarrow OI^- + I^- + 2H^+. \tag{4}$$

It can be observed from Fig. 9a the plasma treatment of I_2 solution reduces the intensity corresponding to the presence of I_3^- ions to 30% and the presence of I^- ions reduces to 92% of their initial unprocessed values. So, it can be concluded that the forward rate of the reaction (3) is reduced. The plasma processing of water generates a huge amount of H^+ ions that can react with I^- ions and hence the presence of 225 nm peak corresponding to I^- ions in plasma processed I_2 solution confirms. As indicated by the red dotted graph in Fig. 9a, the plasma processing does not scavenge the I^- ions. The aqueous 0.1 mM iodine solution is mixed with the 1 mM silver nitrate with a volume ratio of 1:10 and plasma treatment at current of 2 mA is performed. The results of absorption spectrum are shown in Fig. 9b. A new abosorption band with a center-peak at 415 nm appears which correspond to silver iodide (AgI) [51-53] appearing due to the reaction with [54]
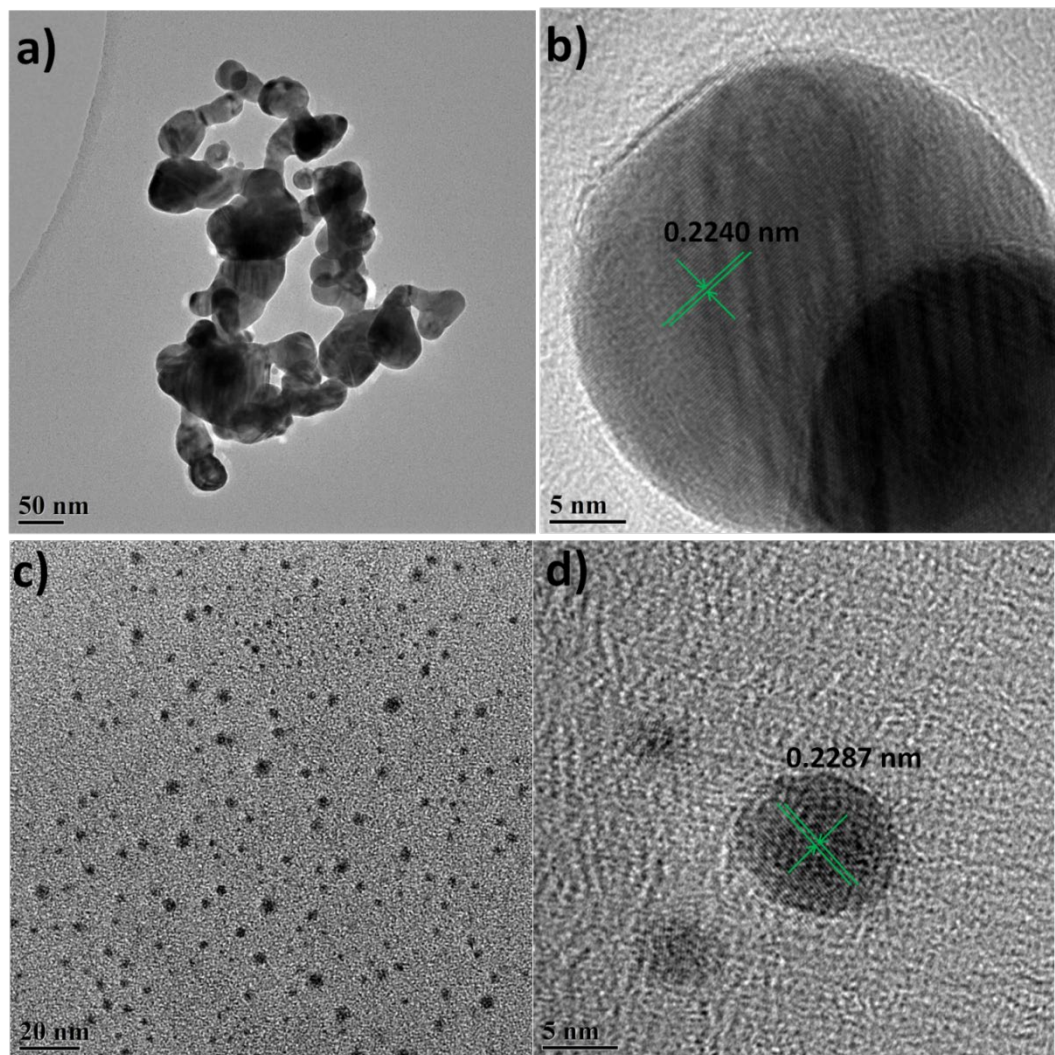
$$6AgNO_3 + 3I_2 \rightarrow 4AgI + 2AgIO_3 + 6NO_2 \tag{5}$$

Fig. 10. *(a)-(b) TEM images of AgNSs of 25 nm to 30 nm in size and (c)-(d) TEM images of the AgNSs of 2 nm to 5 nm in size. The AgNSs samples are prepared from plasma treatment of 0.1 mM I_2 solution mixed with 1 mM $AgNO_3$ solutions at current of 2 mA for the period of 10 minutes.*

Due to the presence of the silver ions, the absorption peaks at 351 nm, 288 nm and 225 nm are not observed here and a peak at 212 nm is found that corresponds to highly dispersed Ag^+ ions [51,55,56]. We also observe the presence of absorption region centered at 415 nm corresponding to silver iodide [51,57,58]. There also exists a characteristic SPR peak at 398 nm indicating the presence of AgNSs. However, the intensity of absorption is enhanced and the peak is having a red-shift of 11 nm as compared to the results of AgNSs obtained from 1 mM silver precursor solutions (refer to Fig. 2a). The absorption maximum at 415 nm is still there after plasma processing, however it has a red-shift of 11 nm. This means that there is still the presence of silver iodide. The peak at 261 nm correspond to the presence of silver ion clusters $Ag_m^{\delta+}$[34,38,42,59,60]; where δ = different ionic states of Ag^+ions and m = number of Ag atoms. The existence of nanostructures is also confirmed by the TEM images (see Fig. 10). The nanostructures are in the range of 2 nm to 5 nm (group-A) and 25 nm to 30 nm (group-B) in size. There also appears the presence of the

larger nanostructures agglomerated as shown in Fig. 11. As evident from the TEM images, the lattice spacing from Fig. 10b and Fig.10d is 0.224 nm and 0.229 nm for the groups A and B respectively. The lattice spacing at 0.229 nm can be attributed to the (111) plane of the silver crystals [61,62] and the spacing of 0.224 nm could arise due to the possible compression of the (111) plane caused by the strain on the surface.The presence of I_2 solution in the silver precursor helps to form silver iodide and the left-over silver ions undergo the reduction mechanisms via plasma-induced cascaded chemistry i.e. either via H$^{\bullet}$ radicals or/and e$^{-}_{aq}$. Therefore, two possible reactions can be of the form:

$$e^{-}_{aq} + Ag^{+} \rightarrow Ag^{0} \qquad (6)$$

$$H^{\bullet} + Ag^{+} \rightarrow Ag^{0} + H^{+} \qquad (7)$$
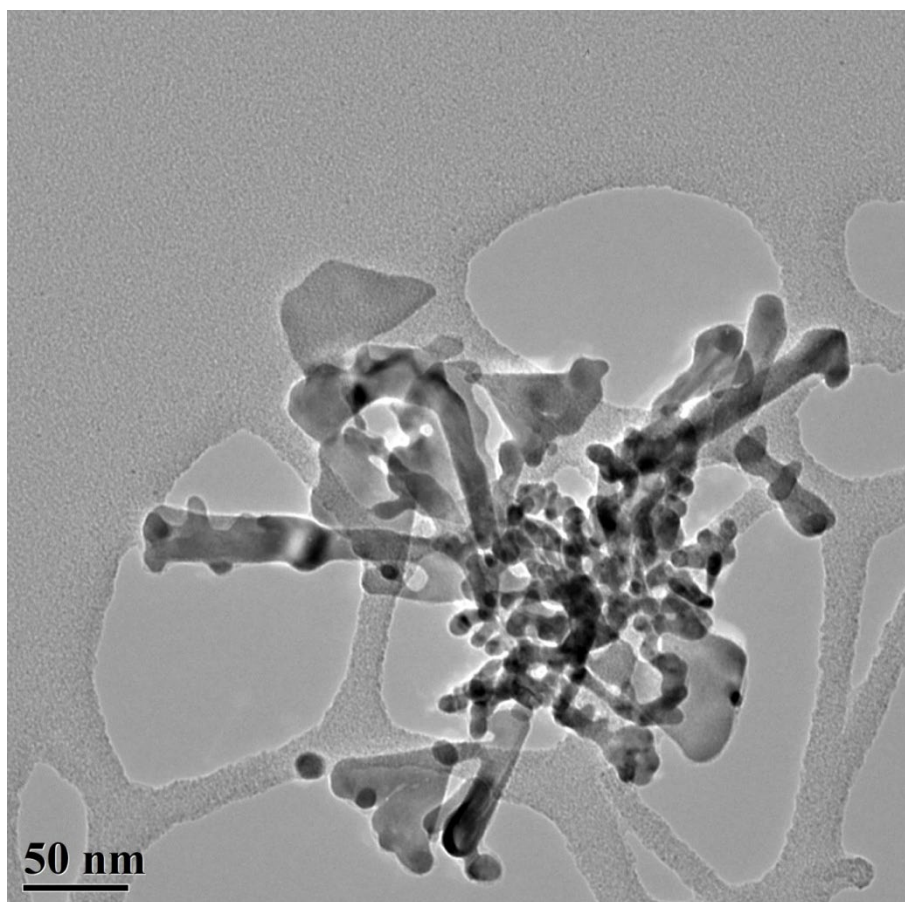
Fig. 11. *Nanostructures produced by plasmatreatment of 0.1 mM I_2 solution mixed with 1 mM $AgNO_3$ solutions at current of 2 mA for the period of 10 minutes.*

Conclusions

In conclusion, it has been observed that hydrogen peroxide is not playing a role of reductant for Ag^{+} cations. The hydrated electrons or/and hydrogen radicals are two possible reactive species serving as a reducing agent for Ag^{+} cations and related synthesis of AgNSs. The presence of ethanol and methanol in the silver nitrate solution seems to accelerate the synthesis mechanism of AgNSs. The experiments conducted with the iodine solutions reflect that fact that the addition of I^{-} ions enhances the process of reduction of Ag^{+} cations and therefore there seems an increment in the density of AgNSs. The analysis from the TEM data suggests that iodine ions generates the

comfortable conditions for the synthesis of small NPs i.e. less than 10 nm. However, the complications of iodine solutions with silver nitrate can be more clarified if there are some quantified interpretations available in terms of solution chemistry. Further analysis can offer a pathway to explore the plasma-induced chemistry for a better control at the reaction kinetics.

Acknowledgements

References

[1] Lee, H., Park, S.H., Jung, S.C., Yun, J.J., Kim, S.J. and Kim, D.H., 2013. Preparation of nonaggregated silver nanoparticles by the liquid phase plasma reduction method. Journal of Materials Research, 28(8), pp.1105-1110. https://doi.org/10.1557/jmr.2013.59

[2] Shuaib, U., Hussain, T., Ahmad, R., Zakaullah, M., Mubarik, F.E., Muntaha, S.T. and Ashraf, S., 2020. Plasma-liquid synthesis of silver nanoparticles and their antibacterial and antifungal applications. Materials Research Express, 7(3), pp.035015. https://doi.org/10.1088/2053-1591/ab7cb6

[3] Skiba, M.I., Vorobyova, V.I. and Kosogina, I.V., 2020. Preparation of silver nanoparticles in a plasma-liquid system in the presence of PVA: antimicrobial, catalytic, and sensing properties. Journal of Chemistry, 3, pp 1-9. https://doi.org/10.1155/2020/5380950

[4] Kondeti, V.S.K., Gangal, U., Yatom, S. and Bruggeman, P.J., 2017. Ag+ reduction and silver nanoparticle synthesis at the plasma–liquid interface by an RF driven atmospheric pressure plasma jet: Mechanisms and the effect of surfactant. Journal of Vacuum Science & Technology A: Vacuum, Surfaces, and Films, 35(6), p.061302. https://doi.org/10.1116/1.4995374

[5] Kim, H.J., Shin, J.G., Park, C.S., Kum, D.S., Shin, B.J., Kim, J.Y., Park, H.D., Choi, M. and Tae, H.S., 2018. In-liquid plasma process for size-and shape-controlled synthesis of silver nanoparticles by controlling gas bubbles in water. Materials, 11(6), p.891. https://doi.org/10.3390/ma11060891

[6] Abou El-Nour, K.M., Eftaiha, A.A., Al-Warthan, A. and Ammar, R.A., 2010. Synthesis and applications of silver nanoparticles. Arabian journal of chemistry, 3(3), pp.135-140. https://doi.org/10.1016/j.arabjc.2010.04.008

[7] Beyene, H.D., Werkneh, A.A., Bezabh, H.K. and Ambaye, T.G., 2017. Synthesis paradigm and applications of silver nanoparticles (AgNPs), a review. Sustainable materials and technologies, 13, pp.18-23. https://doi.org/10.1016/j.susmat.2017.08.001

[8] Verma, P. and Maheshwari, S.K., 2019. Applications of Silver nanoparticles in diverse sectors. International Journal of Nano Dimension, 10(1), pp.18-36.

[9] Tarannum, N. and Gautam, Y.K., 2019. Facile green synthesis and applications of silver nanoparticles: a state-of-the-art review. RSC advances, 9(60), pp.34926-34948. https://doi.org/10.1039/C9RA04164H

[10]　Mariotti, D., Patel, J., Švrček, V. and Maguire, P., 2012. Plasma–liquid interactions at atmospheric pressure for nanomaterials synthesis and surface engineering. Plasma Processes and Polymers, 9(11-12), pp.1074-1085. https://doi.org/10.1002/ppap.201200007

[11]　Patel, J., Němcová, L., Maguire, P., Graham, W.G. and Mariotti, D., 2013. Synthesis of surfactant-free electrostatically stabilized gold nanoparticles by plasma-induced liquid chemistry. Nanotechnology, 24(24), p.245604. https://doi.org/10.1088/0957-4484/24/24/245604

[12]　Huang, T. and Xu, X.H.N., 2010. Synthesis and characterization of tunable rainbow colored colloidal silver nanoparticles using single-nanoparticle plasmonic microscopy and spectroscopy. Journal of materials chemistry, 20(44), pp.9867-9876. https://doi.org/10.1039/c0jm01990a

[13]　Mock, J.J., Barbic, M., Smith, D.R., Schultz, D.A. and Schultz, S., 2002. Shape effects in plasmon resonance of individual colloidal silver nanoparticles. The Journal of Chemical Physics, 116(15), pp.6755-6759. https://doi.org/10.1063/1.1462610

[14]　Sharma, J., Chaki, N.K., Mahima, S., Gonnade, R.G., Mulla, I.S. and Vijayamohanan, K., 2004. Tuning the aspect ratio of silver nanostructures: the effect of solvent mole fraction and 4-aminothiophenol concentration. Journal of Materials Chemistry, 14(6), pp.970-975. https://doi.org/10.1039/b312766b

[15]　Sun, Y., Gates, B., Mayers, B. and Xia, Y., 2002. Crystalline silver nanowires by soft solution processing. Nano letters, 2(2), pp.165-168. https://doi.org/10.1021/nl010093y

[16]　Caswell, K.K., Bender, C.M. and Murphy, C.J., 2003. Seedless, surfactantless wet chemical synthesis of silver nanowires. Nano Letters, 3(5), pp.667-669. https://doi.org/10.1021/nl0341178

[17]　Sun, Y., Yin, Y., Mayers, B.T., Herricks, T. and Xia, Y., 2002. Uniform silver nanowires synthesis by reducing AgNO3 with ethylene glycol in the presence of seeds and poly (vinyl pyrrolidone). Chemistry of Materials, 14(11), pp.4736-4745. https://doi.org/10.1021/cm020587b

[18]　Yang, Y., Hu, Y., Xiong, X. and Qin, Y., 2013. Impact of microwave power on the preparation of silver nanowires via a microwave-assisted method. RSC advances, 3(22), pp.8431-8436. https://doi.org/10.1039/c3ra00117b

[19]　Zhang, W.C., Wu, X.L., Chen, H.T., Gao, Y.J., Zhu, J., Huang, G.S. and Chu, P.K., 2008. Self-organized formation of silver nanowires, nanocubes and bipyramids via a solvothermal method. Acta Materialia, 56(11), pp.2508-2513. https://doi.org/10.1016/j.actamat.2008.01.043

[20]　Zhang, M. and Wang, Z., 2013. Nanostructured silver nanowires-graphene hybrids for enhanced electrochemical detection of hydrogen peroxide. Applied Physics Letters, 102(21), p.213104. https://doi.org/10.1063/1.4807921

[21]　Huang, X.Z., Zhong, X.X., Lu, Y., Li, Y.S., Rider, A.E., Furman, S.A. and Ostrikov, K., 2013. Plasmonic Ag nanoparticles via environment-benign atmospheric microplasma electrochemistry. Nanotechnology, 24(9), p.095604. https://doi.org/10.1088/0957-4484/24/9/095604

[22]　Shi, Q., Vitchuli, N., Nowak, J., Caldwell, J.M., Breidt, F., Bourham, M., Zhang, X. and McCord, M., 2011. Durable antibacterial Ag/polyacrylonitrile (Ag/PAN) hybrid nanofibers prepared by atmospheric plasma treatment and electrospinning. European polymer journal, 47(7), pp.1402-1409. https://doi.org/10.1016/j.eurpolymj.2011.04.002

[23]   Meiss, S.A., Rohnke, M., Kienle, L., Zein El Abedin, S., Endres, F. and Janek, J., 2007. Employing plasmas as gaseous electrodes at the free surface of ionic liquids: deposition of nanocrystalline silver particles. ChemPhysChem, 8(1), pp.50-53. https://doi.org/10.1002/cphc.200600582

[24]   Yu-Tao, Z., Ying, G. and Teng-Cai, M., 2011. Plasma catalytic synthesis of silver nanoparticles. Chinese Physics Letters, 28(10), p.105201. https://doi.org/10.1088/0256-307X/28/10/105201

[25]   Chen, Q., Li, J. and Li, Y., 2015. A review of plasma–liquid interactions for nanomaterial synthesis. Journal of Physics D: Applied Physics, 48(42), p.424005-424030. https://doi.org/10.1088/0022-3727/48/42/424005

[26]   Zou, J.J., Zhang, Y.P. and Liu, C.J., 2006. Reduction of supported noble-metal ions using glow discharge plasma. Langmuir, 22(26), pp.11388-11394. https://doi.org/10.1021/la061795b

[27]   Sato, S., Mori, K., Ariyada, O., Atsushi, H. and Yonezawa, T., 2011. Synthesis of nanoparticles of silver and platinum by microwave-induced plasma in liquid. Surface and Coatings Technology, 206(5), pp.955-958. https://doi.org/10.1016/j.surfcoat.2011.03.110

[28]   Richmonds, C. and Sankaran, R.M., 2008. Plasma-liquid electrochemistry: Rapid synthesis of colloidal metal nanoparticles by microplasma reduction of aqueous cations. Applied Physics Letters, 93(13), p.131501. https://doi.org/10.1063/1.2988283

[29]   Chiang, W.H., Richmonds, C. and Sankaran, R.M., 2010. Continuous-flow, atmospheric-pressure microplasmas: a versatile source for metal nanoparticle synthesis in the gas or liquid phase. Plasma Sources Science and Technology, 19(3), p.034011. https://doi.org/10.1088/0963-0252/19/3/034011

[30]   Chang, F.C., Richmonds, C. and Sankaran, R.M., 2010. Microplasma-assisted growth of colloidal Ag nanoparticles for point-of-use surface-enhanced Raman scattering applications. Journal of Vacuum Science & Technology A: Vacuum, Surfaces, and Films, 28(4), pp.L5-L8. https://doi.org/10.1116/1.3428708

[31]   Lee, S.W., Liang, D., Gao, X.P. and Sankaran, R.M., 2011. Direct writing of metal nanoparticles by localized plasma electrochemical reduction of metal cations in polymer films. Advanced Functional Materials, 21(11), pp.2155-2161. https://doi.org/10.1002/adfm.201100093

[32]   von Brisinski, N.S., Höfft, O. and Endres, F., 2014. Plasma electrochemistry in ionic liquids: From silver to silicon nanoparticles. Journal of Molecular Liquids, 192, pp.59-66. https://doi.org/10.1016/j.molliq.2013.09.017

[33]   Wang, R., Zuo, S., Zhu, W., Wu, S., Nian, W., Zhang, J. and Fang, J., 2014. Microplasma-Assisted Growth of Colloidal Silver Nanoparticles for Enhanced Antibacterial Activity. Plasma Processes and Polymers, 11(1), pp.44-51. https://doi.org/10.1002/ppap.201300038

[34]   Gutierrez, M. and Henglein, A., 1993. Formation of colloidal silver by" push-pull" reduction of silver (1+). The Journal of Physical Chemistry, 97(44), pp.11368-11370. https://doi.org/10.1021/j100146a003

[35]   Salkar, R.A., Jeevanandam, P., Aruna, S.T., Koltypin, Y. and Gedanken, A., 1999. The sonochemical preparation of amorphous silver nanoparticles. Journal of materials chemistry, 9(6), pp.1333-1335. https://doi.org/10.1039/a900568d

[36]   Edelstein, A.S. and Cammaratra, R.C. eds., 1998. Nanomaterials: synthesis, properties and applications. CRC press. https://doi.org/10.1201/9781482268591

[37]   Saito, N., Hieda, J. and Takai, O., 2009. Synthesis process of gold nanoparticles in solution plasma. Thin Solid Films, 518(3), pp.912-917. https://doi.org/10.1016/j.tsf.2009.07.156

[38]   Kapoor, S., Lawless, D., Kennepohl, P., Meisel, D. and Serpone, N., 1994. Reduction and aggregation of silver ions in aqueous gelatin solutions. Langmuir, 10(9), pp.3018-3022. https://doi.org/10.1021/la00021a026

[39]   Chen, Q., Kaneko, T. and Hatakeyama, R., 2012. Reductants in gold nanoparticle synthesis using gas–liquid interfacial discharge plasmas. Applied Physics Express, 5(8), p.086201. https://doi.org/10.1143/APEX.5.086201

[40]   Henglein, A., 1998. Colloidal silver nanoparticles: photochemical preparation and interaction with O_2, CCl_4, and some metal ions. Chemistry of Materials, 10(1), pp.444-450. https://doi.org/10.1021/cm970613j

[41]   Henglein, A. and Giersig, M., 1999. Formation of colloidal silver nanoparticles: capping action of citrate. The Journal of Physical Chemistry B, 103(44), pp.9533-9539. https://doi.org/10.1021/jp9925334

[42]   Pillai, Z.S. and Kamat, P.V., 2004. What factors control the size and shape of silver nanoparticles in the citrate ion reduction method?. The Journal of Physical Chemistry B, 108(3), pp.945-951. https://doi.org/10.1021/jp037018r

[43]   Henglein, A., 1979. Reactions of organic free radicals at colloidal silver in aqueous solution. Electron pool effect and water decomposition. Journal of Physical Chemistry, 83(17), pp.2209-2216. https://doi.org/10.1021/j100480a006

[44]   Tochikubo, F., Shirai, N. and Uchida, S., 2013. Plasma-induced liquid phase reaction in atmospheric pressure glow discharge electrolysis. In 21st International Symposium on Plasma Chemistry (ISPC 21), Cairns Convention Centre, Queensland, Australia Aug. 4-9, 2013.

[45]   Shirai, N., Shimokawa, Y., Aoki, T., Uchida, S. and Tochikubo, F., 2013, September. Plasma electrolysis using atmospheric dc glow discharge in contact with liquid for synthesis of metal nano-particles. In APS Annual Gaseous Electronics Meeting Abstracts (pp. FT3-006).

[46]   Barker, N.T. and Green, J.H., 1964. Iodine as a Scavenger for Hydrogen Atoms in Irradiated Ethanol. Nature, 204(4961), pp.872-873. https://doi.org/10.1038/204872a0

[47]   Jortner, J., Raz, B. and Stein, G., 1960. The far u.-v. absorption spectrum of the iodide ion in aqueous solution. Transactions of the Faraday Society, 56, pp.1273-1275. https://doi.org/10.1039/tf9605601273

[48]   Awtrey, A.D. and Connick, R.E., 1951. The absorption spectra of I_2, I3-, I-, IO3-, S4O6= and S2O3=. Heat of the reaction I3-= I2+ I. Journal of the American Chemical Society, 73(4), pp.1842-1843. https://doi.org/10.1021/ja01148a504

[49]   Backer, H. and Hollowell, J., 2000. Use of iodine for water disinfection: iodine toxicity and maximum recommended dose. Environmental Health Perspectives, 108(8), pp.679-684. https://doi.org/10.1289/ehp.00108679

[50]   Lengyel, I., Epstein, I.R. and Kustin, K., 1993. Kinetics of iodine hydrolysis. Inorganic Chemistry, 32(25), pp.5880-5882. https://doi.org/10.1021/ic00077a036

[51]   Hu, C., Peng, T., Hu, X., Nie, Y., Zhou, X., Qu, J. and He, H., 2010. Plasmon-induced photodegradation of toxic pollutants with Ag− AgI/Al2O3 under visible-light irradiation. Journal of the American Chemical Society, 132(2), pp.857-862. https://doi.org/10.1021/ja907792d

[52]   Zeng, C., Tian, B. and Zhang, J., 2013. Silver halide/silver iodide@ silver composite with excellent visible light photocatalytic activity for methyl orange degradation. Journal of colloid and interface science, 405, pp.17-21. https://doi.org/10.1016/j.jcis.2013.05.009

[53]   Hirsch, H., 1975. Formation of metastable high temperature cubic silver iodide by precipitation. https://doi.org/10.1007/BF01419259

[54]   Patil, K.C., Rao, C.N.R., Lacksonen, J.W. and Dryden, C.E., 1967. The silver nitrate-iodine reaction: Iodine nitrate as the reaction intermediate. Journal of Inorganic and Nuclear Chemistry, 29(2), pp.407-412. https://doi.org/10.1016/0022-1902(67)80044-7

[55]   Bogdanchikova, N., Meunier, F.C., Avalos-Borja, M., Breen, J.P. and Pestryakov, A., 2002. On the nature of the silver phases of Ag/Al2O3 catalysts for reactions involving nitric oxide. Applied Catalysis B: Environmental, 36(4), pp.287-297. https://doi.org/10.1016/S0926-3373(01)00286-7

[56]   Wang, Z.M., Yamaguchi, M., Goto, I. and Kumagai, M., 2000. Characterization of Ag/Al 2 O 3 de-NO x catalysts by probing surface acidity and basicity of the supporting substrate. Physical Chemistry Chemical Physics, 2(13), pp.3007-3015. https://doi.org/10.1039/b000226g

[57]   Micic, O.I., Meglic, M., Lawless, D., Sharma, D.K. and Serpone, N., 1990. Semiconductor photophysics. 5. Charge carrier trapping in ultrasmall silver iodide particles and kinetics of formation of silver atom clusters. Langmuir, 6(2), pp.487-492. https://doi.org/10.1021/la00092a032

[58]   Gnanavel, M. and Sunandana, C.S., 2008, December. Optical absorption and Photoluminescence in ultra thin silver and silver iodide films. In 2008 IEEE PhotonicsGlobal@ Singapore (pp. 1-4). IEEE. https://doi.org/10.1109/IPGC.2008.4781352

[59]   Šileikaitė, A., Puišo, J., Prosyčevas, I. and Tamulevičius, S., 2009. Investigation of silver nanoparticles formation kinetics during reduction of silver nitrate with sodium citrate. Materials Science (Medžiagotyra), 15(1), pp.21-27.

[60]   Henglein, A., 1989. Small-particle research: physicochemical properties of extremely small colloidal metal and semiconductor particles. Chemical reviews, 89(8), pp.1861-1873. https://doi.org/10.1021/cr00098a010

[61]   Khan, M.A.M., Kumar, S., Ahamed, M., Alrokayan, S.A. and AlSalhi, M.S., 2011. Structural and thermal studies of silver nanoparticles and electrical transport study of their thin films. Nanoscale research letters, 6(1), pp.1-8. https://doi.org/10.1186/1556-276X-6-434

[62]   Lu, G., 2007. Engineering nanoparticles and nanoparticle-carbon nanotube hybrid structures for miniaturized gas sensors. The University of Wisconsin-Milwaukee.

Exploring Electronic Structure and Optical Properties of 2D Monolayer As₂S₃ by First-Principle's Calculation

Abhishek Patel[1, a *], Deobrat Singh[2], Yogesh Sonvane[3], P.B. Thakor[1] and Rajeev Ahuja[2,4]

[1]Department of Physics, Veer Narmad South Gujarat University, Surat 395007, India

[2]Materials Theory Division, Uppsala University, Box 516, Uppsala 75120, Sweden

[3]Department of Physics, Sardar Vallabhbhai National Institute of Technology, Surat 395007, India

[4]Department of Physics, Indian Institute of Technology Ropar, Rupnagar 140001, India

* arpatel14@hotmail.com

Abstract. In the present work, the structural, electronic and optical properties of the 2D monolayer As₂S₃ have been systematically investigated by the first principles calculations. The monolayer As₂S₃ has stable structure in the 2D oblique lattice which is confirm by phonon dispersion. Here, the elemental projected band-structure and density of states of the monolayer As₂S₃ have been determined by using HSE functional. The calculated bandgap of the monolayer As₂S₃ has 3.29 eV (of the indirect nature). In the optical properties, the complex dielectric function and optical absorption spectrum have been studied. The results suggest that the 2D monolayer As₂S₃ as hopeful candidate for potential applications in nano-electronics and opto-electronics.

Introduction

Among the all material families, the family of the 2D materials draw outstanding research attentions due to their remarkable electronic, mechanical, optical and others properties after the discovery and experimental realization of graphene in the year 2004[1,2]. The new members are continuously being added through theoretical predications and experimental investigations in the expanding family of 2D materials [3–6]. The 2D materials such as graphene, boron nitride (h-BN), silicene, germanene, TMDs, MXenes and etc. have high symmetric and isotropic lattice due to their hexagonal structure[7–12]. These conventional 2D materials fail to desirable performance in the direction dependent optoelectronic technology[5,13].The two-dimensional materials with low symmetry, such as borophene, phosphorene 1T' phase of TMDs and germanium phosphide have diversity in properties due to their anisotropic lattice structure[5,13]. These low symmetrical systems with diverse properties and feature can become solution for frequency and direction dependent devices due to their anisotropy[13]. The broad family of the 2D materials can fabricated by various experimental methods such as chemical vapor deposition (CVD), pulse laser deposition (PLD) method, molecular beam epitaxy (MBE) and others[14,15]. The two-dimensional (2D) semiconductor materials in the form of monolayer, bilayer and few-layers have novel combination of the electronic and optical properties[15]. It leads toward new electronic and optoelectronic devices with ultrathin thickness and flexibilities due to new physics behind their electronic structures and the screening in the 2D systems[15].

The two-dimensional (2D) materials with anisotropy can open new era of optoelectronic technology due to their orientation dependent and frequency dependent properties. The 2D black phosphorus (bP) has the large anisotropy but it is an unstable material due to its degradation in the air[13,16,17]. The 2D material with high anisotropy and stability can become a good alternative. As_2S_3 has layered structure in bulk phase and is important member of anisotropic material family. The arsenic based layered materials are useful in the electronic devices, sensors and energy system[5,18]. Recently, the 2D nanosheet of layered material As_2S_3 has been experimentally synthesized by Siskins et al.[13]. The monolayer As_2S_3 have outstanding chemical stability, high anisotropy and high thermal and dynamic stabilities[13,19]. Motivated by these interesting consequences, the structural properties, phonon-dispersion, elemental projected electronic band-structure, and optical properties of the monolayer As_2S_3 are explored using the first-principle's calculations in this work.

Computational Details

The first-principle calculations have been performed using the VASP code in this work[20,21]. The ground state energy of monolayer As_2S_3 is calculated by using the DFT calculations through Generalized Gradient Approximation (GGA) method with exchange-correlation (XC) function of Perdew-Burke-Ernzerhof (PBE)[22]. The projected augmented wave method is employed within Energy Cut-off of 500eV to approximate the core-valence electron interactions[23]. The thick vacuum of 20 Å has been inserted in the structure to avoid interaction between periodic layers in y direction[19,24–26]. By setting criteria for the total energy to 10^{-8} eV/cell and the force to 0.01 eV/Å, the structure of this material is optimized using the Monkhorst k-point grid of 7×1×7 through the conjugate gradient method[27]. Density functional perturbation theory (DPFT) calculation is performed using the supercell of the size 3×1×3 for the monolayer As_2S_3[28,29]. The phonon-dispersion of this material is calculated by using the phonopy software.[30] For the visualization of monolayer As_2S_3, the VESTA software is used[31]. To obtain accurate electronic properties of the monolayer As_2S_3, the HSE method is employed by taking screening parameter (β) = 0.2 Å^{-1} and mixing parameter (α) = 0.25. The optical absorption ($\alpha(\omega)$) can be determined using the real and imaginary functions using following expressions:

$$\alpha(\omega) = \frac{4\pi E \sqrt{(|\varepsilon(\omega)| - \varepsilon_1(\omega))}}{hc}$$

where, $|\varepsilon(\omega)| = \sqrt{\varepsilon_1^2(\omega) + \varepsilon_2^2(\omega)}$, is the relative dielectric function and E is photon energy[32,33].

Results and discussion

Structural properties

The optimized structure of monolayer As_2S_3 is illustrated in the Fig.-1. In this material, the 3 coordinated As and 2 coordinated S atoms are arranged in the monoclinic lattice arrangement in Pc space group. The optimized lattice-constants of monolayer form of this 2D material are a = 4.66 Å and c =12.42 Å. While the calculated the lattice-constants of bulk-phase are a = 4.60 Å, b = 11.01 Å and c =12.26 Å. The unit-cell of monolayer As_2S_3 with two formula unit of As_2S_3 satisfies the octet rule. This monolayer material has large asymmetry due to its monoclinic arrangement in lattice space, while the other materials, like graphene, TMDs have good symmetry due to hexagonal lattice arrangement of atoms. To check the dynamic stability, the phonon band-structure for the single layer (SL) of As_2S_3 along the high symmetry path (Γ-Z-C-Y- Γ) is computed through

the DPFT method. The calculated phonon-dispersion spectra for single layer of As_2S_3 is shown in the Fig.-1(d). The positive phonon dispersion of monolayer As_2S_3 confirms the dynamic stability of structure. Here, the phonon density of states is also compatible with the phonon band-structure.
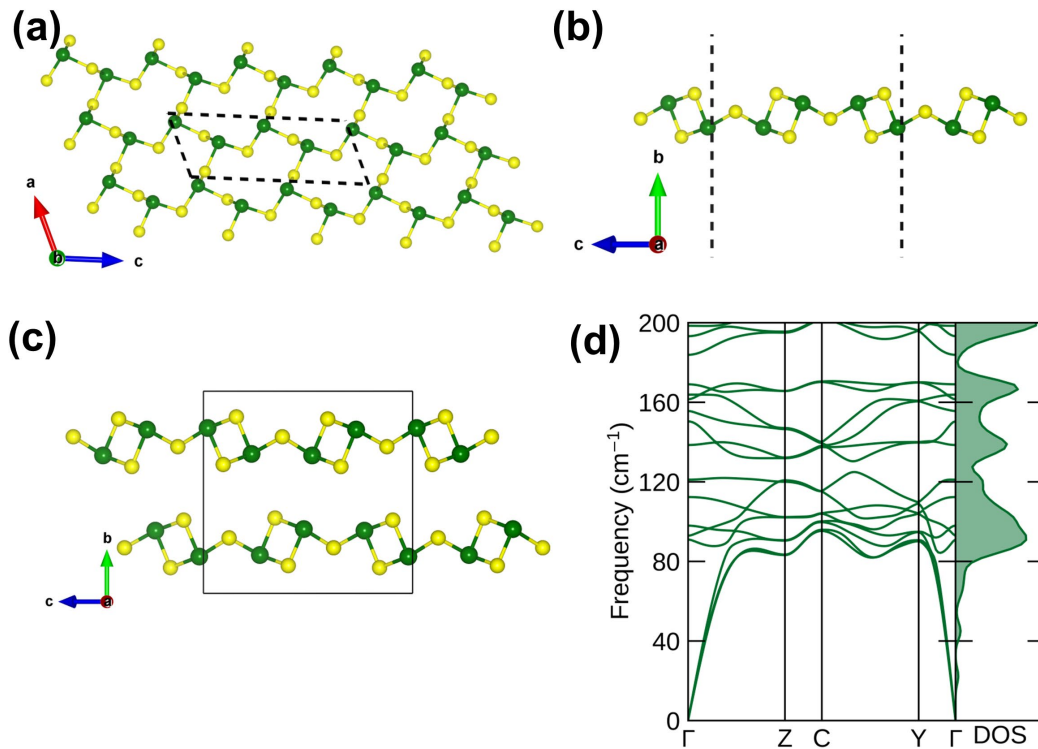
(a)

(b)

(c)

(d)

Fig.-1: (a) top view of monolayer As_2S_3, (b) sideview of monolayer As_2S_3 (c) bulk-phase of As_2S_3 and (d) phonon dispersion of monolayer As_2S_3
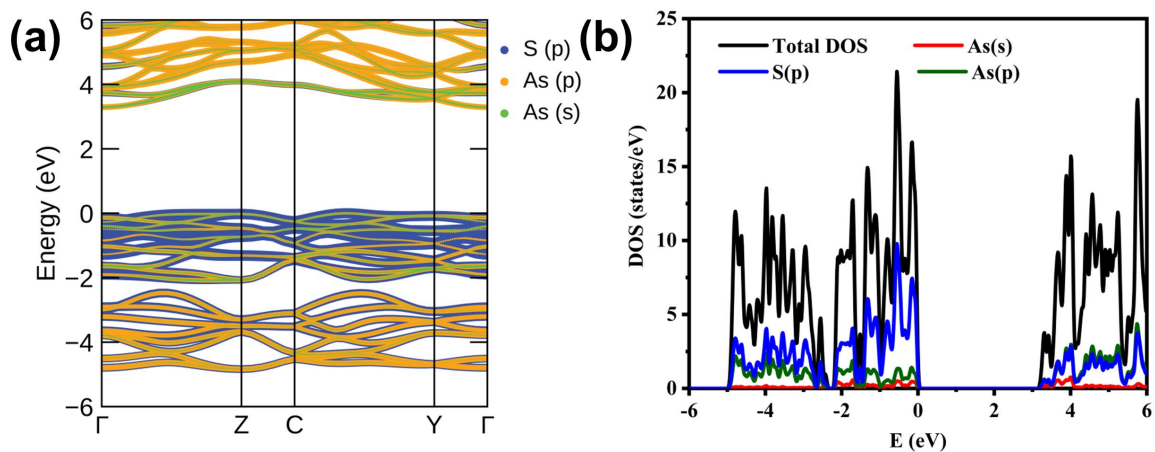
Electronic properties

(a)

(b)

Fig.-2: (a) Electronic Band-Structure and (b) Density of States for the monolayer As_2S_3

Table 1: Electronic bandgap of 2D monolayer As_2S_3

Material	Structure	Functional	Indirect Bandgap (eV)	Direct Bandgap (eV)
As_2S_3 (monolayer)	monoclinic	HSE06	3.29	3.43
As_2S_3 (monolayer)	monoclinic	PBE	2.31	2.47

The calculated the elemental projected electronic band-structure and the projected density of states (PDOS) has been illustrated in Fig.-2. Here, the elemental projected band-structure using hybrid HSE06 is computed for the monolayer As_2S_3 along the symmetry path Γ-Z-C-X- Γ. This monolayer As_2S_3 exhibits semiconducting behavior with the indirect bandgap of 3.29 eV and the direct bandgap of 3.43 eV (see Table 1). In the elemented projected electronic band-structure of monolayer As_2S_3, it is clearly observed that the conduction band mainly composed of the contribution of p-orbital of As along with significant contribution of p-orbital of S atom and while in the composition of the valence band, the dominant contribution of p-orbital of sulfer has been observed with presence of s-orbital and p-orbital of As atom (see Fig.-2(a)). Here, the contribution of the p-orbital of As increases in valence band from near fermi-level toward far from fermi-level. From the analysis of the partial density of states of monolayer As_2S_3, the p-orbitals of arsenic (As) and sulfer(S) atoms have major contribution in the formation of total density (see Fig.-2(b)). In the conduction band, they are strongly hybridized with each other and almost equality contributes in the formation of total density. While in the valence band, the p-orbital of S atom has dominant contribution than the other orbitals. In the valence band and conduction band, there is also observed the small contribution the s-orbital of As atoms. Here, the projected density of states of the monolayer As_2S_3 is highly analogues with electronic band-structure of it.
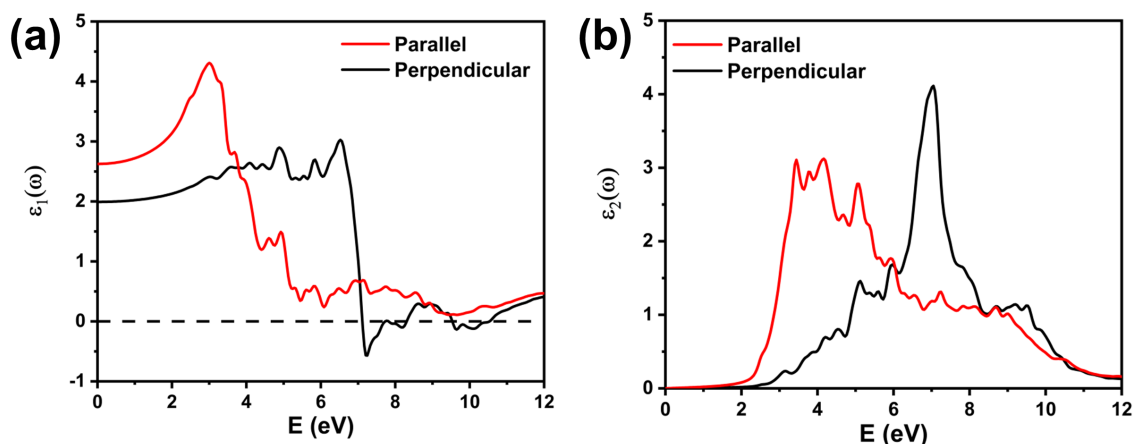
Optical properties

Fig.-3: Calculated complex dielectric constant of monolayer As_2S_3 :(a) real part and (b) imaginary part

The real and imaginary part of the calculated frequency dependent complex dielectric constant of 2D monolayer As_2S_3 has been illustrated in the Fig.-3. The electronic polarizability of the

material is directly related with the real dielectric function through the Clausius-Mossoti relation. The monolayer As_2S_3 shows the static value of real dielectric function (at photon energy E=0) is at 2.62 for the in-plane direction and is 1.99 for the out-plane direction (see Fig.3(a)). The maximum electronic polarizability is located at the photon energies 2.92 eV in visible region for direction parallel to field and at photon energy 7.17 eV for the perpendicular field direction. In the perpendicular field direction, the real dielectric constant shows negative values for some photon frequencies which describes metallic response for those photon energies. The monolayer As_2S_3 shows maximum negative value of real dielectric function for the photon energy 7.24 eV in UV region. While the imaginary dielectric function concerns with the electronic inter-band transitions. In direction parallel to the field, the first three peaks of imaginary dielectric constant have been located at the photon energies 3.41 eV, 3.76 eV and 4.15 eV (see Fig.3(b)). While for the case of perpendicular field direction, the first peak of imaginary dielectric constant has been observed at the photon energies 3.16 eV. The strongest peak of the imaginary dielectric function is located at photon energy 7.04 eV for the out-plane direction (perpendicular field direction).
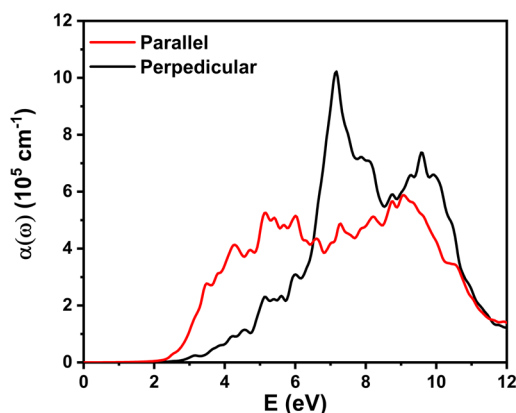

Fig.-4: Calculated optical absorption spectrum of the monolayer As_2S_3

The anisotropic optical absorption spectrum of the monolayer As_2S_3 has been illustrated in the Fig.-4. The monolayer As_2S_3 has absorption of the order 10^5 cm^{-1} for visible and UV frequencies in the both cases, parallel field and perpendicular field direction cases. For the infrared and visible frequencies having photon energy below the 2 eV, the monolayer As_2S_3 shows negligible optical absorption in both cases (in-plane direction and out-plane direction to field). In the optical absorption spectrum of monolayer As_2S_3, the large anisotropy is observed between parallel field and perpendicular field directions. This monolayer material shows the strongest absorption peak at photon energy 7.17 eV in the ultra-violet region for the out-plane direction (perpendicular direction).

Conclusion

In the present investigation, the structural, electronic properties and optical properties of 2D layered As_2S_3 have been studied for monolayer phase. The dynamically stability of monolayer phase of the 2D As_2S_3 has been confirmed by the positive phonon dispersion. The monolayer As_2S_3 is wide bandgap semiconductor with indirect electronic bandgap of 3.29 eV. This material has shown large optical absorption for visible and UV frequencies. The monolayer As_2S_3 displays anisotropic optical properties along the in-plane and out-of-plane directions. The result of the current investigation suggests the monolayer As_2S_3 for the potential applications in the field of the nanoelectronics and optoelectronics.

Conflicts of Interest
The authors declare no conflicts of interest.

References

[1] C. Lee, X. Wei, J.W. Kysar, J. Hone, Measurement of the Elastic Properties and Intrinsic Strength of Monolayer Graphene, Science (80-.). 321 (2008) 385 LP – 388. https://doi.org/10.1126/science.1157996

[2] D. Tyagi, H. Wang, W. Huang, L. Hu, Y. Tang, Z. Guo, Z. Ouyang, H. Zhang, Recent advances in two-dimensional-material-based sensing technology toward health and environmental monitoring applications, Nanoscale. 12 (2020) 3535–3559. https://doi.org/10.1039/C9NR10178K

[3] A.K. Geim, K.S. Novoselov, The rise of graphene, Nat. Mater. 6 (2007) 183–191. https://doi.org/10.1038/nmat1849

[4] K.S. Novoselov, A.K. Geim, S. V Morozov, D. Jiang, Y. Zhang, S. V Dubonos, I. V Grigorieva, A.A. Firsov, Electric Field Effect in Atomically Thin Carbon Films, Science (80-.). 306 (2004) 666 LP – 669. https://doi.org/10.1126/science.1102896

[5] B. Mortazavi, F. Shojaei, M. Azizi, T. Rabczuk, X. Zhuang, As2S3, As2Se3 and As2Te3 nanosheets: Superstretchable semiconductors with anisotropic carrier mobilities and optical properties, J. Mater. Chem. C. 8 (2020) 2400–2410. https://doi.org/10.1039/C9TC05904K

[6] A. Patel, D. Singh, Y. Sonvane, P.B. Thakor, R. Ahuja, Impact of stacking on the optoelectronic properties of 2D ZrS2/GaS heterostructure, Mater. Today Proc. 47 (2021) 526–528. https://doi.org/10.1016/j.matpr.2020.10.385

[7] B. Radisavljevic, A. Radenovic, J. Brivio, V. Giacometti, A. Kis, Single-layer MoS2 transistors, Nat. Nanotechnol. 6 (2011) 147–150. https://doi.org/10.1038/nnano.2010.279

[8] E. Bianco, S. Butler, S. Jiang, O.D. Restrepo, W. Windl, J.E. Goldberger, Stability and Exfoliation of Germanane: A Germanium Graphane Analogue, ACS Nano. 7 (2013) 4414–4421. https://doi.org/10.1021/nn4009406

[9] D. Nakamura, H. Nakano, Liquid-Phase Exfoliation of Germanane Based on Hansen Solubility Parameters, Chem. Mater. 30 (2018) 5333–5338. https://doi.org/10.1021/acs.chemmater.8b02153

[10] L. Song, L. Ci, H. Lu, P.B. Sorokin, C. Jin, J. Ni, A.G. Kvashnin, D.G. Kvashnin, J. Lou, B.I. Yakobson, P.M. Ajayan, Large Scale Growth and Characterization of Atomic Hexagonal Boron Nitride Layers, Nano Lett. 10 (2010) 3209–3215. https://doi.org/10.1021/nl1022139

[11] Y. Kubota, K. Watanabe, O. Tsuda, T. Taniguchi, Deep Ultraviolet Light-Emitting Hexagonal Boron Nitride Synthesized at Atmospheric Pressure, Science (80-.). 317 (2007) 932 LP – 934. https://doi.org/10.1126/science.1144216

[12] P. Vogt, P. De Padova, C. Quaresima, J. Avila, E. Frantzeskakis, M.C. Asensio, A. Resta, B. Ealet, G. Le Lay, Silicene: Compelling Experimental Evidence for Graphenelike Two-Dimensional Silicon, Phys. Rev. Lett. 108 (2012) 155501. https://doi.org/10.1103/PhysRevLett.108.155501

[13] M. Šiškins, M. Lee, F. Alijani, M.R. Van Blankenstein, D. Davidovikj, H.S.J. Van Der Zant, P.G. Steeneken, Highly Anisotropic Mechanical and Optical Properties of 2D Layered As2S3 Membranes, ACS Nano. 13 (2019) 10845–10851. https://doi.org/10.1021/acsnano.9b06161

[14] A. Zavabeti, A. Jannat, L. Zhong, A.A. Haidry, Z. Yao, J.Z. Ou, Two-Dimensional Materials in Large-Areas: Synthesis, Properties and Applications, Nano-Micro Lett. 12 (2020) 66. https://doi.org/10.1007/s40820-020-0402-x

[15] M. Bernardi, C. Ataca, M. Palummo, J.C. Grossman, Optical and Electronic Properties of Two-Dimensional Layered Materials, Nanophotonics. 6 (2017) 479–493. https://doi.org/10.1515/nanoph-2015-0030

[16] M. Moreno-Moreno, G. López-Polín, A. Castellanos-Gomez, C. Navarro, J. Gomez-Herrero, Environmental Effects in Mechanical Properties of Few-layer Black Phosphorus, 2D Mater. 3 (2016) 31007. https://doi.org/10.1088/2053-1583/3/3/031007

[17] J. Tao, W. Shen, S. Wu, L. Liu, Z. Feng, C. Wang, C. Hu, P. Yao, H. Zhang, W. Pang, X. Duan, J. Liu, C. Zhou, D. Zhang, Mechanical and Electrical Anisotropy of Few-Layer Black Phosphorus, ACS Nano. 9 (2015) 11362–11370. https://doi.org/10.1021/acsnano.5b05151

[18] S. Zhang, S. Guo, Z. Chen, Y. Wang, H. Gao, J. Gómez-Herrero, P. Ares, F. Zamora, Z. Zhu, H. Zeng, Recent progress in 2D group-VA semiconductors: from theory to experiment, Chem. Soc. Rev. 47 (2018) 982–1021. https://doi.org/10.1039/C7CS00125H

[19] A. Patel, D. Singh, Y. Sonvane, P.B. Thakor, R. Ahuja, Bulk and monolayer As2S3 as promising thermoelectric material with high conversion performance, Comput. Mater. Sci. 183 (2020) 109913. https://doi.org/10.1016/j.commatsci.2020.109913

[20] G. Kresse, J. Furthmüller, Efficient iterative schemes for ab initio total-energy calculations using a plane-wave basis set, Phys. Rev. B - Condens. Matter Mater. Phys. 54 (1996) 11169–11186. https://doi.org/10.1103/PhysRevB.54.11169

[21] G. Kresse, J. Furthmüller, Efficiency of ab-initio total energy calculations for metals and semiconductors using a plane-wave basis set, Comput. Mater. Sci. 6 (1996) 15–50. https://doi.org/10.1016/0927-0256(96)00008-0

[22] J.P. Perdew, K. Burke, M. Ernzerhof, Generalized gradient approximation made simple, Phys. Rev. Lett. 77 (1996) 3865–3868. https://doi.org/10.1103/PhysRevLett.77.3865

[23] D. Joubert, From ultrasoft pseudopotentials to the projector augmented-wave method, Phys. Rev. B - Condens. Matter Mater. Phys. 59 (1999) 1758–1775. https://doi.org/10.1103/PhysRevB.59.1758

[24] Y. Xu, Y. Li, X. Chen, C. Zhang, R. Zhang, P. Lu, First-principle study of hydrogenation on monolayer MoS2, AIP Adv. 6 (2016) 75001. https://doi.org/10.1063/1.4955430

[25] H. Li, C. Tsai, A.L. Koh, L. Cai, A.W. Contryman, A.H. Fragapane, J. Zhao, H.S. Han, H.C. Manoharan, F. Abild-Pedersen, J.K. Nørskov, X. Zheng, Activating and optimizing MoS2 basal planes for hydrogen evolution through the formation of strained sulphur vacancies, Nat. Mater. 15 (2016) 48–53. https://doi.org/10.1038/nmat4465

[26] E.N. Voronina, L.S. Novikov, Ab initio study of unzipping processes in carbon and boron nitride nanotubes under atomic oxygen impact, RSC Adv. 3 (2013) 15362–15367. https://doi.org/10.1039/c3ra41742e

[27] H.J. Monkhorst, J.D. Pack, Special points for Brillouin-zone integrations, Phys. Rev. B. 13 (1976) 5188–5192. https://doi.org/10.1103/PhysRevB.13.5188

[28] H. Shang, C. Carbogno, P. Rinke, M. Scheffler, Lattice dynamics calculations based on density-functional perturbation theory in real space, Comput. Phys. Commun. 215 (2017) 26–46. https://doi.org/10.1016/j.cpc.2017.02.001

[29] G. Kresse, J. Furthmüller, J. Hafner, Ab initio Force Constant Approach to Phonon Dispersion Relations of Diamond and Graphite, Europhys. Lett. 32 (1995) 729–734. https://doi.org/10.1209/0295-5075/32/9/005

[30] A. Togo, I. Tanaka, First principles phonon calculations in materials science, Scr. Mater. 108 (2015) 1–5. https://doi.org/10.1016/j.scriptamat.2015.07.021

[31] K. Momma, F. Izumi, VESTA 3 for three-dimensional visualization of crystal, volumetric and morphology data, J. Appl. Crystallogr. 44 (2011) 1272–1276. https://doi.org/10.1107/S0021889811038970

[32] D. Singh, S.K. Gupta, Y. Sonvane, I. Lukačević, Antimonene: a monolayer material for ultraviolet optical nanodevices, J. Mater. Chem. C. 4 (2016) 6386–6390. https://doi.org/10.1039/C6TC01913G

[33] H.R. Mahida, D. Singh, Y. Sonvane, P. Thakor, R. Ahuja, S. Gupta, The influence of edge structure on the optoelectronic properties of Si2BN quantum dot, J. Appl. Phys. 126 (2019) 0. https://doi.org/10.1063/1.5131149

Prediction of Electronic and Optical Properties of Boron Selenide BSe (2H) monolayer based on First-Principles

Pushkar Mishra[1, a *], and Yogesh Sonvane[1]

[1]Applied Material Lab, Department of Physics, S. V. National Institute of Technology, Surat, 395007, India.

[a]mishrapushkar95@gmail.com

Abstract. In this study, we examined some properties of 2D monolayer of Boron selenide BSe (2H) such as structural, electronic and optical properties. The BSe (2H) monolayer has an indirect bandgap of 2.62eV from Γ to M points. We explored from density of states (DOS), in valance band close to fermi level 4p state of selenium (Se) atom is hybridized with 2p state of B atom, but close to lower part of conduction band 2p state of boron (B) atom is ascendant over the 4p state of selenium atom. We have also calculated optical parameter like imaginary and real component of dielectric function, refractive index, absorption coefficient from random phase approximation method(RPA).

Introduction

Due to their interesting electrical, optical, thermal and mechanical properties 2D materials have gained much attention in recent years; which allows for more versatile future applications in nano-electronic devices [1-4]. The search of new 2D materials is still a top main target of material researcher, since of their surface area is high and ability to tune the properties [5,6]. Recently baron-based chalcogenides, in the form of 2D monolayer, analogues to indium selenide [7] are attracting a lot of interest because their special properties greater stretchability, tensile strength [8], and high carrier mobility [9]. BS, BSe and BTe are three popular boron monochalcogenides. They are mainly found in two type of atomic structures 1T and 2H. In 1T structure ABBC type of atomic layers sequence found, and in 2H structure ABBA type of atomic layer sequence is obtained.

In this study, we examined structural, electronic, and optical properties of boron selenide BSe (2H) monolayer by utilizing first principle calculations.

Methodology

The density functional theory was used in all of the simulations and have been executed in the Vienna Ab-into Simulation Package (VASP) code [10]. We choose pseudopotential, projector augmented wave (PAW) and generalized gradient approximation GGA-PBE method suggested by Perdew et.al [11] was used to deal with exchange correlation energy. For plane wave basis set, we select cut off 500 eV. The force and energy convergence level were set at 0.005 eV/Å and 10^{-5} eV. For optimization using the Mon-khorst-pack scheme [12] the k-points for Brillouin Zone sample size is given as 19x19x1. We have given 15Å vacuum in vertical direction to avoid the possibility of interaction between two layers. For investigating optical properties, we have used random phase approximation (RPA) method [13]. In order to display atomic structure, the VESTA [14] code was used.

Results and Discussions

Structure properties

Figure1 depicts the completely optimised structure of boron selenide BSe (2H) monolayer. It is made of two buckled BSe layers of that are joined in such a way that two B atoms are sandwiched between Se atoms. The calculated bond length B-Se is 2.10Å and lattice constant, a = 3.25Å. The bond length after optimization, between top B atom and bottom B atom (fig. 1(b)) is 1.71Å. Similarly, the distance between upper and lower Se atom (fig.1 (b)) is 3.60Å. The calculated bond angles are ∠BSeB = 101.34° ∠SeBSe = 101.34° ∠SeBB = 116.72°. The buckling parameter is 0.95Å, this is in accordance with previous work [8].
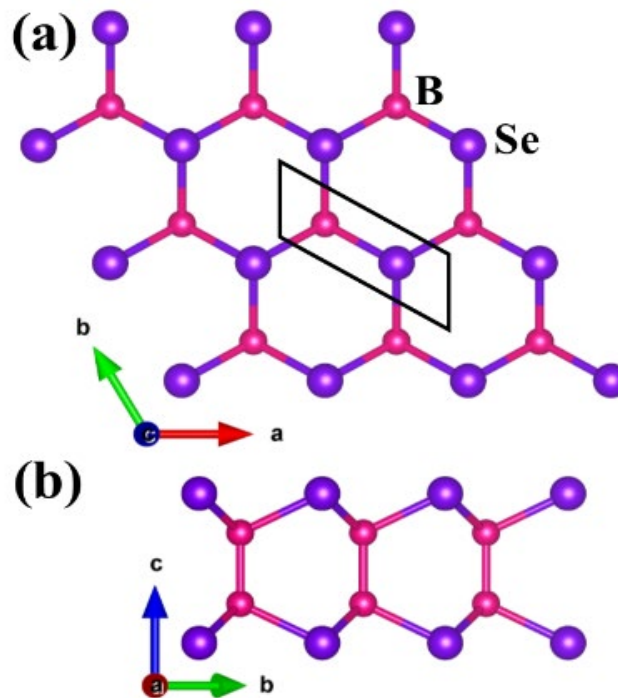

Figure 1. Optimised structure of 2D boron selenide BSe (2H), (a)
top view (b) side view.

Electronic properties

For investigation of electronic properties, we have calculated band structure and density of states (DOS) for boron selenide BS (2H) monolayer. From fig. 2(a) we obtained the indirect band gap of 2.62 eV along Γ to M direction. As shown in fig. 2(b) density of states. In valance band near fermi level, p state of Se atom ascendant over all states. But close to the lower part of conduction band p state of B atom ascendant over the all states. This demonstrates that an electron transition will occur between the p state of Se and the p state of B atom mainly. Although away from the conduction band p state of B atom is hybridized with p state of Se atom. Meanwhile in valance band away from fermi energy p state of Se atom is not hybridized with p state of B atom. Besides the s states of B atom and Se atom have very less contribution in density of sates (DOS) of BSe (2H) monolayer.
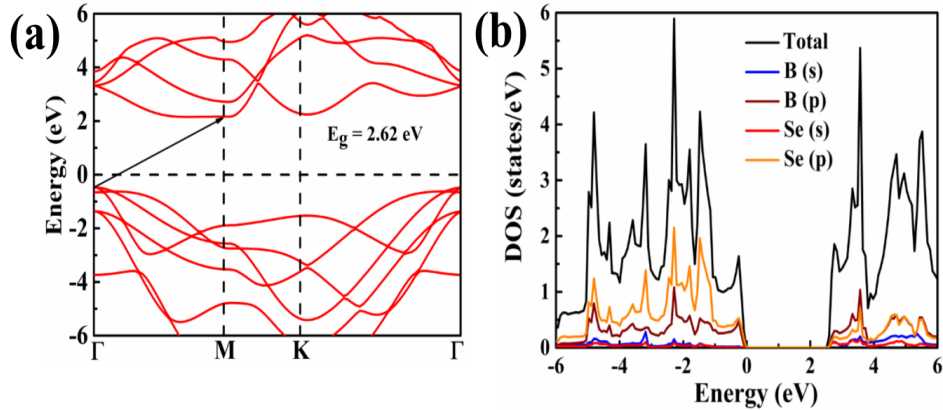
*Figure 2. (a) and (b) represents band structure and density of states (DOS)
of boron selenide BSe (2H) monolayer*

Optical properties

We used random phase approximation (RPA) method to determine imaginary and real parts of complex dielectric function for optical properties calculation. The complex dielectric function $\varepsilon(\omega)$, is defined as $\varepsilon(\omega) = \varepsilon_r(\omega) + i\varepsilon_i(\omega)$ where $\varepsilon_r(\omega)$ is real part and $\varepsilon_i(\omega)$ imaginary part of dielectric function of BSe (2H) monolayer. The optical properties have been determined in both directions in plane of polarisation (E||X) and perpendicular to plane of polarisation (E||Z). Fig. 3 represents the optical properties of BSe (2H) monolayer

Fig. 3(a) illustrate $\varepsilon_i(\omega)$ frequency dependent imaginary part of dielectric function vs photon energy. When a material is transparent for particular photon energy, the imaginary dielectric function $\varepsilon_i(\omega)$, became zero, but when absorption begins, the imaginary dielectric function turns non-zero. For E||X, imaginary dielectric function nearly zero till 1.70 eV, after 1.70eV absorption started reached maximum at 5.83 eV and become zero again after 35.0 eV. That is suggested that absorption occurs between 1.70eV and 35 eV, which can also be seen in Fig. 3(d). For E||Z, $\varepsilon_i(\omega)$, remains zero till 4.2 eV and reaches maximum at 18.52 eV, and after 35.0 eV tuns to zero. That implying material is transparent for less than 4.2 eV and more than 35 eV.

According to fig. 3(b) which shows the graph between real part of dielectric constant $\varepsilon_r(\omega)$ and photon energy. $\varepsilon_r(\omega)$ describes how much a material becomes polarised when an electric field is applied due to the formation of electric dipoles. At zero energy the value of $\varepsilon_r(\omega)$ is considered as static dielectric function. From fig. 3(b), the determined static dielectric function is 4.11 for E||X and 1.58 for E||Z, which is asserting the material have high polarizability in X direction [15].

Figure 3(c) represents how does material's refractive index connect with photon energy. Static refractive index is 2.02 for E||X, and 1.04 for E||Z. It is obvious from fig. 3(c) refractive index begins 0eV reaches highest value 2.71 at 4.76 eV (E||X), 1.44 at 17.5 eV (E||Z) after this graph decreases gradually and reached at minimum value 0.50 at 13.03 eV(E||X) and 0.75 at 23.42 eV (E||Z) after this both these curve increases slowly and become constant after 40 eV.

The absorption spectra are depicted in Fig. 3(d). The absorption in nearly zero till 2.00 eV for E||X, and 3.88 eV for E||Z. Although in the case of E||Z, curve have some small peaks at 6.25 eV, 9.19 eV and 12.97 eV, that means some absorption is also possible at these corresponding photon energies. The maximum peak of absorption lies at 8.72 eV for E||X, and at 19.47 eV for E||Z, both energies are coming at ultraviolet (UV) of electromagnetic spectrum. It ensures that material have strong ability to absorb UV radiation.
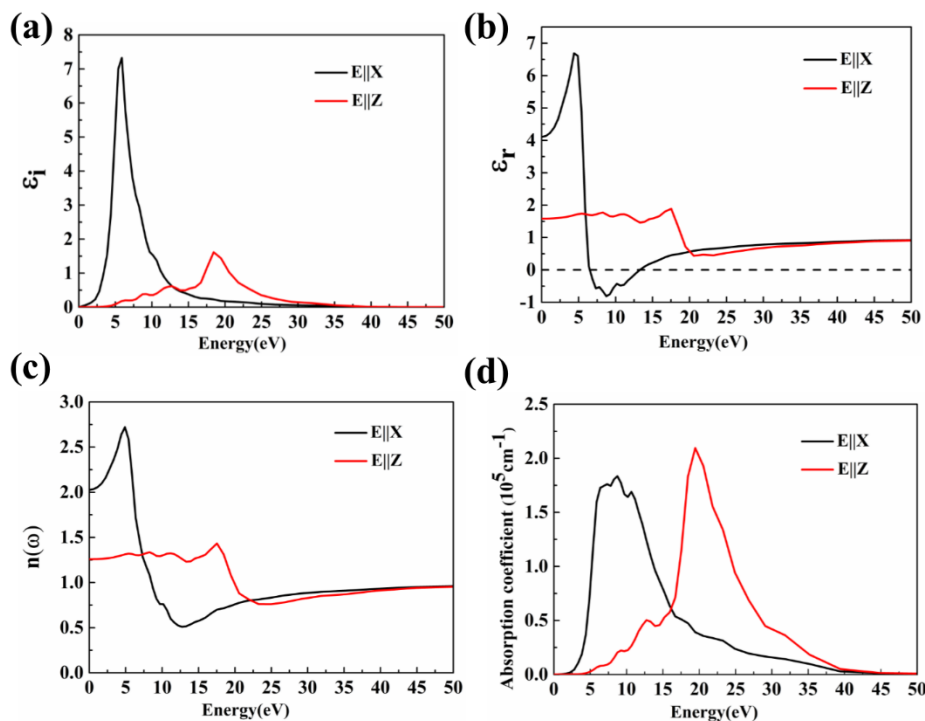

Figure 3 The optical properties (a) imaginary part of dielectric function (b) real part of dielectric function (c) refractive index (d) absorption coeffcent of BSe (2H) monolayer.

Summary

We examined the structural, electronic, and optical properties of BSe (2H) monolayer by using DFT framework. The results show that BSe (H) is an indirect 2.62 eV band gap. The maximum absorption peaks observed at 8.72 eV (E||X) and 19.72 eV (E||Z), which lies in UV region. According to these theoretical results, the 2D BSe (2H) monolayer is viable UV absorption candidate.

References

[1] P. Miró, M. Audiffred, T. Heine, An atlas of two-dimensional materials, Chem. Soc. Rev., 43 (2014) 6537-6554. https://doi.org/10.1039/C4CS00102H

[2] X. Song, J. Hu, H. Zeng, Two-dimensional semiconductors: recent progress and future perspectives, J. Mater. Chem. C 1, (2013) 2952–2969. https://doi.org/10.1039/c3tc00710c

[3] K. J. Koski, Y. Cui, The New Skinny in Two-Dimensional Nanomaterials, Acs Nano 7, (2013) 3739–3743. https://doi.org/10.1021/nn4022422

[4] M. Xu, T. Liang, M. Shi, and H. Chen, Graphene-Like Two-Dimensional Materials Chemical reviews 113, (2013) 3766–3798. https://doi.org/10.1021/cr300263a

[5] A. K. Geim, K. S. Novoselov, The rise of graphene. Nature Mater 6, (2007) 183–191. https://doi.org/10.1038/nmat1849

[6] Q. Liu, X. Zhang, L. Abdalla, A. Fazzio, A. Zunger, Switching a Normal Insulator into a Topological Insulator via Electric Field with Application to Phosphorene, Nano letters 15, (2015) 1222–1228. https://doi.org/10.1021/nl5043769

[7] D. A. Bandurin, A.V.Tyurnina, L.Y. Geliang; et al., High electron mobility, quantum Hall effect and anomalous optical response in atomically thin InSe., Nat. Nano.,12, (2017), 223–227. https://doi.org/10.1038/nnano.2016.242

[8] B. Mortazavi, T. Rabczuk, Boron Monochalcogenides; Stable and Strong Two-Dimensional Wide Band-Gap Semiconductors, 11, (2018), 1573. https://doi.org/10.3390/en11061573

[9] P. Mishra. D. Singh, Y. Sonvane, R. Ahuja, Two-dimensional boron monochalcogenide monolayer for thermoelectric material, 4, (2020), 2363-2369. https://doi.org/10.1039/D0SE00004C

[10] G. Kresse, J. Furthmüller, Efficient iterative schemes for ab initio total-energy calculations using a plane-wave basis set, Phys. Rev. B, 54, (1996) 11169-11186. https://doi.org/10.1103/PhysRevB.54.11169

[11] J. P. Perdew, K. Burke, M. Ernzerhof, Generalized Gradient Approximation Made Simple, Phys. Rev. Lett., 77, 3865-3868. https://doi.org/10.1103/PhysRevLett.77.3865

[12] H.J. Monkhorst, J. D. Pack, Special points for Brillouin-zone integrations, Phys. Rev. B, 13, (1976), 5188-5192. https://doi.org/10.1103/PhysRevB.13.5188

[13] M. Gajdoš, K. Hummer, G. Kresse, J. Furthmüller, F. Bechstedt, Linear optical properties in the projector-augmented wave methodology, Phys. Rev. B, 73, (2006), 045112. https://doi.org/10.1103/PhysRevB.73.045112

[14] K. Momma and F. Izumi, VESTA 3 for three-dimensional visualization of crystal, volumetric and morphology data, J. Appl. Cryst. 44, (2011) 1272-1276. https://doi.org/10.1107/S0021889811038970

[15] D.Singh, S.K. Gupta, Y. Sonvane, I. Lukačević, Antimonene: a monolayer material for ultraviolet optical nanodevices, 4, (2016), 6386-6390. https://doi.org/10.1039/C6TC01913G

The Performance Study of CIGS Solar Cell by SCAPS-1D Simulator

Virang Shukla[1,a] [*], Gopal Panda[2,b]

[1]Department of Physics, Sarvepalli Radhakrishnan University, NH-12, Hoshangabad Road, Bhopal, India

[2]Department of Physics, Sarvepalli Radhakrishnan University, NH-12, Hoshangabad Road, Bhopal, India

[a]virangshukla_1983@yahoo.co.in, [b]gopal_panda007@yahoo.com

Keywords: Solar Cell, SCAPS-1D Simulator, CIGS Thickness, Band Gap, EBR

Abstract: The reference structure was simulated by SCAPS-1D simulator. The simulation result showed the effect of CIGS thickness, band gap and effect of EBR on the cell performance. From the simulation it could be seen that all parameters were sharply affected below CIGS thickness of 1000 nm due to increase of recombination velocity at back contact and poor absorption. Open circuit voltage was improved by CIGS thickness and band gap. Reference structure showed 18.78% efficiency after simulation with CIGS thickness of 3000 nm and band gap of 1.15 eV. The back electron reflector (EBR) had been inserted to reduce the effect of back contact recombination. With EBR cell performance was significantly improved. The proposed structure showed 19.30% efficiency with CIGS thickness of 1000 nm.

Introduction

CIGS are enrolled as an effective alternative to silicon technology. One of the important advantages based on CIGS is the reduction of material usage and thereby reducing cost of production. The past performance of CIGS was reported to 20.3% [26]; which is close to silicon whose performance is nearly 25%. For improving performance of CIGS solar cell it is desirable to understand the basic factors limiting the electrical parameters of the cell. The main aim of this work was to study the various parameters of CIGS solar cell. The simulation was done using SCAPS-1D simulator. Various parameters such as absorber layer thickness, band gap and effect of EBR were examined. The parameters were simulated using SCAPS-1D simulator and their influence on electrical parameters of CIGS solar cell was analyzed.
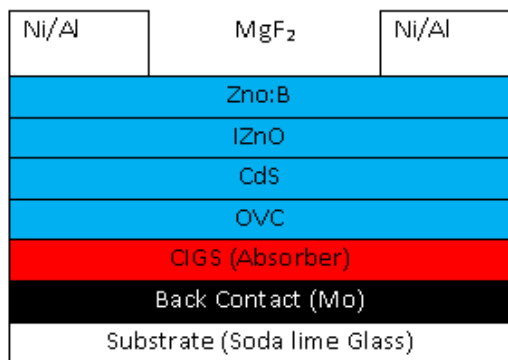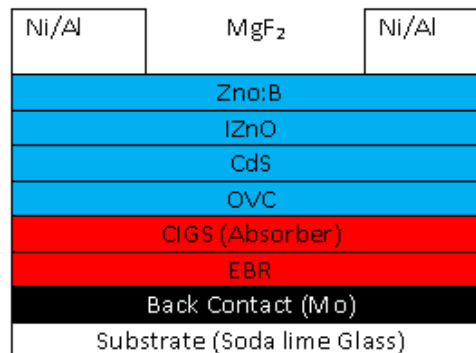

Figure 1(a) Reference Structure

Figure 1(b) Proposed Structure

Cell structure

The structure was simulated using SCAPS-1D simulator. The main part of the cell is CIGS absorber layer and CdS buffer layer. The thin layer OVC is formed between interface states of absorber layer and buffer layer. OVC is normally beneficial for CIGS because of shifting electrical junction from high recombination interface between absorber and buffer layer. As a result recombination rate is reduced [1]. ZnO intrinsic layer and Boron doped ZnO are deposited on the top of the buffer layer. These two layers are commonly considered as a Transparent conducting oxide (TCO). The major drawback of ZnO: Al is absorption loss which leads to decrease in quantum efficiency of CIGS solar cell near infrared region. Therefore Boron doped ZnO would be more beneficial of CIGS solar cell [2]. Transparent conducting oxide is protected with anti-reflected MgF_2 layer to increase the absorption of photons in the absorber layer.

Numerical modeling and parameters for simulation

Simulations can be used to provide the information to interpret measurements and to analyze the potential merits of cell structure. Different software such as SCAPS-1D[22], ASA[3], PC-1D[4], AMPS-1D[18] have been developed for describing the performances of thin film solar cells. SCAPS-1D is widely used simulation program for CdTe and CIGS based solar cells. Single level defect is introduced in each layer. To pin Fermi level at CIGS/OVC and OVC/CDS layer interface neutral defects were introduced at 0.6 eV below the conduction band. The effect of series and shunt resistance was not taken in to the consideration. Band discontinuity at the interfaces between different layers was considered small and avoided. The solar spectrum AM 1.5 was used for the numerical simulation. The temperature was set at 300K.The following parameters were used for numerical simulation.

Table 1. Layer Properties [28]

Parameters	EBR	CIGS	OVC	CdS	iZnO	ZnO:B
W (nm)	10	100-3000	30	50	200	400
E_g (e V)	1.4	Graded	1.3	2.4	3.3	3.3
X (e V)	4.5	4.5	4.5	4.45	4.55	4.55
$\varepsilon/\varepsilon_0$	13.6	13.6	13.6	10	9	9
N_c (cm^{-3})	2.2×10^{18}	2.2×10^{18}	2.2×10^{18}	1.3×10^{18}	3.1×10^{18}	3.0×10^{18}
N_v (cm^{-3})	1.8×10^{19}	1.5×10^{19}	1.5×10^{18}	9.1×10^{18}	1.8×10^{19}	1.8×10^{19}
v_e (cm/s)	10^7	3.9×10^7	3.9×10^7	3.1×10^7	2.4×10^7	2.4×10^7
v_h (cm/s)	10^7	1.4×10^7	1.4×10^7	1.6×10^7	1.3×10^7	1.3×10^7
μ_e	100	100	10	72	100	100
μ_h	25	12.5	1.50	20	31	31
Doping (cm^{-3})	2×10^{19}	5×10^{16}(A)	10^{13} (A)	5×10^{17}(D)	10^{17}(D)	10^{20} (D)

Table 2. Bulk defect Properties [28]

Parameters	EBR	CIGS	OVC	CdS	i ZnO	ZnO:B
N(cm^{-3})	10^{14}(D)	10^{14}(D)	10^{14}(D)	5×10^{16}(A)	10^{16}(A)	10^{16}(A)
ϖ_e (cm^2)	10^{-15}	10^{-15}	10^{-15}	10^{-15}	10^{-15}	10^{-15}
ϖ_h (cm^2)	10^{-11}	10^{-11}	10^{-11}	5×10^{-13}	5×10^{-13}	5×10^{-13}

Table 3. Properties of Interface [28]

Interface	CIGS/OVS	OVC/CDS
ΔE_C (e V)	0.6	0.6
N (cm^{-3})	10^{11} (N)	3×10^{13} (N)
ϖ_e (cm^2)	10^{-15}	10^{-15}
ϖ_h (cm^2)	10^{-15}	10^{-15}

Simulation analysis and result:

Effect of CIGS thickness on the performance of Solar cell

The thickness of CIGS was set at 3000nm. Other parameters were remained constant with variation of CIGS thickness. The CIGS band gap was kept constant at 1.15 e V. The figure (2) shows the influence of CIGS thickness on different electrical parameters of the cell. It could be observed from the result that there is a sudden reduction of all electrical parameters for reducing CIGS thickness below 1000 nm. The short circuit current density (Jsc) decreased abruptly by reducing CIGS thickness below 1000 nm. Recombination of photoelectrons at back contact was the reason of this. Photons having short wavelength deeply penetrate in to absorber layer and can create electron-hole pairs at back contact. In this zone recombination rate is very high. This may leads to lower the short circuit current density from 34.092197 mA /cm^2 to 25.463094 mA /cm^2 when CIGS thickness was reduced from 1000 nm to 100 nm.

For ultrathin thickness V_{OC} lesson due to reduction of the junction. The debase of Voc and Jsc drive to reduce efficiency of CIGS cell. The cell efficiency reduces from 16.93 % for 1000nm thickness of absorber layer to 8.93% for the thickness of 100 nm. The main reason behind this is only few photons are absorbed by absorber layer as the CIGS thickness reduces. As a result efficiency of solar cell reduced. All parameters of solar cell remained constant for CIGS thickness greater than 1000nm. The Jsc increased from the value 34.092197 mA/cm^2 to 36.734819 mA/cm^2 when CIGS thickness was increased from 1000 nm to 3000 nm. This leads to the cell efficiency from 16.93 % to 18.78 %. The quantum efficiency reaches 90% at CIGS thickness of 1000 nm. As the thickness was increased from 1000 nm more photons can be absorbed by absorber layer which can improve the cell performance.
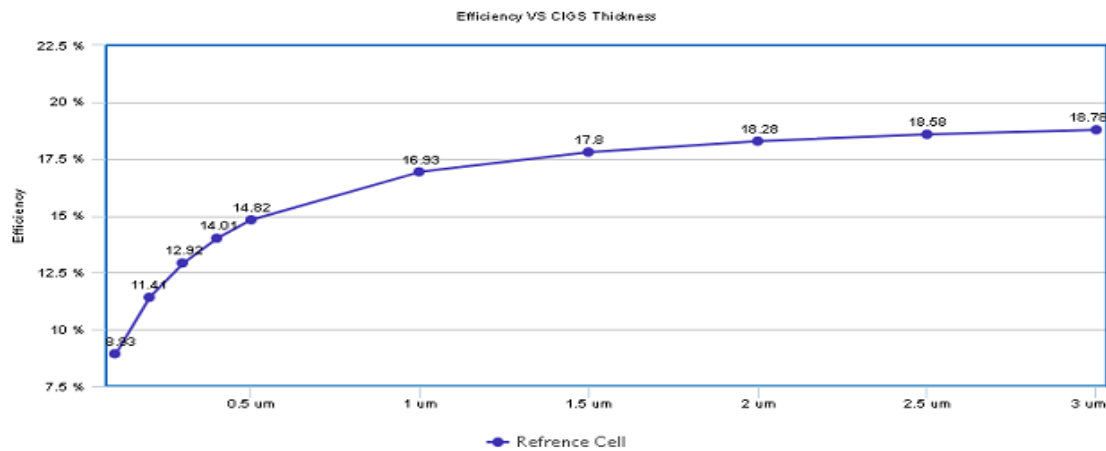

Figure 2 (a) Jsc VS CIGS thickness
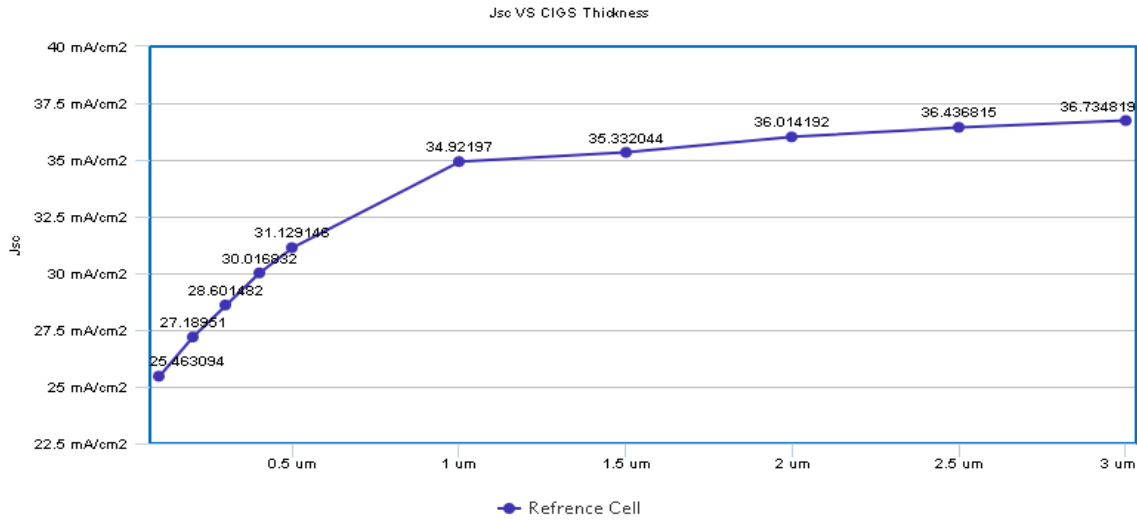
Figure 2 (b) Efficiency VS CIGS thickness

Grading effect on Performance of CIGS solar cell

CIGS band gap could be changed from 1 eV to 1.65 eV based on gallium proportion. The gallium dependency of band gap can be described by following equation.

E_g [eV] = 1.02 +0.67x + bx (x – 1) [8].

Where x denotes the gallium content in CIGS layer, x is the ratio of Ga / (Ga + In). The co efficient b is known as optical bowing coefficient. The band gap was assumed to be varied in accordance with gallium content in absorber layer. All parameters of CIGS layer and parameters of other layers were kept constant. From the simulation it could be seen that Voc increased with increase of band gap for Eg <1.25 eV. However the increment of Voc was not in proportional form with band gap. The relation of Voc was linear for band gap <1.25 eV(X<0.3).The relation became nonlinear for band gap having value >1.25 eV(X > 0.3). However open circuit voltage remains constant with high Ga concentration. This was mainly because of increment of   recombination rate in space charge region (SCR). From simulation result it could be seen that short circuit current density decreased sharply with increase of gallium content but strongly dependent on absorber layer thickness. For W < 1000 nm due to combined effect of increase in band gap and decrease in absorption coefficient decrement of Jsc was severe. The efficiency and fill factor increased with increase of band gap for Eg <1.25 eV. Above this value if band gap is increased by adding gallium concentration will decrease cell performance. These results seem to be good in comparison with experimental result obtained from different literature. The cell shows excellent efficiency with Eg = 1.15 eV (X = 0.3) [13]. From the study of Rau et al. [14] and Hanna et al. [9] it could be concluded that increment of band gap by adding Ga concentration can induce deformity in CIGS. These deformity gain degrade cell performance when band gap exceeds beyond 1.15 eV (X = 0.3). Figure (3) and Figure (4) shows variations of electrical parameters due to change in band gap.

Performance improvement with EBR:

The most affected parameter is short circuit current density by changing of CIGS thickness especially for ultrathin absorber (< 1000nm) as the electron is captured by back contact. Due to capture of electron at back contact Jsc reduces below 1000 nm thickness of absorber layer. With the help of ultrathin layer (EBR) between CIGS and Mo it would be possible to keep photo electrons away from interface. The back electron reflector can keep away electrons from CIGS/Mo

interface. As a result short circuit current density increases with increment of absorber layer thickness. Back electron reflector is able to increase all parameters of cell. The efficiency gain is about 2 % with EBR having thickness of 10 nm when absorber layer thickness is 1000 nm. The figure (5) shows gain in Jsc and efficiency due to different EBR thickness by varying the thickness of CIGS.
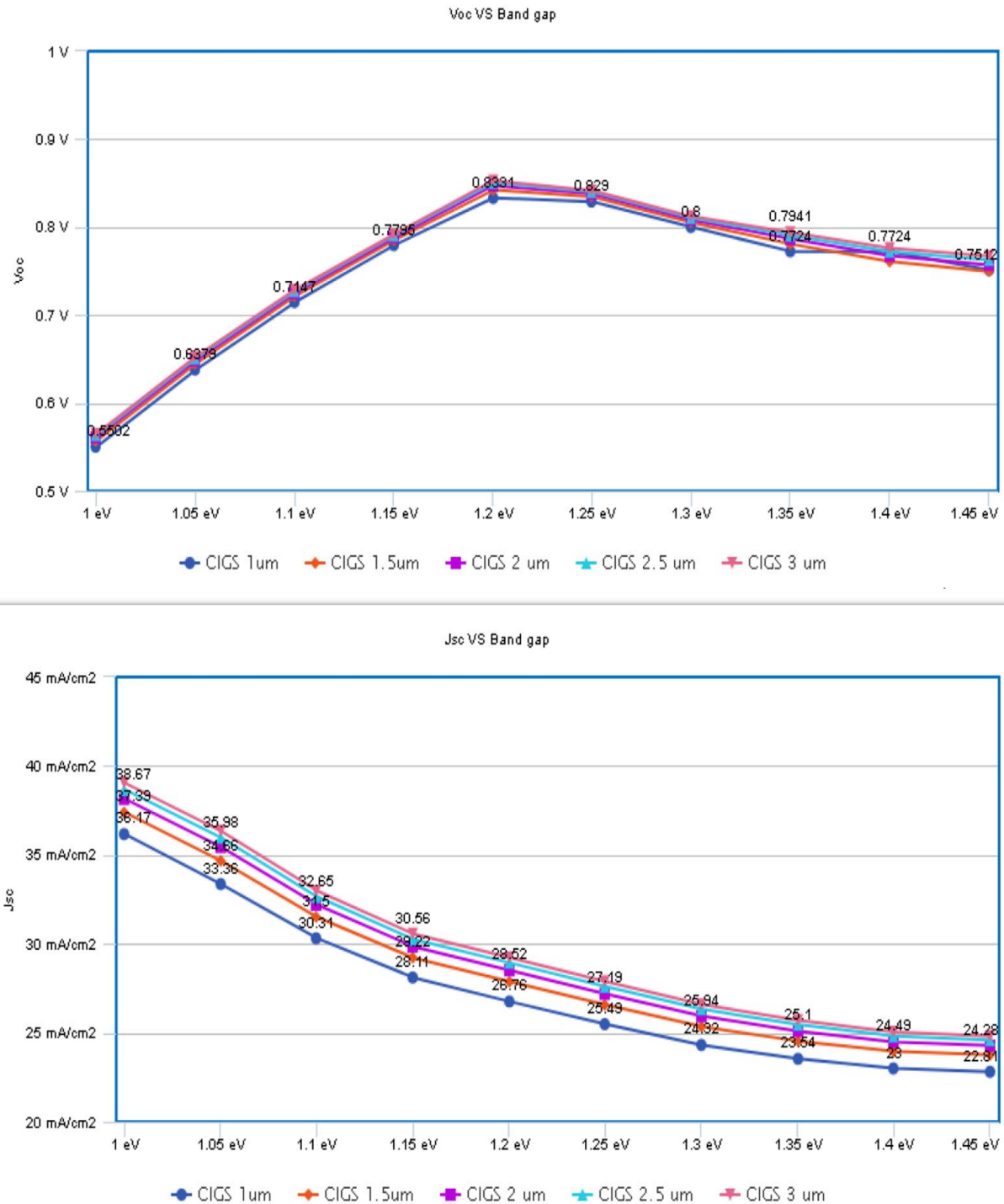

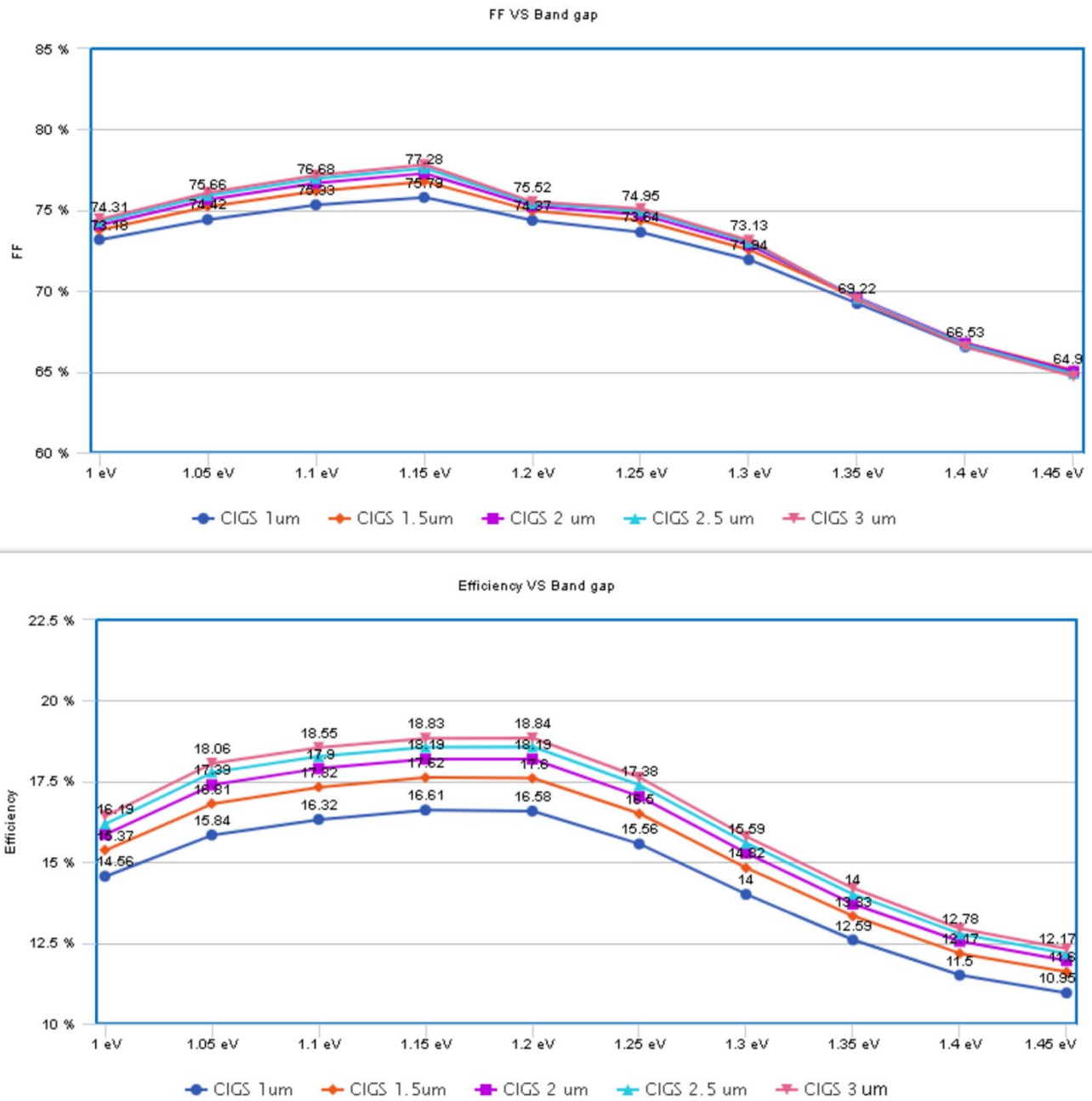*Figure 3. Effect of CIGS band gap on V_{oc} and J_{sc} by varying CIGS thickness*

Figure 4. Effect of CIGS band gap on Fill factor and Efficiency by varying CIGS thickness
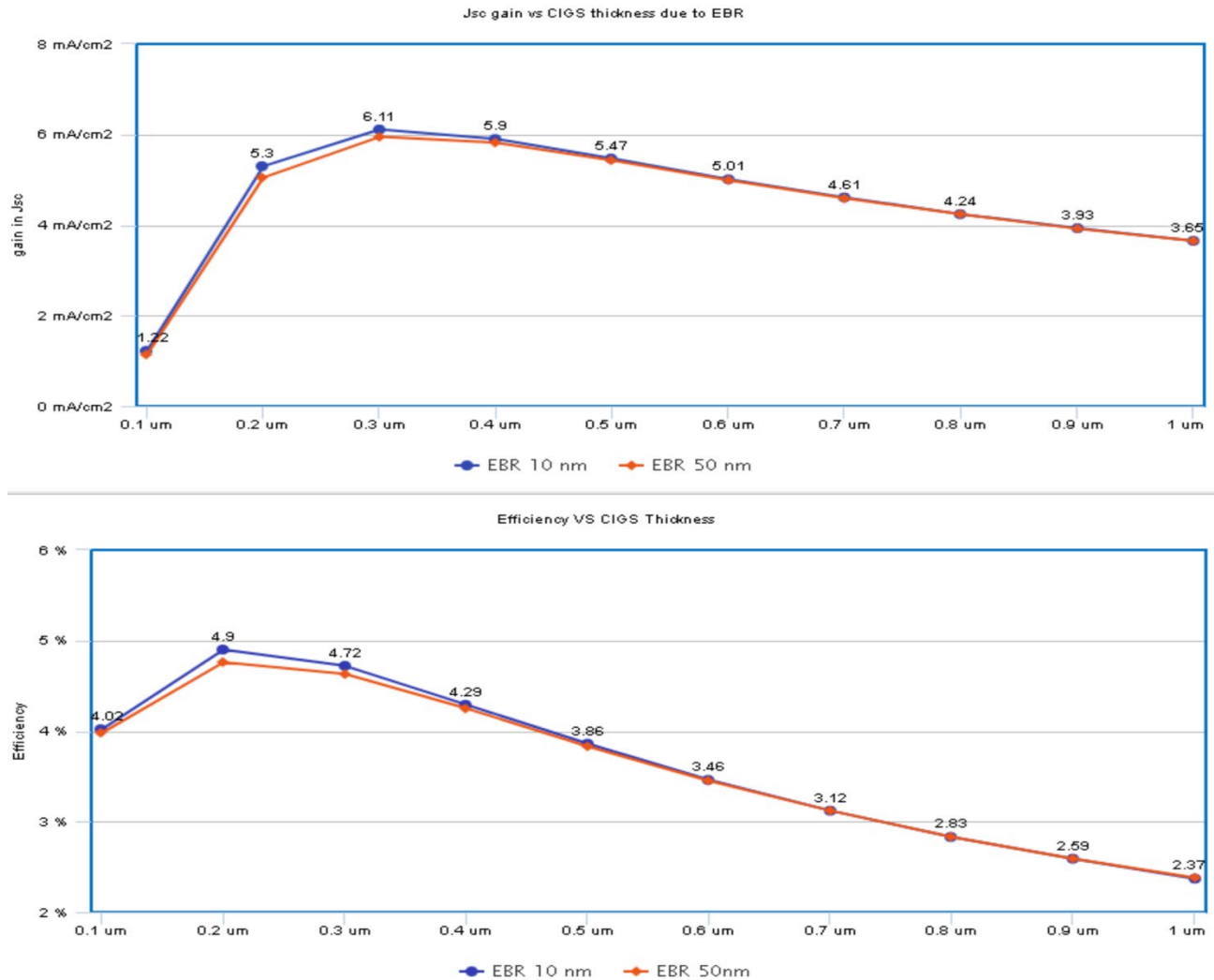
Figure 5. Gain in Jsc and Efficiency with back electron reflector by changing CIGS thickness

Conclusion

The thickness of CIGS layer, band gap and effect of EBR were analyzed using SCAPS-1D simulator. Following results could be obtained after simulation.

1. All parameters of cell are affected by varying CIGS thickness; short circuit current density degrades when thickness reduces from 1000 nm to 100 nm because of increment of recombination at CIGS/Mo interface.

2. The Ga grading can enhance solar cell performance. Jsc reduces drastically with increment of Ga in absorber. The relation between Voc and band gap is linear for E_g<1.25 eV. With increase in gallium concentration in absorber can enhance efficiency for E_g < 1.2 eV. Above this value increase in gallium concentration in absorber layer can reduce the cell efficiency. At E_g =1.15 cell shows the highest efficiency.

3. Back electron reflector can improve the cell performance. The efficiency is gained by 2 % with the presence of EBR with thickness of 10 nm when absorber layer thickness is 1000 nm.

Table 4. Performance parameters of Reference and Proposed cell

Parameters of cell	Reference cell	Cell with EBR (Proposed)
Thickness of CIGS (μm)	1.0	1.0
Open circuit voltage(V)	0.6567	0.6727
Jsc (mA /cm^2)	34.092197	37.746186
FF (%)	75.62	76.03
Efficiency (%)	16.93	19.30

Acknowledgements

References

[1] J. Song, S. S. Li, C. H. Huang, O. D. Crisalle, and T. J. Anderson, "Device modeling and simulation of the performance of Cu (In1−xGax)Se2 solar cells," *Solid-State Electronics*, vol. 48, no. 1, 2004, pp. 73–79. https://doi.org/10.1016/S0038-1101(03)00289-2

[2] Y. Hagiwara, T. Nakada, and A. Kunioka, "Improved J_{sc} in CIGS thin film solar cells using a transparent conducting ZnO:B window layer," *Solar Energy Materials and Solar Cells*, vol. 67, no. 1–4, 2001, pp. 267–271. https://doi.org/10.1016/S0927-0248(00)00291-9

[3] A. M. K. Dagamseh, B. Vet, P. Šutta, and M. Zeman, "Modelling and optimization of a-Si:H solar cells with ZnO:Al back reflector," *Solar Energy Materials and Solar Cells*, vol. 94, no. 12, 2010, pp. 2119–2123. https://doi.org/10.1016/j.solmat.2010.06.039

[4] P. A. Basore and D. A. Clugston, "PC1D version 4 for windows: from analysis to design," in *Proceedings of the 25th IEEE Photovoltaic Specialists Conference*, May 1996, pp. 377–381. https://doi.org/10.1109/PVSC.1996.564023

[5] M. Gloeckler, A. L. Fahrenbruch, and J. R. Sites, "Numerical modeling of CIGS and CdTe solar cells: setting the baseline," in *Procceddings of the 3rd World Conference on Photovoltaic Energy Conversion*, May 2003, pp. 491–494.

[6] O. Lundberg, M. Bodegård, J. Malmström, and L. Stolt, "Influence of the Cu(In, Ga)Se2 thickness and Ga grading on solar cell performance," *Progress in Photovoltaics*, vol. 11, no. 2, 2003, pp. 77–88. https://doi.org/10.1002/pip.462

[7] P. Chelvanathan, M. I. Hossain, and N. Amin, "Performance analysis of copper-indium-gallium-diselenide (CIGS) solar cells with various buffer layers by SCAPS," *Current Applied Physics*, vol. 10, no. 3, 2010, pp. S387–S391. https://doi.org/10.1016/j.cap.2010.02.018

[8] O. Lundberg, M. Edoff, and L. Stolt, "The effect of Ga-grading in CIGS thin film solar cells," *Thin Solid Films*, vol. 480-481, 2005, pp. 520–525. https://doi.org/10.1016/j.tsf.2004.11.080

[9] G. Hanna, A. Jasenek, U. Rau, and H. W. Schock, "Influence of the Ga-content on the bulk defect densities of Cu(In,Ga)Se$_2$," *Thin Solid Films*, vol. 387, no. 1-2, 2001, pp. 71–73. https://doi.org/10.1016/S0040-6090(00)01710-7

[10] T. Minemoto, T. Matsui, H. Takakura et al., "Theoretical analysis of the effect of conduction band offset of window/CIS layers on performance of CIS solar cells using device simulation," *Solar Energy Materials and Solar Cells*, vol. 67, no. 1–4, 2001, pp. 83–88. https://doi.org/10.1016/S0927-0248(00)00266-X

[11] C.-H. Huang, "Effects of Ga content on Cu(In,Ga)Se$_2$ solar cells studied by numerical modeling," *Journal of Physics and Chemistry of Solids*, vol. 69, no. 2-3, 2008, pp. 330–334. https://doi.org/10.1016/j.jpcs.2007.07.093

[12] R. Kniese, D. Hariskos, G. Voorwinden, U. Rau, and M. Powalla, "High band gap Cu(In,Ga)Se$_2$ solar cells and modules prepared with in-line co-evaporation," *Thin Solid Films*, vol. 431-432, 2003, pp. 543–547. https://doi.org/10.1016/S0040-6090(03)00260-8

[13] N. Amin, P. Chelvanathan, M. I. Hossain, and K. Sopian, "Numerical modelling of ultra thin Cu(In,Ga)Se$_2$ solar cells," in *Proceedings of the 6th International Conference on Materials for Advanced Technologies (ICMAT '11)*, July 2011, pp. 291–298. https://doi.org/10.1016/j.egypro.2012.02.034

[14] U. Rau, M. Schmidt, A. Jasenek, G. Hanna, and H. W. Schock, "Electrical characterization of Cu(In,Ga)Se$_2$ thin-film solar cells and the role of defects for the device performance," *Solar Energy Materials and Solar Cells*, vol. 67, no. 1–4, 2001, pp. 137–143. https://doi.org/10.1016/S0927-0248(00)00273-7

[15] Z. J. L. Kao, N. Naghavi, F. Erfurth et al., "Towards ultrathin copper indium gallium diselenide solar cells: Proof of concept study by chemical etching and gold back contact engineering," *Progress in Photovoltaics*, vol. 20, 2012, pp. 582–587. https://doi.org/10.1002/pip.2162

[16] A. Kanevce, Anticipated performance of Cu(In, Ga)Se$_2$ solar cells in the thin-film limit [Doctoral thesis], Colorado State University, (2007).

[17] S. Singh, S. Kumar, and N. Dwivedi, "Band gap optimization of p-i-n layers of a-Si:H by computer aided simulation for development of efficient solar cell," *Solar Energy*, vol. 86, no. 5, 2012, pp. 1470–1476. https://doi.org/10.1016/j.solener.2012.02.007

[18] N. Hernández-Como and A. Morales-Acevedo, "Simulation of hetero-junction silicon solar cells with AMPS-1D," *Solar Energy Materials and Solar Cells*, vol. 94, no. 1, 2010, pp. 62–67. https://doi.org/10.1016/j.solmat.2009.05.021

[19] A. Niemegeers, S. Gillis, and M. Burgelman, "A user program for realistic simulation of polycrystalline heterojunction solar cells: SCAPS-1D," in *Proceedings of the 2nd World Conference on Photovoltaic Energy Conversion*, Wien, July 1998.

[20] R. Scheer, "Towards an electronic model for CuIn1−xGaxSe2 solar cells," *Thin Solid Films*, vol. 519, no. 21, 2011, pp. 7472–7475. https://doi.org/10.1016/j.tsf.2011.01.092

[21] A. Bouloufa, K. Djessas, and A. Zegadi, "Numerical simulation of CulnxGa1−xSe2 solar cells by AMPS-1D," *Thin Solid Films*, vol. 515, no. 15, 2007, pp. 6285–6287. https://doi.org/10.1016/j.tsf.2006.12.110

[22] S. Degrave, M. Burgelman, and P. Nollet, "Modelling of polycrystalline thin film solar cells: new features in scaps version 2.3," in *Proceddings of the 3rd World Conference on Photovoltaic Energy Conversion*, May 2003, pp. 487–490.

[23] J. Pettersson, C. Platzer-Björkman, U. Zimmermann, and M. Edoff, "Baseline model of graded-absorber Cu(In,Ga)Se$_2$ solar cells applied to cells with Zn1−xMgxO buffer layers," *Thin Solid Films*, vol. 519, no.21, 2011, pp. 7476–7480. https://doi.org/10.1016/j.tsf.2010.12.141

[24] Z. Jehl, F. Erfurth, N. Naghavi et al., "Thinning of CIGS solar cells: part II: cell characterizations," *Thin Solid Films*, vol. 519, no. 21, 2011, pp. 7212–7215. https://doi.org/10.1016/j.tsf.2010.12.224

[25] M. Gloeckler and J. R. Sites, "Potential of sub micrometer thickness Cu (In,Ga) Se$_2$ solar cells," *Journal of Applied Physics*, vol. 98, no. 10, Article ID 103703, 2005, pp. 1–7. https://doi.org/10.1063/1.2128054

[26] P. Jackson, D. Hariskos, E. Lotter et al., "New world record efficiency for Cu(In,Ga)Se$_2$ thin-film solar cells beyond 20%," *Progress in Photovoltaics*, vol. 19, no. 7, 2011, pp. 894–897. https://doi.org/10.1002/pip.1078

[27] T. M. Razykov, C. S. Ferekides, D. Morel, E. Stefanakos, H. S. Ullal, and H. M. Upadhyaya, "Solar photovoltaic electricity: current status and future prospects," *Solar Energy*, vol. 85, no. 8, 2011, pp. 1580–1608. https://doi.org/10.1016/j.solener.2010.12.002

[28] S.ouedraogo,F.Zougmore,J.M.Ndjaka, "Numerical analysis of Copper-Indium-Gallium-Diselenide based solar cell by SCAPS-1D",International Journal of Photoenergy,vol.2013. https://doi.org/10.1155/2013/421076

Effect of Copper Phthalocyanine Interfacial Layer on the Performance of Mixed Halide Perovskite Solar Cells

K.L. Usha Kumary[1,a] *, M. Pratheek[2,b], T.A. Shahul Hameed[3,c] and P. Predeep[2,d]

[1] LBS Centre for Science and Technology, Trivandrum, 695033, India

[2] Laboratory for Molecular Electronics and Photonics, National Institute of Technology, Calicut, 673601, India

[3] Department of Electronics and Communication Engineering, TKM College of Engineering, Kollam, 691005, India

[a] ushakumarykl@gmail.com, [b] pratheekmekkat@gmail.com, [c] shahulhameed@tkmce.ac.in,
[d] ppredeep@gmail.com

Keywords: Hole Transport Layer, Mobility, Perovskite Solar Cell

Abstract. Organo metallic halide perovskite solar cells (PSCs) have attracted much attention due to the enhanced photovoltaic performance and wide absorption in the visible region. In this work, a perovskite solar cell device with mixed halide perovskite $CH_3NH_3PbI_{3-x}Cl_x$ as the active layer was fabricated in the normal device architecture and investigated. The effect of device performance was compared by introducing copper phthalocyanine (CuPc) as a hole transport layer (HTL). It is seen that device with a transport layer exhibits a better performance and power conversion efficiency (PCE) than the device without an HTL. The carrier mobility was determined using the space charge limited current (SCLC) method and found to be $0.0013 cm^2/Vs$.

Introduction

Perovskite solar cells (PSCs) have got considerable attention since 2009 when the first cell was reported with a conversion efficiency of 3.8% [1]. Following the pioneer work of Miyasaka et.al in organic-inorganic methyl ammonium lead halide perovskites, ease of preparation and solution processability makes it interesting for photovoltaic applications [2]. The real success happened in 2012 when the efficiency had reached up to 10% [3][4] and at present, the reported efficiency is about 21.6% [5]. Though the commercialisation demands high efficiency, long term stability and behaviour of suppressed hysteresis [6].

   PSCs make use of hybrid halide perovskite materials as the light absorbers and they possess crystal structure in the form ABX_3 where A and B are the cations. The cations A exist at the corners of the cubical structure and B in the middle of the octahedral sites set up by the X anions which exist in the middle of each face. The X consists of a halide and it can be fluorine, chlorine, bromine, iodine or a mixture of different halide atoms. Lead is the usually used small cation B. Tin can also be used, but it makes the structure less stable[7]. These small cations B together with the anions X form the inorganic part of the perovskite material. Methyl ammonium, ethyl ammonium or formamidinium constitute the organic part. The most investigated perovskite materials for photovoltaic applications are $CH_3NH_3PbI_3$ or the mixed halide $CH_3NH_3PbI_{3-x}Cl_x$ [8] due to their properties like intense wide band absorption, direct band gap, high carrier mobility and simple fabrication method [9]. The structures of the methyl ammonium halide [10] and copper phthalocyanine [11] are shown in Fig. 1.
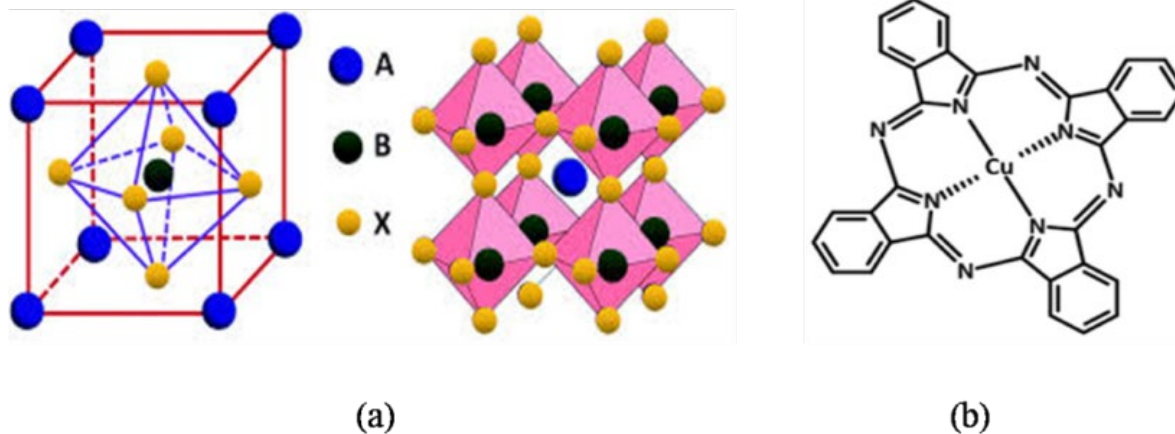
Fig. 1 Structures a) Organic-inorganic Methyl Ammonium Halide b) CuPc

Perovskite solar cell structures are generally classified into i) Inverted p-i-n and ii) Normal n-i-p structures [12] which are shown in Fig. 2.
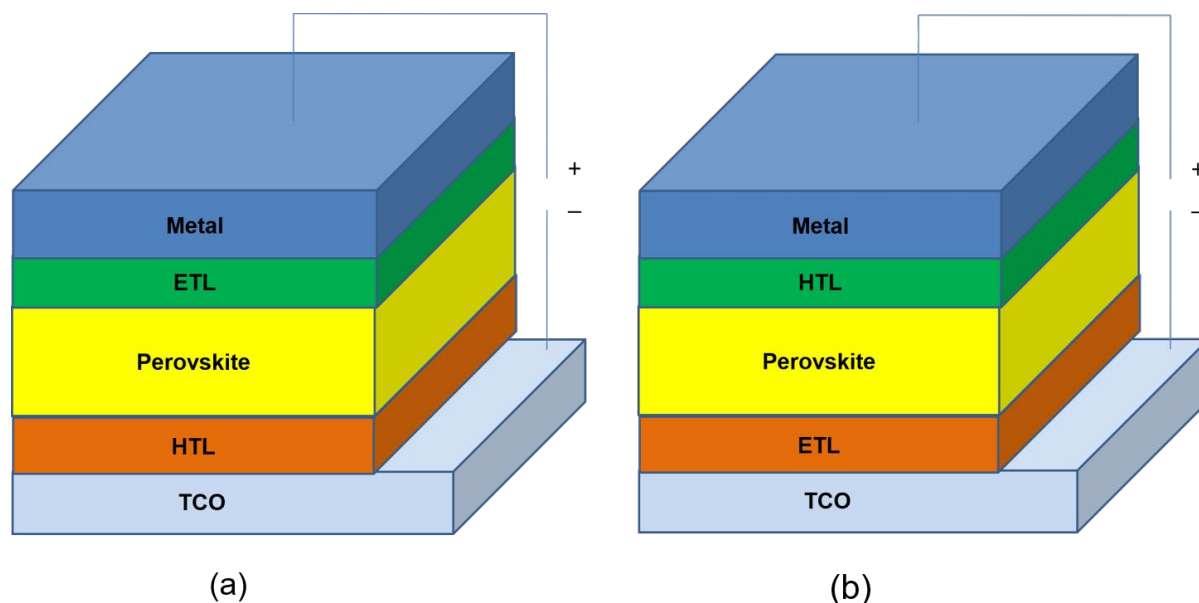

Fig. 2 (a) Inverse p-i-n and (b) Normal n-i-p

Device architecture consists of different layers. Indium tin oxide (ITO) or Fluorine doped tin oxide (FTO) substrate acts as the transparent conducting cathode. Electron transport layer (ETL) and hole transport layer (HTL) are used to extract and transport charge carriers to the respective electrodes and thus reduce the carrier recombination. The materials TiO_2, PCBM, ZnO and Al_2O_3 are commonly used as the ETL and Spiro-MeOTAD, PEDOT:PSS and CuI as HTL[12].

PSCs operate on the principle that when light incidents on the device, it reaches into the active layer through the transparent electrode and generates excitons which are dissociated easily into

charge carriers. The binding energy of excitons depends on the optical band gap and the perovskite material. Generated charge carriers have high diffusion length are transported through the transport layers and finally collected by the respective electrodes. In the PSC device with normal structure, electrons are collected by FTO which is the transparent electrode.

It can be understood that most of the hole transport layers introduced in the PSCs were of small molecular type. Copper phthalocyanine (CuPc) is a widely known small molecule metal organic compound that has been commonly used [13] in organic photovoltaic cells as HTL due to its properties such as excellent chemical and thermal stability, flexibility, high hole mobility and its semiconducting property [14]. It has also been introduced in the PSCs [15].

In normal perovskite architecture, HTL is coated on the top of the perovskite surface followed by a layer of a high work function metal as the anode. The HTL facilitates the transfer of holes to anode from the perovskite layer by providing proper band alignment. The highest occupied molecular orbital (HOMO) and the lowest unoccupied molecular orbital (LUMO) of the HTL should be greater or lower respectively than that of the perovskite material to provide necessary driving force for the charge transfer process. Certain hole transport materials (HTM) exhibit better performance depending upon the device configuration and the method by which it is fabricated. In normal architecture, if a solution processable HTL is used, it is better to choose HTMs which do not need protic or polar solvents that dissolve the perovskite material. However, the solvent of the HTM should have an affinity[8] towards the perovskite layer surface.

In this work, perovskite solar cell devices with and without an HTL layer (Copper Phthalocyanine) are fabricated with normal architecture. Carrier mobility is then estimated using space charge limited current (SCLC) method.

Experimental Details

Fluorine doped tin oxide FTO/TiO$_2$ coated glass with a dimension of size of 2.5cmx2.5cm from Solaronix was used for the PSC fabrication without any further cleaning. Here, TiO$_2$ layer acts as the scaffold for facilitating the perovskite coating. The perovskite film was prepared with CH$_3$NH$_3$PbI$_{3-x}$Cl$_x$ precursor ink purchased from Ossila. The ink was stirred for 2hrs. at 60°C and spin coated at 2000rpm for 30s onto the FTO/TiO$_2$ coated glass plate to form the absorbing layer and the film was annealed at 90ºC for 30mins. The CuPc HTL was deposited by thermal evaporation in the vacuum thermal evaporation coating setup at 10^{-5} torr base pressure to form a layer of 10nm thickness. As CuPc has a large π conjugated system, it is not easy to dissolve in commonly used organic solvents and therefore vapor deposition method was preferred to get the film. A quartz crystal was used to monitor the thickness. Finally, the anode Ag was evaporated through a shadow mask in the vacuum unit to form a layer of 100nm thickness.

The electrical characterization of the fabricated devices with the configurations FTO/TiO$_2$/perovskite/Ag and FTO/TiO$_2$/perovskite/CuPc/Ag were carried out by Keithley Sourcemeter and Solar Simulator at 100mW/cm^2.

Results and Discussion

The perovskite solar cell devices with and without CuPc hole transport layer are shown in Fig.3 and Fig. 4 respectively.
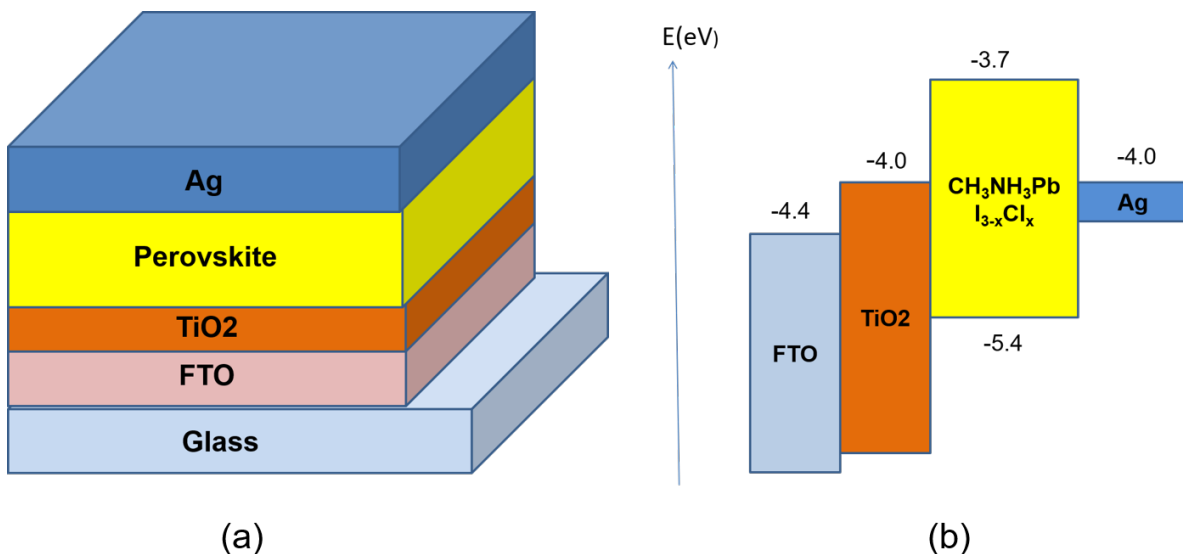
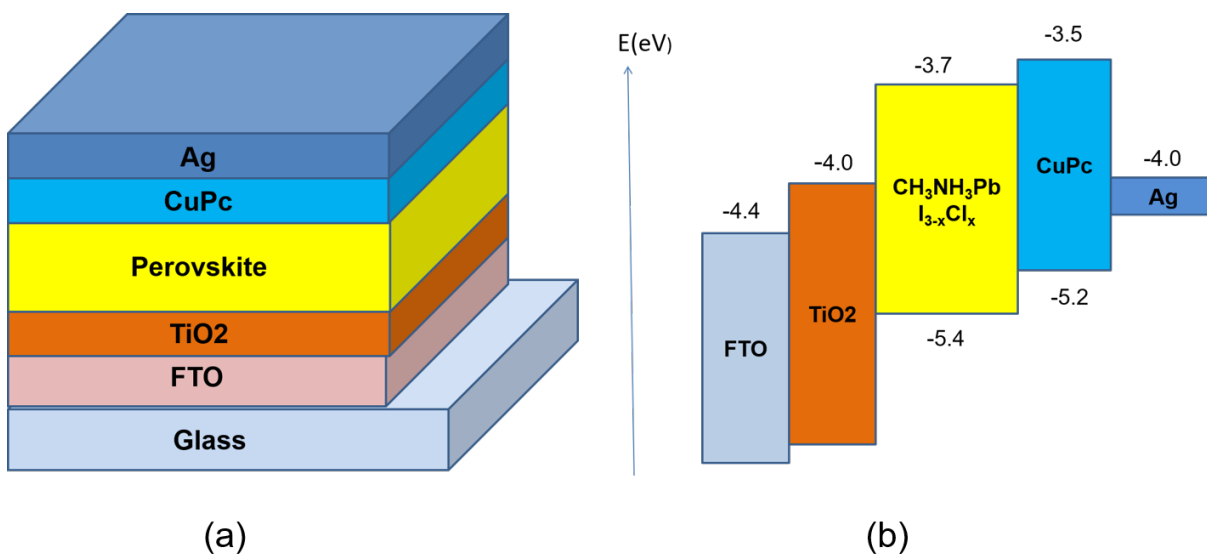*Fig. 3 (a)Perovskite device configuration and (b) Energy level schematic*

Fig. 4 (a) PSC structure with HTL (b) Energy level of each material

The energy level diagrams of the corresponding device structures are also presented. The working of the PSC depends upon the energy levels of the device layers. When incident light reaches the perovskite active layer $CH_3NH_3PbI_{3-X}Cl_x$, it excites electrons from HOMO to LUMO energy level by leaving holes in the HOMO energy level [12]. As in Fig. 3(b), the LUMO of $CH_3NH_3 PbI_{3-X}Cl_x$ is 3.7eV [15] and the work function of TiO_2 is nearly 4.0 eV, TiO_2 can easily collect the electrons. The copper phthalocyanine coated onto the top of the perovskite film (Fig.4(a)) helps to collect more photogenerated holes by the anode Ag [16]. The energy level of the subsequent layers must have to be matched for the effective functioning of the cell and also provide better contact between the layers.
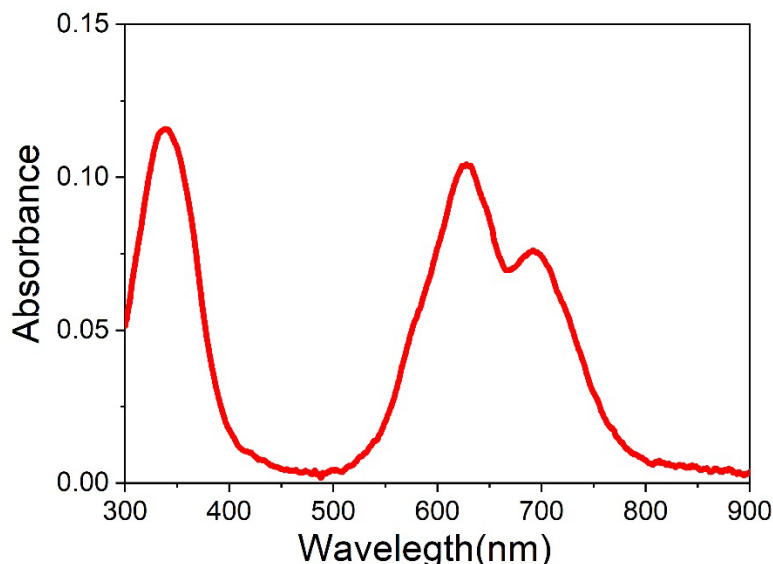
i)UV-Vis Absorption Characteristics

Fig. 5 Absorption spectrum

The optical absorbance spectrum of CuPc (Fig. 5) shows two absorption peaks at about 340nm (UV region) called Soret (B) band and at 625nm (visible region) called Q band. A small shoulder is seen at about 700nm. The Q band that is well known for the phthalocyanine molecule appears in between 550 and 750nm which is in the visible region. Generally, the distinct characteristic peaks in the visible spectral region are interpreted as π-π^* transition between bonding and antibonding molecular orbitals whereas that in the B band, are interpreted as the lowest allowed n-π^* excitation. It can also be noted that the band exhibits Davydov splitting [17] seen in all phthalocyanine derivatives. The high energy and low energy peaks available in the Q band correspond to the first and second π-π^* excitation[17].

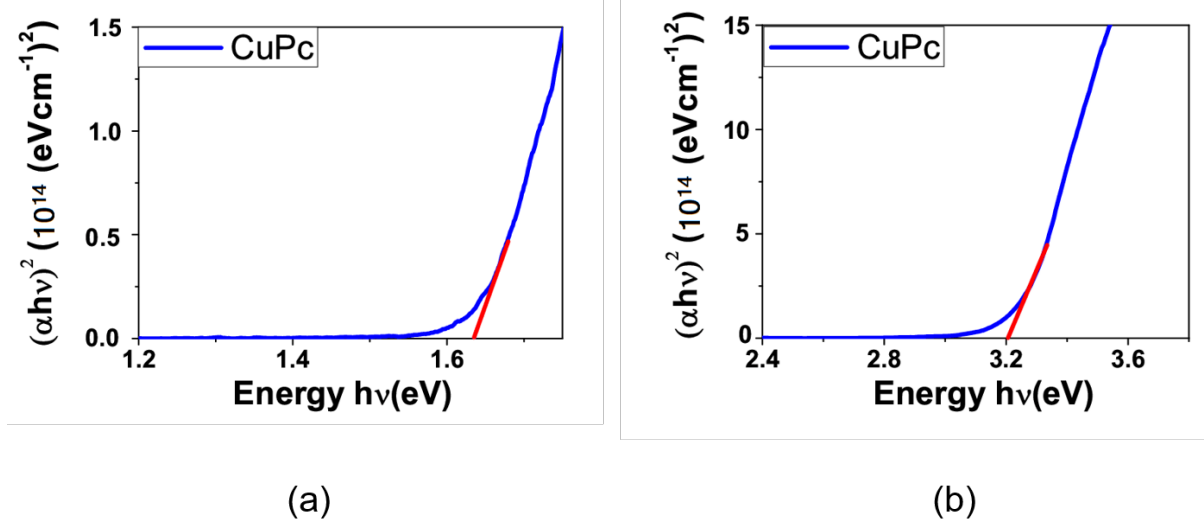(a)   (b)

Fig. 6 Tauc's plot for energy band gap calculation

The optical energy gap of CuPc is evaluated from its absorption spectrum near the fundamental absorption edges. In these regions, the incident photon energy hν is related to the absorption coefficient α as:

$$\alpha h\nu = B(h\nu - E_0)^m \tag{1}$$

where E_0 is the optical band gap, B is the transition probability which is constant within the optical frequency range and m is transition constant and has values m=0.5 for direct and 2 for indirect [18] transitions.

The characteristics of $(\alpha h\nu)^2$ versus hν near the Q and B band absorption edges are shown in Fig. 6. The optical band gaps CuPc is determined by extending tangent to zero absorption and are obtained as 1.63eV and 3.2eV.

ii)J-V Characteristics

Carrier mobility is one of the important characteristics of transporting material for effective carrier extraction and transport. The mobility is therefore calculated using the space charge limited current method from the dark characteristics (Fig.7(b). In the SCLC region, the J-V characteristics become quadratic where the current density depends on mobility rather than the carrier density [19] and therefore the carrier mobility can be evaluated using the relation:

$$J = \frac{9\mu\epsilon V^2}{8d^3} \tag{2}$$

The hole mobility in the device is obtained as 0.0013cm^2/Vs which is closer to the value reported [8].
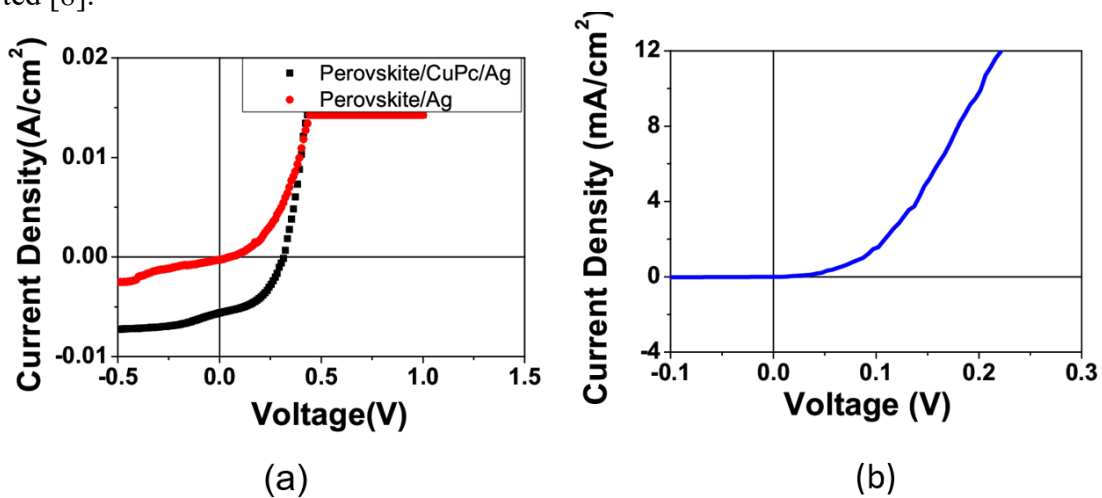

Fig. 7 J-V characteristics (a) illumination (b) dark

Under illumination the current-voltage characteristics of the PSC devices were obtained as in Fig.7(a) and the parameters determined for each cell were presented in Table 1. The device fabricated with CuPc as HTL with an active area of 7mm^2 returned open circuit voltage (V_{oc}) of 0.31V, short circuit current density (J_{sc}) of 6mA/cm^2 and fill factor of 46.11% which resulted in an efficiency of 0.8%. Even though the V_{oc} obtained is of greater with HTL, but it has not reached to the expected value as the HOMO level of CuPc is 5.2eV because the photovoltage of the device is decided by the difference in the quasi Fermi levels [13] of electron and hole conducting materials. The J_{sc} is improved due to the efficient extraction and transport of holes by the CuPc

layer. The higher the hole conductivity of the metal organic combination, the larger values of J_{sc} and FF. The fill factor is also improved due to the small value of series resistance Rs [20].

Table 1 Photovoltaic Parameters of the Perovskite solar cells

Device	V_{oc}	J_{sc}	FF	PCE	Rs	Rsh
	[V]	[mA/cm^2]	[%]	[%]	[Ω]	[Ω]
Without HTL	0.0225	0.2383	41.99	0.002	221.73	195.69
With CuPc as HTL	0.3130	6.0	46.11	0.80	13.76	204.92

The CuPc absorption spectrum shown in Fig. 5 is not preferably applicable for the normal architecture, but to the inverted one [8]. Usually, a portion of the light is reflected by the metal electrode to the perovskite layer and it can improve the device performance, but in the normal structure, the reflected light would get hold by the CuPc layer.

The PSC devices in this study were fabricated under ambient conditions and humidity. The readings were also taken under the same conditions without encapsulating the devices and this has resulted in uncharacteristically low values of efficiency recorded for the devices studied here. However, as the investigations intended objective is to comparatively study the effect of the CuPc HTL, this limitation may be ignored as the results provided valuable data and insight in achieving the intended objective.

Conclusions

The perovskite solar cell devices in normal architecture were constructed and tested with CuPc hole transport layer. The effect of CuPc was studied and observed that the device performance was enhanced with the introduction of HTL. The parameters J_{sc} and FF were improved due to the higher hole conductivity of the CuPc layer. The device fabrication was carried out under ambient conditions of high humidity, without using a glove box which account for the uncharacteristically poor performance of the devices. But the objective of the study has been accomplished as the results show a much high and unambiguous performance enhancement with CuPc as HTL compared with the device without any interfacial layer. The hole mobility was determined using SCLC method and it was obtained as 0.0013cm^2/Vs.

References

[1] A. Kojima, K. Teshima, Y. Shirai, T. Miyasaka, Organometal Halide Perovskites as Visible-Light Sensitizers for Photovoltaic Cells, J. Am. Chem. Soc. 131 (2009) 6050-6051. https://doi.org/10.1021/ja809598r

[2] H. J. Snaith, Perovskites : The Emergence of a New Era for Low-Cost , High-Efficiency Solar Cells, J. Phys. Chem. Lett. 4 (2013) 3623–3630. https://doi.org/10.1021/jz4020162

[3]   H. Kim, C. Lee, J. Im, K. Lee, T. Moehl, A. M Marchoro, S. Moon, R. H. Baker, J. Yum, J. E. Maser, M. Gratzel, N. Park, Lead iodide perovskite sensitised All-Solid-State Submicron Thin Film Mesoscopic solar cell with fficiency exceeding 9%, Sci. Rep. 2 (2012) 591-597. https://doi.org/10.1038/srep00591

[4]   M. M. Lee, J. Teuscher, T. Miyasaka, T. N. Murakami, H. J. Snaith, Efficient Hybrid Solar Cells based on Meso -Superstructured Organometal Halide Perovskites, Science 338 (2012) 643–648. https://doi.org/10.1126/science.1228604

[5]   D. S. Philips, W. Warmuth, Fraunhofer ISE: Photovoltaics Report, 2019.

[6]   Z. Wu, T. Song, B. Sun, Carbon-Based Materiala used for Perovskite Solar cell, ChenNanoMat 3 (2017) 75-88. https://doi.org/10.1002/cnma.201600312

[7]   M. A. Green, A. Ho-baillie, H. J. Snaith, The emergence of perovskite solar cells, 8 (2014) 506–514. https://doi.org/10.1038/nphoton.2014.134

[8]   A. Gheno, S. Vedraine, B. Ratier, J. Bouclé, π-Conjugated Materials as the Hole-Transporting Layer in Perovskite Solar Cells, Metals 6 (2016) 21–42. https://doi.org/10.3390/met6010021

[9]   W. Chen, Y. Wu, Y. Yue, J. Liu, W. Zhang, X. Yang, H. Chen, E. Bi, I. Ashraful, M. Gratzel, L. Han, Efficient and stable large-area perovskite solar cells with inorganic charge extraction layers, Science 350 (2015) 944–949. https://doi.org/10.1126/science.aad1015

[10] Z. Yi, H. Ladi, X. Shai, H. Li, Y. Shen, M. Wang, Will organic – inorganic hybrid halide lead perovskites be eliminated from optoelectronic Applications?, Nanoscale Adv. 1 (2019) 1276–1289. https://doi.org/10.1039/C8NA00416A

[11] M. Yokota, K. Fujii, M. Ishigo, K. Sasaki, H. Kato, N. Doki, Enabling Solution Growth of Insoluble Organic Materials in Common Solvents, Adv. Chem. Eng. Sci. 6 (2016) 82-86. https://doi.org/10.4236/aces.2016.62010

[12] A. Baron, Synthesis and Characterization of methyl ammonium lead tri halide Perovskite Compounds and their Applications in Photonic Devices, Ph. D, University of Basrah, 2019.

[13] X. Jiang, Z. Yu, J. Lai, Y. Zhang, N. Lei, D. Wang, L. Sun, Efficient perovskite solar cells employing a solution-processable copper phthalocyanine as a hole-transporting material, Sci. China 60 (2017) 423–430. https://doi.org/10.1007/s11426-016-0393-5

[14] J. Zaumseil, H. Sirringhaus, Electron and Ambipolar Transport in Organic Field-Effect Transistors, Chem. Rev. 107 (2007) 1296–1323. https://doi.org/10.1021/cr0501543

[15] C. V. Kumar, D. Georgia Sfyri Raptis, E. Stathatos, P. Lianos, Perovskite Solar Cell with Low cost Cu-Phtahlocyanne as Hole Transporting Layer, RSC Adv. 5 (2015) 3786–3791. https://doi.org/10.1039/C4RA14321C

[16] S. Pitchaiya, M. Natarajan, A. Santhanam, V. Asokan, A. Yuvapragasam, V. M. Ramakrishnan, S. E Palanisamy, S. Sundaram, D. Velayuthapillai, A review on the classification of organic/inorganic/carbonaceous hole transporting materials for perovskite solar cell application, Arab. J. Chem. 13 (2020) 2526-2557. https://doi.org/10.1016/j.arabjc.2018.06.006

[17] A. A. M. Farag, Optical absorption studies of copper phthalocyanine thin films, Opt. Laser Technol. 39 (2007) 728–732. https://doi.org/10.1016/j.optlastec.2006.03.011

[18] Z. U. Islam, M. Tahir, W.A. Syed, F. Aziz, F. Wahab, S. M. Said, M. R. Sarker, S. H. Md Ali, M. F. M Sabri, Fabrication and photovoltaic properties of organic solar cell based on zinc phthalocyanine, Energies 13 (2020) 962-975. https://doi.org/10.3390/en13040962

[19] K. L. Usha Kumary, M. Pratheek, T. A. Shahul Hameed, P. Predeep, Measurement of hole mobility in P3HT based photovoltaic cell using space charge limited current method, AIP Conf. Proc. 2162 (2019) 20142–20147. https://doi.org/10.1063/1.5130352

[20] J. Wang, Z. Wang, M. Li, C. Zhang, L. Jiang, K. Hu, Q. Ye, L. Liao, Doped Copper Phthalocyanine via an Aqueous Solution Process for Normal and Inverted Perovskite Solar Cells, Adv. Energy Mater. 8 (2018) 1701688- 1701696. https://doi.org/10.1002/aenm.201701688

Ionization Potentials of Nucleic Acid Intercalators

SATISH Desale[1,a] [*], YOGESH S. Sonawane[2,b], SUNIL R. Patil[3,c],
SNEHAL Sharma[3,d], GODAWARI Hedaoo[3,e] and NIRAJ Sinha[4,f]

[1]Department of Applied Sciences and Humanities, R.C. Patel Institute of Technology, Shirpur, MS 425405, India

[2]Zeal College of Engineering and Research, Pune, MS 411041, India

[3]Institue of Science, Nagpur, Civil Lines Nagpur, MS 440008, India

[4]Department of Mechanical Engineering, IIT Kanpur, Kanpur, UP 208016, India

[a]satishdesale@gmail.com, [b]dr.yss01@gmail.com, [c]phy.patil@iscnagpur.ac.in, [d]sharmasnehal108@gmail.com, [e]mp.hedaoogodawari@iscnagpur.ac.in, [f]nsinha@iitk.ac.in

Keywords: Nucleic Acid, Intercalator, Ionization Potentials, Density Functional Theory

Abstract. Nucleic acid based electronic devices have attracted particular interest over the past two decades due to its ability of long-range charge transport and self-assembly. The π-π interactions of the stacked bases are believed to be responsible for the long-range charge transport. The insertion of intercalators could alter electronic structure of the host nucleic acids which may influence the charge transport through the nucleic acid. The influence of intercalators on charge transport through the host nucleic acids largely depends on ionization potentials of the intercalators. Therefore, in this work we intend to determine vertical and adiabatic ionization potentials of the nucleic acid intercalators by using density functional theory calculations using Gaussian 16 package. We also explore the role of solvent and discuss the significance of ionization potential values in comparison with the ionization potential values of nucleic acid bases. Ionization Potential values of these intercalators range from 7.67 eV to 11.12 eV and 4.5 eV to 6.46 eV in vacuum and aqueous medium, respectively. Daunomycin is found to have lowest ionization potential value in vacuum as well as in aqueous medium. On the other hand, Proflavine (Anthraquinone) has highest ionization potential value in vacuum (aqueous medium). Non-planar intercalators exhibit distinct vertical and adiabatic ionization potential values and decrease drastically upon solvation.

Introduction

Nucleic acids have been found to conduct electrical current. This has led to an idea of nucleic acid, particularly deoxyribonucleic acid (DNA), based electronic devices. Therefore, it has attracted significant research interest over the past two decades. This is mainly due to DNA's ability of long-range charge transport and self-assembly. Apart from this, these devices offer biocompatibility [1] and the possibility of electronics beyond the limits of lithography [2]. The π-π interactions of the stacked bases are believed to be responsible for the long-range charge transport. Further understanding and control of electrical conductivity of a given DNA molecule would further expedite the engineering of DNA based electronic systems. As a result, prodigious efforts [3,4] are put into understanding the charge transport in DNA. Apart from this, the basic building blocks of DNA bases have distinct electronic properties such as ionization potential (IP). The distinct IP values of DNA bases and base pairs allows one to construct DNA based electronic barriers and wells [5,6].

However, the major hurdle for further advent in DNA based electronic devices is the floppiness of the DNA molecule [7]. Native DNA can exist in several different structural forms including A-form, B-form, and Z-form, and the specific structure depends on local environmental variables such as ion concentration, humidity, strain and pH. The coupling between bases in the duplex will change depending on the conformation of the DNA, and the structure can be changed in a variety of ways. For instance, a DNA duplex can be switched from B-form into A-form by dehydrating the duplex in an ethanol solution, and preliminary studies indicate a counter intuitive result in that A-form DNA has a ~10x higher conductance than B-form [3].

Intercalators such as Daunomycin [8] are the small molecules inserted between nucleic acid bases. Intercalation of such molecules in DNA leads to profound changes in the structure of the double helix. Therefore, intercalation in DNAs can introduce the measurable change in the electronic properties of the molecule [9]. This leads to an idea that intercalation in DNA can offer the requisite stability for its electronic applications and control on electronic behavior of DNA. The influence of intercalators on charge transport through the host DNAs will mainly depend on the IPs of the intercalators. Therefore, in this work we intend to determine vertical (IPV) and adiabatic ionization potentials (IPA) of the intercalators by using density functional theory (DFT). As these systems, intercalated DNA are often solvated. Therefore, we also explore the role of dielectric constant and discuss the significance of IP values in comparison with that of the DNA bases.

Computational Details

In this study, we determine IP values of four intercalators i.e, Daunomycin, Proflavine, Berberine and Anthraquinone using DFT calculations. All the structural optimizations are performed using micromechanics with universal force field (UFF) [10]. The DFT calculations with B3LYP functional and 6-31g(d,p) basis set are performed using Gaussian 16 package. The effect of aqueous medium is considered implicitly using asolvent in polarizable continuum model (PCM) model. Vertical ionization potential as well as adiabatic ionization potential values are determined. The IPA is determined by applying the following procedure. First, the total energies of a molecule with physiological charge E(G) and radical cation with additional +1 charge E(G+) are calculated. The ionization energy is then obtained by,

$$IPA = E(G+) - E(G) \tag{1}$$

Whereas, IPV is defined as,

$$IPV = E(G+*) - E(G) \tag{2}$$

where E(G+*) is the energy of structurally optimized ionic states of intercalators with +1 charge in addition to their physiological charge. Proflavine, Berberine and Daunomycin have physiological charge of +1, whereas Anthraquinone is neutral. The structures of intercalators are shown in Fig. 1.
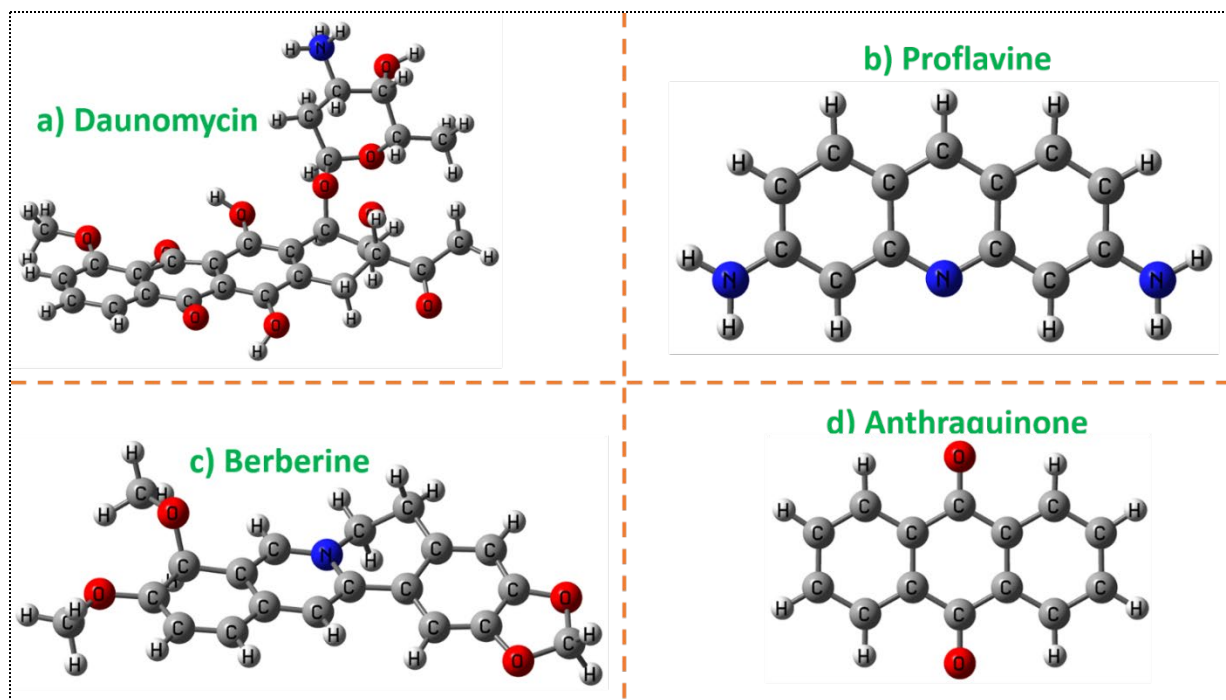
Fig. 1. Intercalating Molecules

Results and Discussions

The calculated values of IPA and IPV are presented in Table 1. We find that the IP values of these intercalators range from 7.673 eV to 11.123 eV in vacuum and in aqueous medium from 4.5 eV to 6.219 eV. Daunomycin has been found to have lowest IPA and IPV values in vacuum as well as in aqueous medium. On the other hand, Proflavine shows highest IP values in vacuum but Anthraquinone shows highest IP value in aqueous medium. We do not see major difference between IPA and IPV of these molecules (max 146 meV in vacuum and 127 meV in aqueous) as these are relatively smaller and largely planar molecules. The difference in IPA and IPV is almost negligible for completely planar molecules, i.e., Anthraquinone and Proflavine in vacuum. Although IP values of all the intercalators are influenced by consideration of aqueous medium, the major difference is in the non-planar molecules, Berberine and Daunomycin. We find that the values of IPA as well as IPV decrease substantially when aqueous medium is considered by means of changing dielectric constant of the molecule's surrounding. Higher dielectric constant of water screens the electrostatic interactions between the atoms. The screening is more effective for non-planar molecules. Therefore, IP values of non-planar molecules are significantly smaller than those of in vacuum. IP value of Anthraquinone is reported to be 9-9.40 eV[11], which is quite close to what has been obtained in this work, 8.726 eV in vacuum. To the best of our knowledge, this is the first study to report IP values of Berberine, Proflavine and Daunomycin.
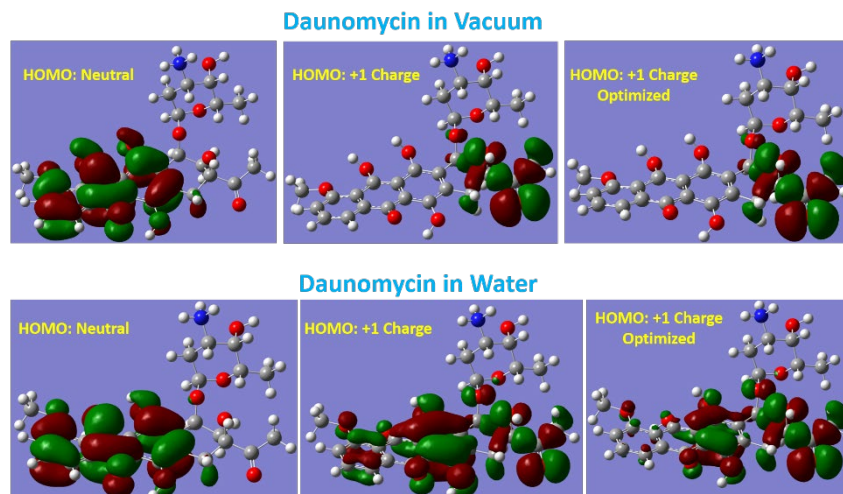
Fig. 1. HOMO Localization of Daunomycin in Vacuum and in Water Medium.

Range of IPV (in eV) of DNA and RNA bases, Uracil, Thymine, Cytosine, Adenine and Guanine, are 9.4-9.6, 9.0-9.2, 8.8-9.0, 8.3-8.5 and 8.0-8.3, respectively [12]. Therefore, all these intercalators in aqueous medium are expected to influence the charge transport when intercalated in DNA. It is most likely to assist the charge transport as the intercalators have IP values lower than DNA bases in aqueous medium. On the other hand, the intercalation may suppress the charge transport in vacuum.

Summary

In this work, we report vertical and adiabatic ionization potentials of four common intercalators, Anthraquinone, Berberine, Proflavine and Daunomycin, by using DFT calculations. To the best of our knowledge, this the first report on IP values of Berberine, Proflavine and Daunomycin. IP values of these intercalators vary over wider range, i.e. 7.673 eV to 11.123 eV in vacuum than in aqueous medium from 4.5 eV to 7.219 eV. Daunomycin is found to have lowest IP value in medium. Non-planar intercalators have distinct vertical and adiabatic ionization potential values and decrease drastically upon solvation. Planar intercalators have almost no influence on IP values and HOMO localization. The solvation decreases IP values of all the intercalators due electrostatic screening which also plays a major role in HOMO orbital localization. Smaller IP values of intercalators compared to nucleic acid bases in aqueous medium indicates that intercalators could significantly affect the charge transport in intercalated nucleic acids.

References

[1] Liedl, T., Sobey, T.L., and Simmel, F.C., DNA-based nanodevices, Nano Today, 2 (2) (2007)., 36–41. https://doi.org/10.1016/S1748-0132(07)70057-9

[2] Porath, D., Lapidot, N., and Gomez-Herrero, J., Charge Transport in DNA-based Devices, in Introducing Molecular Electronics (eds.Cuniberti, G., Richter, K., and Fagas, G.), Springer Berlin Heidelberg, Berlin, Heidelberg, (2005) pp. 411–444. https://doi.org/10.1007/3-540-31514-4_16

[3] Artés, J.M., Li, Y., Qi, J., Anantram, M.P., and Hihath, J., Conformational gating of DNA conductance. Nature Communications, 6 (2015), pp 8870. https://doi.org/10.1038/ncomms9870

[4] Li, Y., Artés, J.M., and Hihath, J., Long-Range Charge Transport in Adenine-Stacked RNA:DNA Hybrids. Small, 12 (4) (2016), pp432–437. https://doi.org/10.1002/smll.201502399

[5] Qi, J., Rabbani, M.G., Edirisinghe, S., and Anantram, M.P., Transport of charge in DNA heterostructures. 2011 11th IEEE International Conference on Nanotechnology, (2011) pp487–491. https://doi.org/10.1109/NANO.2011.6144620

[6] Patil, S.R., Chawda, V., Qi, J., Anantram, M.P., and Sinha, N., Charge transport through DNA based electronic barriers. AIP Conferene Proceedings, 1953 (1), (2018) pp140148. https://doi.org/10.1063/1.5033323

[7] Wang, H., Cheatham, T.E., Gannett, P.M., and Lewis, J.P., Differential electronic states observed during A--B DNA duplex conformational transitions. Soft Matter, 5 (3), (2009) 685–690. https://doi.org/10.1039/B800462E

[8] Wilhelm, M., Mukherjee, A., Bouvier, B., Zakrzewska, K., Hynes, J.T., and Lavery, R., Multistep Drug Intercalation: Molecular Dynamics and Free Energy Studies of the Binding of Daunomycin to DNA. Journal of American Chemical Society, 134 (20), (2012)   pp8588–8596. https://doi.org/10.1021/ja301649k

[9] Wang, X., Gao, L., Liang, B., Li, X., and Guo, X., Revealing the direct effect of individual intercalations on DNA conductance toward single-molecule electrical biodetection. Journal of Materials Chemistry B, 3 (26), (2015) pp5150–5154. https://doi.org/10.1039/C5TB00666J

[10] Rappé, A.K., Casewit, C.J., Colwell, K.S., Goddard III, W.A., and Skiff, W.M., UFF, a full periodic table force field for molecular mechanics and molecular dynamics simulations. Journal of American Chemical Society, 114 (25), (1992) pp10024–10035. https://doi.org/10.1021/ja00051a040

[11] https://www.chemeo.com/cid/45-405-2/9%2C10-Anthraquinone#ref-nist-webboo.k.

[12] Roca-Sanjuán, D., Rubio, M., Merchán, M., and Serrano-Andrés, L., Ab initio determination of the ionization potentials of DNA and RNA nucleobases. Journal of Chemical Physics, 125 (8), (2006) pp 84302. https://doi.org/10.1063/1.2336217

Recent Trends in Surface Cladding on AISI 1045 Steel Substrate: A Review

Md Sarfaraz Alam[1, a*], Anil Kumar Das[2, b]

[1,2] Department of Mechanical Engineering, National Institute of Technology Patna, Bihar, 800005, India

[a*]mda.phd19.me@nitp.ac.in; [b]akdas@nitp.ac.in

Abstract. This paper gives the informative review and enlighten the important characteristics and development of different cladding techniques applied on AISI 1045 medium carbon steel substrate material. The paper focuses on the cladding methods used on AISI 1045 steel follows the way of surfacing via fusion. The cladding practice like wire feed, powder blown are taken into consideration. Different cladding methods such as Tungsten Inert Gas (TIG) Arc cladding, thermal spraying, laser cladding and electron beam cladding has been compared for better understanding. The application of various cladding powders by TIG cladding technique on AISI 1045 steel substrate material is presented by exhaustive critical review of various research papers of the era. The importance of TIG cladding process has been discussed.

Introduction

AISI 1045 steel is one of the most usable medium carbon steels with excellent mechanical properties that is widely used in the automotive industry. Forging camshafts and cams needs material characteristics such as hardness, wear resistance, and higher strength. In order to achieve desirable microstructures and excellent mechanical properties, manufacturing conditions such as alloy content and cooling rate were changed in industrial practise. As technology progressed, the demand for better surface properties grew in popularity. There have been many advances that may be classified as "surface engineering." Coating, also known as cladding, is the process of creating a modified or new surface phase in a solid substrate [1–4]. Cladding is commonly used to improve properties near the surface while leaving core characteristics unchanged. [5-7]. Metals can be resurfaced using a melting process in which an intense energy source is used to fuse the substrate's surface as well as the reinforcing particles. [8]. When the reinforcing particles and base material solidify, this results in a tight metallurgical bond. Injection of powder, pre-place, powder surfacing or wire feed methods may all be used to apply reinforcement to the substrate material's surface. [9-11]. Several common techniques for surfacing AISI 1045 substrates have been investigated, including tungsten inert gas cladding [3,9,10,12–19], laser cladding [1,2,4,20–23], electron beam cladding [24,25], and thermal spraying [5,8,9,26–36]. The TIG cladding process uses an electric arc to generate a heat arc between the electrode (tungsten) and the substrate surface. Shielding gases like hydrogen, helium, argon, and a mixture of both helium and argon are used to protect the molten layer from contamination during the melting process. Following the solidification of the melted sheet, a new micro-structure with altered hardness and wear performance is created. Laser cladding is a non-conventional technique that involves fusing another material to the substrate surface. The process involves depositing coating material onto a substrate using a laser heat source. As a result, laser cladding (coating) emerges as an alternative surfacing technique. The technique can create coating layers with low dilution, better solid metallurgical bonding, and lesser distortion

with the substrate on a large variety of candidate materials [23, 24]. Low porosity and a homogeneous microstructure can be achieved using the laser cladding technique. Researchers suggested that the thickness of the film be monitored by adjusting the process parameters. In the electron beam cladding (EBC) process, a high velocity accelerated electrons is used to melt target metal. Thermionic emission occurs when cathode filament is heated in a negatively charged state, as a result electron are emitted. The beam of electrons bombarded into the surface of substrate at a speed of up to 0.7 times the speed of light. About 95% heat energy is generated by the kinetic energy of the electrons. The highest power density that could be achieved is 1010 Wm^{-2}. The electron beam has a diameter of between 0.3-0.8 mm. One of EBC's superior abilities is the ability to deep melt the surface layer due to its high-power density. This may be useful for coalescence of two metals, but the surface alteration does not need as much heat because the target focus is to reshape the top surface layer of the metal. [28] Another method known as thermal spraying that involves heating the coating material and depositing it on the substrate in individual particles. Sprayed reinforcing particles strike the ground, solidify, and form a laminar structure, resulting in a new/altered coating layer. [31-33].

Table 1: - Surface alteration approaches

Methods	Tungsten Inert Gas (TIG Arc) cladding	Electron beam (EB) cladding	Laser cladding (LC)	Thermal spraying (TS)
Fundamentals	A negatively charged tungsten electrode and positively charged metal substrate produces electric arc, hence heat is generated. Argon gas works as a shielding agent to prevent contamination and oxidation.	An electron beam is a high kinetic energy accelerated beam, when an electron beam is bombarded with a substrate material, the kinetic energy of the electrons is changed into heat, causes the fusion.	Laser cladding is an unconventional technique that involves melting one material to a substrate's surface. With a pre-set spot size, the laser beam is directed at the substrate. An inert gas transports the powder coating content into the melt pool using a nozzle	The cladding substance is sprayed on surface of substrate then heated. The sprayed particles collide with the surface of substrate, melting and solidifying to create a modified/new coating layer.
Advantages	There is no need for flux since inert gas shielding is used, so there is no inclusion or slag, high surface characteristics, ease of operation, lesser installation & maintenance costs, and a wider range of materials can be used. Less distortion is caused by small fires or sparks.	Since the process is carried out in vacuum, there is no scattering of electrons, and the surface quality is excellent, even on materials with higher thickness. Less distortion & shrinkage due to a more reliable and repeatable process, as well as a better regulated process.	Because of the concentrated heat source, coating can be accurately positioned, resulting in complete metallurgical bonding with low porosity and voids, high regularity, and a broader variety of products that are more energy efficient	The highest rate of deposition is up to 15 kg/h, and there is a wide variety of cladding materials that are easy to use and need little input power, and they can be used on heat sensitive substrates that need less heat, such as electronic components.

| Disadvantages | Rate of dilution is high. Because of the limited heat sources, it is not ideal for thicker materials or sluggish processes. | X-rays produced during the operation. Due to the limited size of the vacuum set-up, installation costs are high and are dependent on the vacuum chamber. | Due to random disruption in the system, sensitive process may lead to poor quality weld. Comparatively higher cost. | Higher oxide and porosity levels comparatively; hard to achieve thicker coating; high installation cost; more dust and fumes produced; therefore, health and safety issues; higher oxide & porosity comparatively. |

Surface cladding trends on AISI 1045

The material's surface property is critical for extending the existence of mechanical components. To achieve the surface alteration, ceramic particles were added to the matrix material's surface using different techniques to improve the material's surface properties. Surface composites are processed using molten phase processing at elevated temperatures. Matrix and the reinforcement form an interfacial reaction, and the chances of any harmful phases forming are strong. Ceramic particles were applied to the matrix surface and treated with TIG arc, EB irradiation, LC, and TS techniques in order to improve the material's surface characteristics. Areley et al. [1] used a 2.5 kW CO2 laser to deposit TiC on an AISI 1045 substrate. The existence of undissolved TiC particles was found to have increased the surface hardness. According to Wang et al. [3] TIG heating deposits coating layer of a mixture of powders containing (FeBrBSi, graphite and ferro-titanium on AISI 1045 steel. The findings revealed that during the TIG welding process, a metallic bonding of graphite and ferro-titanium and graphite can produce TiC grains. The cladded composite surface achieved has a significant improvement resistance against wear and micro-hardness because of development of titanium carbide grains. Similarly, Xinhong et al. [10] used a TIG process to deposit Fe-based self-fluxing, ferro-titanium, graphite and FeCrBSi powder to the substrate of C-45 steel grade, resulting in an in-situ system coating to manufacture an iron based composite surface with titanium carbide grains. TiC particles in the range of 3-5m were synthesised from graphite and ferrotitanium powder and uniformly spread in the matrix. TiC particles having higher hardness in the matrix enhanced the composite coating's hardness and wear resistance. On an AISI 1045 steel substrate, Zhao et al. [19] used tungsten inert gas cladding to deposit an in-situ synthesised $(Ti-Cr-Nb-Mo)_x C_y$ grains ceramic coating reinforcement. Closed packed grains, no cracks, and porosity characterise the coatings. The cladding's contact with the AISI 1045 steel substrate appeared to be seamless, reliable, and free of flaws. The substrate and the coating may have a strong metallurgical bond. Dark ceramic particles are mixed with a white Ni alloy binder to create the coating. Ceramic particle size and quantity vary from the root to the peak of the cladding grew in the proportion and amount in a gradient pattern. 5 times higher hardness value was achieved in comparison to AISI 1045 steel substrate. On an AISI 1045 steel substrate, Zhao et al. [18] used a TIG arc to create a cermet cladding layer based on (Ti, W) C. Close packed grains, no cracks, and porosity make up the cladding layers. Uniformity, continuous, and almost without defect cladding layer's is achieved at interface with the AISI 1045 steel substrate. It is possible to achieve fairly good metallurgical bond between the cermet and AISI 1045. Dark ceramic particles are bonded together by a white Ni alloy binder in the cladding layer. The peak

hardness of 1365 HV was obtained, nearly 600% harder than substrate. The cladded layers have excellent abrasion resistance. AISI 1045 steel substrate cladded by TIG arc with a placeable coating of ferro-titanium powder, the by the change in amount of nitrogen as shielding gas and their effects were studied by Hojjatzadeh et al. [12]. As the shielding gas's nitrogen content increases, an increment in penetration depth and area of cross section is observed in cladded surfaces. Two major microstructures emerged with the varying content of nitrogen: 1. Titanium-Nitride nano-structure spread in an alpha phase ferrite Fe_3C matrix is achieved with the increment of nitrogen, & 2. Ti (C_xN_y) in an alpha phase ferrite–Fe_2Ti matrix at a lower nitrogen content. In a crystal dissolved under pure argon, titanium carbide in a matrix of alpha ferrite, eutectic composition of alpha phase ferrite, and Fe2Ti was discovered. Tian et al. [29] used Fe-based cored wires as and spray device HAS-02, On the surface of AISI 1045 steel, FeNiCrAlBRE coatings were sprayed. The following were the wire arc spray system's parameters: The spray voltage is 30-34 V, the current is 14-160 A, pressure is 600 kPa (compressed air), and the gap is 200 millimetres. The arc sprayed FeNiCrAlBRE coatings undergo surface remelting, which results in a changed structure with reduced porosity, increased structure dispersion, and material homogenization, all of which led to improved wear resistance. Depending on how much heat was added to the coating after remelting, the Al_2O_3 form from an uneven block to a streamlined strip. Atoms diffused between both the layer of oxide and the surface matrix. There are no gaps or pores evident in the cladding layer after remelt. This layer has a smaller abraded volume, width, weight, and penetration than the spraying cladding. TIG is a popular and cost-effective method of improving the properties of arc-sprayed coatings. Tian et al. [30] produced as-sprayed coatings on AISI 1045 steel by using 2 mm diameter Fe–Ni–Cr–Al cored wire. The transformation Fe-Fe occurs as a result of the remelting treatment. Coated specimens have a much higher wear resistance than uncoated specimens. Separation of oxide into layers is the root cause of wear in sprayed coatings, according to thin flakes and energy dispersive spectroscopic analysis. The key abrasive wear mechanisms of remelted coatings are cutting and ploughing. Using cladding via laser and cladding by hybrid-laser induction, Zhou et al. [2] developed NiCrBSi powdered by 50% weight WC composite cladding on substrate of steel using LIHC. Prior to dry sliding wear, SEM and diffraction by X ray were used to investigate the micro-structure and phase constituents in composite coatings also XRD for wear. The height of cladding with LC was significantly more than LIHC with same laser processing conditions, while the heat affected zone, width of cladding, dilution, and efficiency of powder utilisation were significantly lower in LC. Sharifitabar [16] used a TIG coating process to coat AISI 1045 steel with Fe–TiC–Al_2O_3 coatings. Cladding precursors were $3TiO_2$-4Al-4.5C–1.71Fe. Using a TIG arc cladding process, substrate and mixture were melted together. The precursor was used to create a composite with 20 vol. percent reinforcing phases. Separately or on Al_2O_3 particles in a four-step process, in front of the molten pool, TiC is formed in Fe particles, when Fe grains enters molten pool, titanium carbide re-precipitated during solidification and TiC dissolution into the melt. Due to partially dissolution of few titanium carbide grains, TiC-Al_2O_3 territories formed in the cladded bead. Cladding micro-hardness improved and attained a maximum value 830 HV, increasing the resistance against abrasion of AISI 1045. Li et al. [35] are a group of researchers who came up with a novel approach an 800 μm thick coating layer was created spraying through plasma and arc remelting using on a steel substrate AISI 1045. Before and after TIG remelting, the NiCrBSi coating's microstructure and phase composition were investigated. The modulus of elasticity, fracture-toughness micro-hardness and resistance against wear of the material have all been tested. The results clearly show the improvement in the above-mentioned characteristics by the application of plasma sprayed and TIG remelting method. A

similar study is carried out by Li et al. [26] confirms the feasibility of this method and found to have an improvement in the dense Ni based plasma sprayed coating's microstructure and interfacial properties. Dong et al. [32] fabricated Ni based coating on a AISI 1045 steel grade by the method of plasma spray and TIG remelting. Results confirms the feasibility of TIG remelting for the coating and the microstructure of coated substrate enhanced with a significant improvement in corrosion resistance. Dong et al. [31] uses the methodology of coating with plasma spray and then remelting by TIG arc for the cladding layer of FeCrBSi on AISI 1045 steel, results shows that the feasibility of coating is very high and found to have a good characteristics of wear resistance. Yuan et al. [36] Used plasma sprayed coating then remelting of the layer by TIG arc technique for NiCr-Cr_3C_2 coating on a substrate made of AISI 1045 plate. The experiment was carried out to see how remelt by TIG affect the micro-structure and resistance against wear characteristics of NiCr-Cr_3C_2 coatings. Cladding of NiCr-Cr_3C_2 results in a significant improvement in microstructure, mechanical, and wear characteristics, as anticipated. Hao Liu et al. [23] and Jian Liu et al. [22]. The surface properties of AISI 1045 steel were improved by coating it with a high-entropy alloy (HEA), Al- CoCrFeNiTi. A good metallurgical bonding between coated alloy and substrate is achieved. As compared to substrate excellent wear and corrosion resistance shown by coatings. 4.5 times higher microhardness (865 HV) is achieved with respect to AISI 1045. Coating showed the best corrosion resistance. Jing Liu et al. [4] Deposited composite coatings of γ-Niss/Mo_2Ni_3Si on AISI 1045 plate by CO_2 laser (10.6 µm) wavelength. SEM with an attachment of EDS and XRD was used for phase constitution and microstructure study. Various mechanical properties e.g., microhardness, dry sliding wear behaviour and toughness of the coated plate were analysed. The result depicts that a much higher improvement in wear characteristics of coated alloy with respect to the substrate. Dong et al. [5] Coated NiCrBSiNb on a steel ring made of C 45 grade by the method of plasma spray and induction remelting. After coating microstructure were analysed, hardness test and wear test has been conducted. The result indicates that spray coating defects has been nullified almost and a great metallurgical bond between NiCrBSiNb and AISI 1045 was achieved. There is an efficient & significant improvement by the plasma sprayed coatings and induction heating for remelting in microstructure and wear resistance. Li et al. [27] Prepared NiCr-Cr_3C_2 cladding with plasma spray followed by remelting through tungsten inert gas arc on AISI 1045. A comparative study has been carried out before and after remelting of the NiCr-Cr_3C_2 coatings at different temperatures namely 25 ^{0}C, 200 ^{0}C, 400 ^{0}C, and 600 ^{0}C at each temperature microstructure, hardness and the wear test has been done. The outcome reveals that coating's internal structure appeared dense, there is a large reduction in defects. Also, there is an increase of 13.3% hardness on cladding surface after remelting and the surface was found to be uniform. The NiCr-Cr_3C_2 coating has been shown to greatly improve wear resistance, and the microstructure can be improved by tungsten inert gas arc remelting.

Summary and Future Outlook
In this review article a comprehensive review on surface modification through various surfacing methods is presented. The mechanical properties such as tensile strength, hardness & flexural strength is increased due to formation of intermetallic phases. The tribological, mechanical and corrosive properties of modified composite surface is improved due to uniform mixing of reinforcement particles with matrix. TIG arc method is a straightforward and movable method in comparison with conventional heat treatment methods hence, it is convenient method for altering the selective region.

References

[1] S. Ariely, J. Shen, M. Bamberger, F. Dausiger and H. Hugel, Laser surface alloying of steel with TiC. Surface and Coatings Technology, 45 (1991) 403-408. https://doi.org/10.1016/0257-8972(91)90249-V

[2] Shengfeng Zhou, Jianbo Lei, Xiaoqin Dai, Jinbo Guo, Zhenjie Gu, Hongbo Panc, A comparative study of the structure and wear resistance of NiCrBSi/50 wt.% WC composite coatings by laser cladding and laser induction hybrid cladding. Int. Journal of Refractory Metals and Hard Materials, 60 (2016) 17–27. https://doi.org/10.1016/j.ijrmhm.2016.06.019

[3] X.H. Wang, M. Zhang, Z.D. Zou, S.L. Song, F. Hanc, S.Y. Qu, In situ production of Fe–TiC surface composite coatings by tungsten-inert gas heat source Surface & Coatings Technology 200 (2006) 6117–6122. https://doi.org/10.1016/j.surfcoat.2005.09.021

[4] Jing Liu, Jian Zhang, Pengchuan Liu, Lijun Deng & Sen Zhang, Microstructure and wear behaviour of laser cladded γ-Ni$_{ss}$/Mo$_2$Ni$_3$Si coating. Surface Engineering Volume 36 (2020) - Issue 12: Special Issue: Laser. https://doi.org/10.1080/02670844.2019.1586301

[5] Dong, H, Surface engineering of light alloys: aluminum, magnesium and titanium alloys. Boca Raton, (2010) CRC Press. https://doi.org/10.1533/9781845699451

[6] S. Mridha and S. Dyuti, Wear Behavior of Modified Surface Layer Produced by TIG Melting of Preplaced Ti Powder in Nitrogen Environment. Advanced Material Research, 264–265, (2011) 1421–1426. https://doi.org/10.4028/www.scientific.net/AMR.264-265.1421

[7] K. A. Bello, M. A. Maleque, A. A. Adebisi and A. Dube, Preparation and characterization of TIG-alloyed hybrid composite coatings for high-temperature tribological applications. Int. J. Surf. Eng. Coatings, 94 (2016) 211–221. https://doi.org/10.1080/00202967.2016.1182727

[8] Karin Graf, Ana Sofia Clímaco Monteiro D'Oliveira, PTA hard facing of Nb/Al coatings. Technical Papers • Soldag. Insp, 17(2) (2012) 158-165. https://doi.org/10.1590/S0104-92242012000200009

[9] Li Ya-long, Dong Tian-shuna, Li Guo-lua, Wang Hai-doub, Fu Bin-Guoa, Zheng Xiao-donga, Zhou Xiu-kai, Microstructure and mechanical property of Ni-based thick coating remelted by gas tungsten arc. Vacuum, Volume 155 (2018) 260-269. https://doi.org/10.1016/j.vacuum.2018.05.053

[10] Wang Xinhong, Zou Zengda, Song Sili, Qu Shiyao, Microstructure and wear properties of in situ TiC/FeCrBSi composite coating prepared by gas tungsten arc welding. Wear 260 (2006) 705–710. https://doi.org/10.1016/j.wear.2005.03.018

[11] J. A. Folkes, Developments in Laser Surface Modification and Coating. Surface Coatings Technology, 63 (1994) 65–71. https://doi.org/10.1016/S0257-8972(05)80009-X

[12] S.M.H. Hojjatzadeha, A. Halvaeeb, M. Heydarzadeh Sohib, Surface alloying of AISI 1045 steel in a nitrogen environment using a gas tungsten arc process. Journal of Materials Processing Technology, 212 (2012) 2496– 2504. https://doi.org/10.1016/j.jmatprotec.2012.06.006

[13] Meng Junsheng, Ji Zesheng, Microstructure and Formation Mechanism of in-Situ TiN-TiB$_2$ /Ni Coating by Argon Arc Cladding. Rare Metal Materials and Engineering, 47(1) (2018) 0013-0019. https://doi.org/10.1016/S1875-5372(18)30064-X

[14] M. A. Malequea, W. Saffinab, A. S Ahmed and M. Y. Ali, Fe-C-Si ternary composite coating on CP-titanium and its tribological properties. IOP Conf. Series: Materials Science and Engineering, 184 (2017) 012013. https://doi.org/10.1088/1757-899X/184/1/012013

[15] Chinmaya Kumar Sahoo, Manoj Masanta, Microstructure and mechanical properties of TiC-Ni coating onAISI304 steel produced by TIG cladding process. Journal of Materials Processing Technology, 240 (2017) 126–137. https://doi.org/10.1016/j.jmatprotec.2016.09.018

[16] M. Sharifitabar, J. Vahdati Khaki, M. Haddad Sabzevar, M. Sharifitabar, J. Vahdati Khaki, M. Haddad Sabzevar M. Sharifitabar, J. Vahdati Khaki, M. Haddad Sabzevar, M. Sharifitabar, J. Vahdati Khaki, M. Haddad Sabzevar, Microstructure and wear resistance of in-situ TiC–Al2O3 particles reinforced Fe-based coatings produced by gas tungsten arc cladding. Surface & Coatings Technology, 285 (2016) 47–56. https://doi.org/10.1016/j.surfcoat.2015.11.019

[17] X.H. Wang, S.L. Song, Z.D. Zou, S.Y. Qu, Fabricating TiC particles reinforced Fe-based composite coatings produced by GTAW multi-layers melting process. Materials Science and Engineering A, 441 (2006) 60–67. https://doi.org/10.1016/j.msea.2006.06.015

[18] Li-ping Zhao, Zong-de Liu and Bin Li, Microstructure and Grain Abrasion Properties of (Ti,W)C-Ni Cermet Cladding Layers Prepared by Tungsten Inert Gas Cladding. Applied Mechanics and Materials, Vols. 80-81 (2011)133-136. https://doi.org/10.4028/www.scientific.net/AMM.80-81.133

[19] Li-ping Zhao, Zong-de Liu, and Bin Li, Microstructure and Properties of in-situ Synthesized Composite Coating by tungsten inert gas Cladding. Advanced Materials Research, Vols. 314-316 (2011) 296-299. https://doi.org/10.4028/www.scientific.net/AMR.314-316.296

[20] R. Colaço, T. Carvalho, R. Vilar, Laser Cladding of Stellite 6 on Steel Substrates. High Temperature Chemical Processes, 3 (1994) 21-29.

[21] Ruifeng Li, Yajuan Jin, Zhuguo Li, and Kai Qi, A Comparative Study of High-Power Diode Laser and CO_2 Laser Surface Hardening of AISI 1045 Steel. Journal of Materials Engineering and Performance, 23 (2014) 3085–3091. https://doi.org/10.1007/s11665-014-1146-x

[22] Jian Liu, Hao Liu, Peijian Chen, Jingbin Hao, Microstructural characterization and corrosion behaviour of AlCoCrFeNiTix high-entropy alloy coatings fabricated by laser cladding. Surface & Coatings Technology, 361 (2019) 63–74. https://doi.org/10.1016/j.surfcoat.2019.01.044

[23] Hao Liu, Jian Liu, Peijian Chen, Haifeng Yang, Jingbin Hao, and Xianhua Tian, Microstructure and Properties of AlCoCrFeNiTi High-Entropy Alloy Coating on AISI1045 Steel Fabricated by Laser Cladding. Journal of Materials Engineering and Performance, 28, (2019) 1544–1552. https://doi.org/10.1007/s11665-019-03949-9

[24] T. J. Lienert, E. D. Brandon and J. C. Lippold, Laser and electron beam welding of SiCp reinforced aluminum A-356 metal matrix composite. Scripta Materialia, 28 (1993) 1341–1346. https://doi.org/10.1016/0956-716X(93)90479-C

[25] K. Peng, H. Cui, F. Lu, X. Wu, X. Tang, S. Yao and S. Lou, Mechanical properties and wear resistance of aluminum composite welded by electron beam. Trans. Nonferrous Met. Soc. China, 21 (2011) 1925–1931. https://doi.org/10.1016/S1003-6326(11)60951-5

[26] Li Guo-lu, Li Ya-long, Dong Tian-shun, Fu Bin-Guo, Wang Hai-dou, Zheng Xiao-dong, Zhou Xiu-kai, Microstructure and interface characteristics of NiCrBSi thick coating remelted by TIG Process. Vacuum, 156 (2018) 440-448. https://doi.org/10.1016/j.vacuum.2018.07.020

[27] Li Guo-lu, Yuan Jing-min, Dong Tian-shun, Zhao Xiang-wei, Fu Bin-guo, and Shi Jiadong, Wear Resistance under Different Temperatures of NiCr-Cr3C2 Coating Remelted by Tungsten Inert Gas Arc. Journal of Materials Engineering and Performance, 29 (2020) 8013–8024. https://doi.org/10.1007/s11665-020-05254-2

[28] Guo-lu Li, Ya-long Li, Tian-shun Dong, Hai-dou Wang, Xiao-dong Zheng and Xiu-kai Zhou, Microstructure and Wear Resistance of TIG Remelted NiCrBSi Thick Coatings Advances in Materials Science and Engineering, special issue, (2018) 1-10. https://doi.org/10.1155/2018/8979678

[29] H.L. Tian, S.C.Wei, Y.X. Chen, H. Tong, Y. Liu, B.S. Xu, Surface remelting treated high velocity arc sprayed FeNiCrAlBRE coating by Tungsten Inert Gas. Physics Procedia, 50 (2013) 322 – 327. https://doi.org/10.1016/j.phpro.2013.11.051

[30] H. L. Tian, S. C. Wei, Y. X. Chen, H. Tong, Y. Liu, B. S. Xu, Microstructure and Wear Resistance of an Arc-Sprayed Fe-Based Coating After Surface Remelting Treatment. Strength of Materials, 46(2) (2014) 229-234. https://doi.org/10.1007/s11223-014-9540-z

[31] Dong Tianshun, Zheng Xiaodong, Li Yalong, Li Guolu, Zhou Xiukai, and Wang Haidou, Microstructure and Wear Resistance of FeCrBSi Plasma-Sprayed Coating Remelted by Gas Tungsten Arc Welding Process. Journal of Materials Engineering and Performance, 27 (2018) 4069–4076. https://doi.org/10.1007/s11665-018-3475-7

[32] Dong Tianshun, Zhou Xiu kai, Li Guolu, Liu Li and Wang Ran, Microstructure and corrosive wear resistance of plasma sprayed Ni-based coatings after TIG remelting. Mater. Res. Express, volume 5 Number 02 (2018). https://doi.org/10.1088/2053-1591/aaadd7

[33] M. M. Verdian, M. Salehi and K. Raeissi, Microstructure formation and properties of HVOF sprayed NiTi coatings prepared from amorphous/nanocrystalline NiTi powders. Surface Engineering, 26(2) (2010) 491-496. https://doi.org/10.1179/026708410X12593178265823

[34] M.M. Verdian, K. Raeissi, M. Salehi, Electrochemical impedance spectroscopy of HVOF-sprayed NiTi intermetallic coatings deposited on AISI 1045 steel. Journal of Alloys and Compounds, 507 (2010) 42–46. https://doi.org/10.1016/j.jallcom.2010.07.132

[35] Li Ya-long, Dong Tian-shun, Li Guo-lu, Wang Hai-dou, Fu Bin-Guo, Zheng Xiao-dong, Microstructure evolution and properties of NiCrBSi thick coating remelted by gas tungsten arc. Surface and Coatings Technology, 349 (2018) 260-271. https://doi.org/10.1016/j.surfcoat.2018.05.064

[36] Jing-min Yuan, Tian-shun Dong, Bin-guo Fu, Guo-lu Li, Li Liu, and Ran Wang, Effect of Tungsten Inert Gas Arc Remelting on Microstructure and Wear Properties of Plasma-Sprayed NiCr-Cr3C2 Coating. Journal of Materials Engineering and Performance, 28 (2019) 6320-6329. https://doi.org/10.1007/s11665-019-04350-2

Exploiting Reducing Ability of DMF for Assembled Gold Nanostructures

Hitesh Rajput[1,2,a,] Abhitosh Kedia[1, b,] Dimple Shah[2,] Neha Sharma[1]

[1]Department of Physics, Uka Tarsadia University, Bardoli, Surat-394350, Gujarat, India

[2]Applied Physics Department, SVNIT, Surat, Gujarat, India.

[a]hiteshrajpute@gmail.com; [b]abhitosh.kedia@utu.ac.in

Abstract. We explore stable assembly of gold NPs in single step process by introducing a simple chemical synthesis in which pH changed gold precursor is added to dimethylformamide solution at RT. The redox chemistry of N, N-dimethylformamide (DMF) has been effectively utilized in the formation of surfactant free, small chain metal NPs networks (plasmonic oligomers) via molecular dipolar coupling. Kinetic absorption / TEM images illustrate gold nanocrystals formation, their inter-particle coupling as a function of pH as well as with DMF-Water ratio. Sub-nano gap inter-particle coupling b/w spherical/anisotropic Au NPs is seen through arising of new LSPR hump in NIR region. 1-D organized gold nanocrystals are formed when pH modified metal precursor is added to refluxed (80 0C) DMF: Water mixture. The inter-particle coupling provides unique strategy can promote complex sub-wavelength optical waveguides and nanophotonic devices.

Introduction

The formation of arrays of highly anisotropic 1D nanoparticles and their associated collective vector properties are of particular interest to nanoelectronics, optoelectronics, nanomagnetic and sensing devices biology [1]. The formation of chains resembling metal nanoparticles was prepared by physical confinement in grooves etched by ion beams in glass. [2] or porous anodic alumina, [3] and using a linear macromolecular or supramolecular matrix. Alternatively, a 1D matrix can be generated, in the absence of a model, by spontaneous self-assembly of isoelectric nanoparticles with intrinsic magnetic or electrical dipoles. In the second case, the linear assembly is induced by partial removal of the organic stable shell, which increases the electric dipole interactions between the particles. Metal nanoparticle chains have also been reported, [4-7] although the origin of the putative dipole interactions and chain assembly mechanism remains unknown. Unlike semiconductor quantum dots, face-centered cubic (fcc) metal nanoparticles have no intrinsic electrical dipole. However, surface charge and polarity heterogeneity, e.g. with heterogeneous spatial distribution of ligands limited on different crystal faces, [7-9] or with separation of nanophases in stable layers of mixed ligands, [10] is possible. motivation for anisotropic self-assembly.

Herein, redox chemistry of N, N-dimethylformamide (DMF) has been effectively utilized in the formation of surfactant free, small chain metal NPs networks via molecular dipolar coupling. This uniquely versatile and powerful chemical has been used as a solvent in a wide variety of synthetic procedures. In contrast to aqueous solution [11] where a reducing agent [12] is needed for initiating the nanoparticles [13] formation, DMF can itself reduce gold and silver ions partially or completely. The potentiality of reducing ability of DMF [14] for preparation of metal nanoclusters [15-17] is reported but with external energy sources [18]. The mechanism of the formation of metal

nanoparticles using the reducing power of DMF still remains a subject of controversy as literature reports predict that reeducation by DMF release CO2 or carbonic acid [19] with dimethylamine [20] at room temperature, which doesn't have any detectable spectroscopic evidence [21-24]. Although the formation of Au nanoparticles [25] in DMF has already been reported, it seems to require catalysis by either poly(vinylpyrrolidone) [26,27] or by the metal seeds themselves. since Au seeds or PVP form complexes [28] with DMF molecules, they would strip off electrons from such complexed solvent molecules and act as catalysis. The important role played by DMF as a solvent and reaction medium in the formation of metal nanoparticles has motivated us in growth kinetics of metal NPs formation. We have pioneered the use of organic solvent which itself can serve as reducing agent as well as supporting medium and efficient formation of assembled gold nanostructures may not require the introduction of additional reducing agent unlike in conventional chemical methods [29]. Reactive DMF reduces pH modified HAuCl4 at a faster rate via improved metal ligand exchange mechanism the inter-particle coupling provides unique strategy to promote complex sub-wavelength optical waveguides and nanophotonic devices.

Material and methods
Hydrochloroauric acid (Haucl4.3H2O) was purchased from sigma Aldrich chemicals and DMF (N,N-Dimethylmethanamide), NaOH (Sodium Hydroxide), and other washing chemicals were purchased from Loba chemie Pvt. ltd.

Experimental procedure
A solution 12μl of 0.169 M aqueous HAuCl3 was added to 500 μl (1000 μl) water followed by NaOH addition of different concentration as mention in graph. This mixture was added to DMF 4.5 ml (4 ml) DMF and put on sonication for 20 minutes under room temperature. As the reaction proceeded, the solution changed slowly in colour from light yellow to colorless to Apricot colour over few days.

However, the preparation method was partly modified in terms of heating process. A solution of 0.27 mM aqueous HAucl4 was added to 15ml of preheated mixture of DMF and water at 80oC and the mixture was refluxed by simply heating with vigorous stirring. As the reaction proceeded, the solution changed on color from light yellow to colorless to magenta color over few days.

Result and Discussion
We explore stable assembly of gold nanoparticles in single step process by introducing a simple chemical synthesis in which pH changed gold precursor is added to dimethylformamide solution at RT. The redox chemistry of N, N-dimethylformamide (DMF) has been effectively utilized in the formation of surfactant free, small chain metal NPs networks via molecular dipolar coupling. It has been observed that DMF has reducing ability in the basic medium for the metal ions, which is why it readily reduces AuCl3 even at room temperature, whereas it cannot reduce HAuCl3 (preferential solvation make the solution acidic in character). Hence the addition of a base like NaOH to a concentrated solution of Au+3 (HAuCl4) results in the neutralization of its acidity, leading to the rapid formation of hydroxyl containing gold complexes as a result of stepwise substitution of Cl-. The addition of OH- leads to the substitution of Cl- ligands, according to reaction,

$$AuCl_n (OH)^-_{4-n} + OH^- \rightleftharpoons AuCl_{n-1}(OH)^-_{5-n} + Cl^-$$
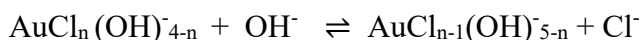
It was found that the reaction rate for formation of gold nanoparticles is affected by the pH of gold solution (with increase in pH NaOH reaction is faster). The chemical reduction of chloroauric acid to gold particles in the new reducing system therefore involves two step reaction process,

which are ligand substitution (Cl is replaced by OH) and chemical reduction of gold hydroxide species. As expected, the rate of ensuing nucleation process increases with increase in gold solution pH. The unusual UV- Vis spectra of as formed gold nanostructures at different pH modified metal precursor are illustrated in figure. 1.
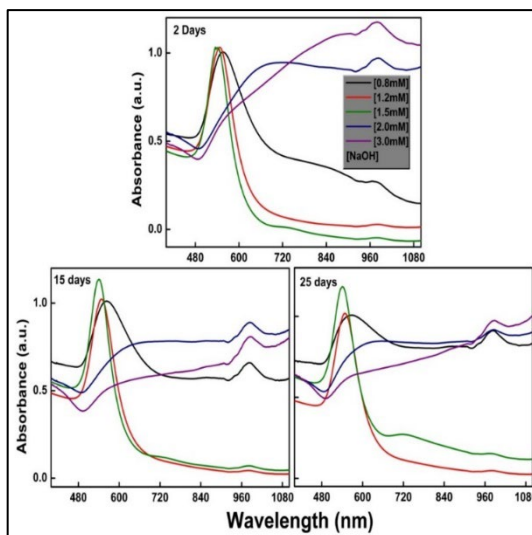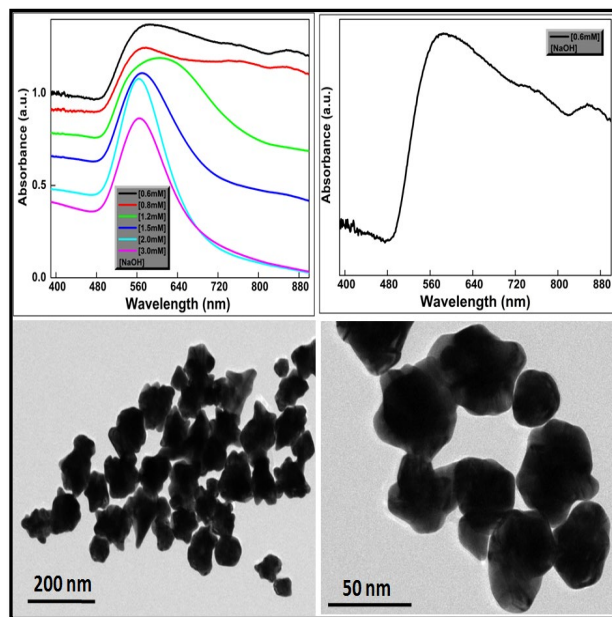

Figure 1. UV- Vis spectra of Gold nanoparticles obtained at different concentration of NaOH (resulting in pH modified Metal precursor) at DMF: water 9:1. Graph are normalize and translate vertically for better clarity.

Sub nano gap inter particle coupling b/w spherical Au NPs is seen (figure 2) through sequential LSPR shift from visible to NIR region arising due to dipole – dipole attraction further in confirmation with TEM images (figure 2). A new peak at 720 nm is observed (fig. 2) along with peak 540 nm (coincident with plasmon band of spherical particles) and intensity of this peak increase with time as shown in fig. 1 for NaOH at 1.5 mM sample.
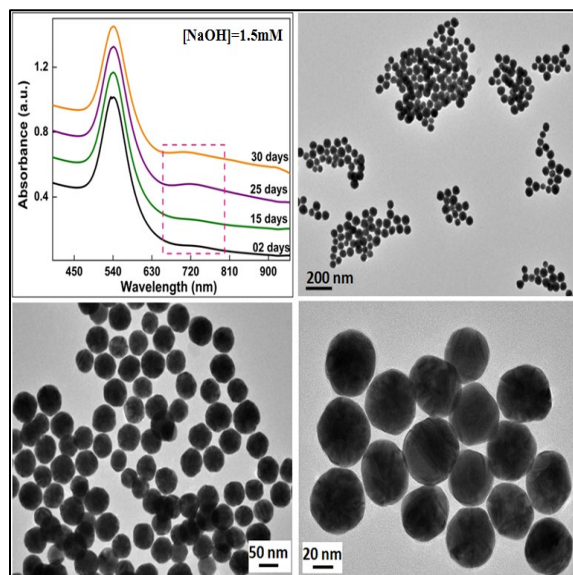
Figure 2. Kinetics absorption/TEM images illustrates assembled gold nanocrystal formation at DMF:water 9:1 and NaOH=1.5mM.

Arise of new peak is due to self-organization of 30nm spherical particles in 2-D array with subatomic between nearest particles can be seen clearly from the TEM image (fig. 2). And more organization is the intensity of longitudinal SPR and LSPR shifts towards red with increase in particle in array.

Furthermore, on increasing water content (take DMF: water ratio 4:1) we get assembly of anisotropic particles see fig. 3, instead of spherical as in low water see fig. 2. In this case anisotropic particle are formed and their assembly take place with time. Deviation from sphericity with decreased DMF to water ratio can result due to faster reducing ability of DMF in the presence of moisture.

Figure 3. *UV- Vis spectra and TEM images of Gold nanoparticles obtained at different concentration of NaOH (resulting in pH modified Metal precursor) at DMF:water 4:1. Graph are normalize and translate vertically for better clarity.*

Kinetic absorption/ TEM images in fig. 4 illustrate the formation of 1-D organized gold nanocrystals formation where pH modified metal precursor is added to refluxed (80oC) DMF: water mixture. TEM image clearly depicts the inter particle coupling and small nanochain networks.

Dipole-dipole attraction from anisotropic distribution of residual surface charge on gold nanoparticles as well as from DMF molecular dimers drives the careful formation of 1D pearl-necklace morphology.

Our main focus is on the molecular interactions responsible for the growth kinetics of as formed nanostructures. The complex formation between DMF and pH modified gold species ensuing in the formation of the N – Methyl formamide ligand substituted chloroaurate complexes which further result in the surfactant free Au nanoparticles chain networks through formation of carbamic/ dimcarb acid in the presence of sufficient water under ambient condition
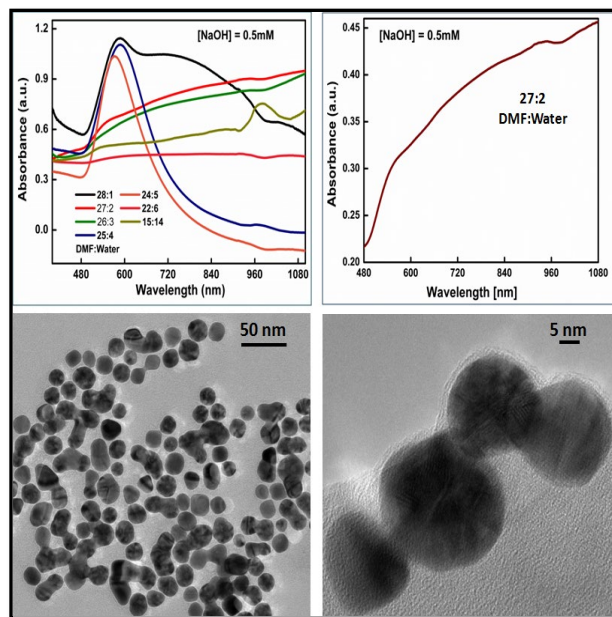
Figure 4. *one dimensional self-organization of gold nanostructures obtained at different DMF and water ratio by refluxing at 80ºC.*

Conclusion

DMF maneuvers aggregation of as prepared spheroidal gold nanocrystals through selected facets even under RT aging, giving rise to small linearly twisted plasmonic gold chain networks, Composition of different gold (III) complexes with increasing pH controls its redox potential, crucial for the essential formation of stable assembled nanogold dispersions. The inter particle coupling provides unique strategy to promote complex sub- wavelength optical waveguides and nanophotonic devices.

Acknowledgements

References

[1] Z. Y. Tang, N. A. Kotov, *Adv. Mater.* **2005**, *17*, 951. https://doi.org/10.1002/adma.200401593

[2] J. J. Penninkhof, A. Polman, L. A. Sweatlock, S. A. Maier, H. A. Atwater, A. M. Vredenberg, B. J. Kooi, Appl. Phys. Lett. 2003, 83, 4137. https://doi.org/10.1063/1.1627936

[3] L. Nagle, D. Ryan, S. Cobbe, D. Fitzmaurice, Nano Lett. 2003, 3, 51. https://doi.org/10.1021/nl025769j

[4] B. V. Enüstün, J. Turkevich, *J. Am. Chem. Soc.* **1963**, *85*, 3317. https://doi.org/10.1021/ja00904a001

[5] J. H. Liao, Y. Zhang, W. Yu, L. N. Xu, C. W. Ge, J. H. Liu, N. Gu, *Colloids Surf., A* **2003**, *223*, 177. https://doi.org/10.1016/S0927-7757(03)00156-0

[6] J. Y. Chang, J. J. Chang, B. Lo, S. H. Tzing, Y. C. Ling, *Chem. Phys. Lett.* **2003**, *379*, 261. https://doi.org/10.1016/j.cplett.2003.08.047

[7] A. N. Shipway, M. Lahav, R. Gabai, I. Willner, *Langmuir* **2000**, *16*,8789. https://doi.org/10.1021/la000316k

[8] B. Nikoobakht, M. A. El-Sayed, *Langmuir* **2001**, *17*, 6368. https://doi.org/10.1021/la010530o

[9] C. J. Johnson, E. Dujardin, S. A. Davis, C. J. Murphy, S. Mann, *J. Mater. Chem.* **2002**, *12*, 1765. https://doi.org/10.1039/b200953f

[10] A. M. Jackson, J. W. Myerson, F. Stellacci, *Nat. Mater.* **2004**, *3*, 330. https://doi.org/10.1038/nmat1116

[11] M. A. R. Meier,M. Filali, J.-F. Gohy, U. S. Schubert, J. Mater. Chem. 2006, 16, 3001. https://doi.org/10.1039/b602548j

[12] J. Sharma, S. Mahima, B. A. Kakade, R. Pasricha, A. B. Mandale, K. Vijayamohanan, J. Phys. Chem. B 2004, 108, 13280. https://doi.org/10.1021/jp0482013

[13] K. Osakada, A. Taniguchi, E. Kubota, S. Dev, K. Tanaka, K. Kubota, T. Yamamoto, Chem. Mater. 1992, 4, 562. https://doi.org/10.1021/cm00021a014

[14] F. Ahmad, V.S. Baswani, Polyhedron 1984,3,977. https://doi.org/10.1016/S0277-5387(00)84655-0

[15] I. Pastoriza- Santos, L. M. Liz-Marza'n, Langmuir 1999, 15, 949. https://doi.org/10.1021/la980984u

[16] J.Y. Yu, S. Schreiner, L. Vaska, Inorg. Chim. Acta 1990, 170, 145. https://doi.org/10.1016/S0020-1693(00)80465-X

[17] R. T. Tom, A.S. Nair, N. Singh. M. Aslam, C. I. Nagendra, R. Philip, K. Vijayamohanan, T. Pradeep, Langmuir 2003, 19, 3439. https://doi.org/10.1021/la0266435

[18] I. Pastoriza- Santos, L. M. Liz-Marza'n, Langmuir 2002, 18, 2888. https://doi.org/10.1021/la015578g

[19] A. Sa'nchez- Iglesias, I. Pastoriza- Santos, J. Pe'rez-juste, B. Rodri 'guez- Gonza 'lez, F. J. Garci'a de Abajo, L.M. Liz- Marza'n, Adv. Mater. 2006, 18, 2529. https://doi.org/10.1002/adma.200600475

[20] P.S. Kumar, I. Pastoriza- Santos, B. Rodri 'guez- Gonza 'lez, F. J. Garci'a de Abajo, L.M. Liz- Marza'n, Nanotechnology 2008, 19, 015606(1-5). https://doi.org/10.1088/0957-4484/19/01/015606

[21] A.V. Gaikwad, P. Verschuren, S. Kinge, G. Rothenberg, E. Eiserz, Phys. Chem. Chem Phys. 2008, 10, 951. https://doi.org/10.1039/B715112H

[22] M. A. R. meier, M. Filali, J. -F. Gohy, U.S. Schubert, J Mater. Chem. 2006, 16, 3001. https://doi.org/10.1039/b602548j

[23] M. Kanehara, E. Kodzuka, T. Teranishi, J. Am. Chem. Soc. 2006, 128, 13084. https://doi.org/10.1021/ja064510q

[24] H. Y. Lee, N.H. Lim, J.A. Seo, S.H. Yuk, B.K. Kwak, G. Khang, H.B. Lee, S. H. Cho, J. Biomed. Mater. Res. Part B 2006, 79, 142. https://doi.org/10.1002/jbm.b.30524

[25] I. Pastoriza- Santos, C. Serra- Rodr 'iguez, L.M. Liz- Marza'an, J. Colloid interface Sci. 2000, 221, 234. https://doi.org/10.1006/jcis.1999.6590

[26] I. Pastoriza- Santos, D. S. Koktysh, A. Mamedow, M. Giersig, N.A. Kotov L. M. Liz-Marza'n, Langmuir 2000, 16, 2731. https://doi.org/10.1021/la991212g

[27] D. S. Koktysh, X. Liang, B. _G. Yun, I. Pastoriza- Santos, R. L. Matts, M. Giersig, C. Serra-Rodr 'iguez , L. M. Liz-Marza'n, Langmuir, N.A. Kotov, Adv. Funct. Mater. 2002, 12, 255. https://doi.org/10.1002/1616-3028(20020418)12:4<255::AID-ADFM255>3.0.CO;2-1

[28] A. S. Nair, V. Suryanarayanan, T. Pradeep, J. Thomas, M. Anija, R. Philip, Mater. Sci. Eng. B 2005, 117, 173. https://doi.org/10.1016/j.mseb.2004.11.010

[29] J. Liu, W. Ong, A. E. Kaifer, Langmuir 2002, 18, 5981. https://doi.org/10.1021/la025956x

Keyword Index

About the Editors

	Dr. Yogesh Sonvane is working as Assistant Professor at Department of Physics at Department of Physics, SVNIT, Surat since 2012. He had 10 years of teaching experience and 14 years of research experience. His research area is Perovskite-based solar cells, Advanced Materials, 2D Materials, Nanomaterials, Nanofluids, Nanowires, Liquid Metal & its Alloy. He had published more than 80+ papers in SCI/Scopus Journals and 70+ papers in international conference proceedings. He had citations of 1500+, H- Index: 20; i10 Index: 33. Under his supervision Five students got Ph.D Degree and Six Students are pursing Ph.D.
	Dr. Dimple V Shah is an Associate Professor and HOD at Physics department, SVNIT Surat, Gujarat, India. She had teaching experience more than 15 years and had more than 20 years of research experience. His research area are Crystal Growth, Thin film, nano-materials, opto-electronic devices, semiconducting materials, thermo electric materials, magnetic materials, multiferroics and solar materials. She had published more than 50+ papers in SCI/Scopus Journals. He had citations of 700+, H- Index: 15; i10 Index: 24. Under her supervision, Five students got Ph.D Degree and Ten Students are pursuing Ph.D.
	Prof. Kamlesh Pathak is a Professor in the Department of Physics,at SVNIT, Surat. His varied research interests ranges from lower atmosphere to cosmology. He has more than 20 years of experience as a faculty as well as a researcher. He has quite a 50+ publications in SCI/Scopus Journals. He had citations of 700+, H- Index: 10; i10 Index: 15.Under her supervision, Five students got Ph.D Degree and Four Students are pursuing Ph.D.
	Dr. Lalit Kumar Saini is working as Assistant Professor at Department of Physics, SVNIT, Surat since 2007. He had 15 years of teaching experience and 19 years of research experience. His research area is Low Dimensional Quantum systems, Advanced Materials, 2D & 1D Materials, Nanomaterials, Coulomb drag. He had published more than 50+ papers in SCI/Scopus Journals and 30+ papers in international conference proceedings. He had citations of 500+, H- Index: 08; i10 Index: 10. Under his supervision, four students got Ph.D. Degree and three more Students are pursing Ph.D.